Tailoring the properties of metamaterials for linear and nonlinear applications

Dissertation
zur Erlangung des Grades
eines Doktors der Naturwissenschaften

von
Oleksiy Sydoruk
Kiew/Ukraine

genehmigt vom Fachbereich Physik der

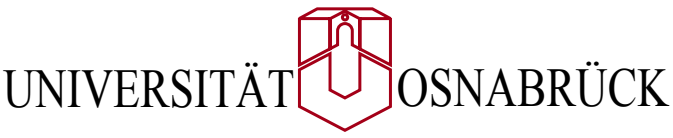

Osnabrück 2007

Tag der Einreichung: 9. Mai 2007

Tag der mündlichen Prüfung: 31. Mai 2007

Contents

1 Introduction **1**

2 Near-field properties of metamaterials **5**
2.1 A metamaterial element . . . 5
2.2 Interaction between metamaterial elements . . . 7
2.3 Waves on the arrays of elements . . . 8

3 Tailoring the dispersion properties **13**
3.1 Anisotropy of magnetic coupling . . . 13
3.2 Phonon-like dispersion . . . 17
3.2.1 Theory . . . 18
3.2.2 Experiment . . . 20
3.3 Coupled modes in diatomic metamaterials . . . 22
3.3.1 Theory . . . 23
3.3.2 Experiment . . . 29

4 Linear applications **35**
4.1 Shift-dependent transmission . . . 35
4.1.1 Experiment . . . 35
4.1.2 Theory . . . 37
4.1.3 Results . . . 38
4.1.4 Tailoring the transmission . . . 39
4.1.5 Concluding remarks . . . 42
4.2 Subwavelength imaging . . . 43
4.2.1 Tailoring the imaging capabilities . . . 43
4.2.2 Experiment . . . 44
4.2.3 Comparison between a single lens and a double lens . . . 48
4.2.4 Concluding remarks . . . 49
4.3 Subwavelength focusing . . . 51
4.3.1 General formulation . . . 51
4.3.2 Tailoring the subwavelength focus . . . 53
4.3.3 Concluding remarks . . . 57
4.4 Rotational Resonance . . . 58

4.4.1 Tailoring the power extraction 58
4.4.2 Concluding remarks 60

5 Nonlinear applications **61**
5.1 Basics of parametric amplification 62
5.2 Fulfilling phase-matching conditions 63
5.2.1 Monatomic arrays 63
5.2.2 Diatomic arrays 65
5.3 Theoretical formulation of parametric amplification 68
5.3.1 Monatomic arrays 68
5.3.2 Diatomic arrays 74
5.4 Amplification under rotational resonance 86
5.4.1 Rotational resonance and phase matching 86
5.4.2 Excitation of the traveling waves 87
5.4.3 Bistability of the parametric gain 89

6 Summary and outlook **91**

A Mutual inductance **95**

B Rotational resonance **99**

Bibliography **103**

The work on this thesis is accompanied by the following publications

1. O. Sydoruk, O. Zhuromskyy, E. Shamonina, and L. Solymar, Phonon-like dispersion curves of magnetoinductive waves, *Appl. Phys. Lett.* **87**, 072501-1-3 (2005).

2. O. Sydoruk, O. Zhuromskyy, and E. Shamonina, Dispersion characteristics of magneto-inductive waves made up by doubly periodic elements, *Proc. SPIE* **5955**, 595508-1-8 (2005).

3. O. Sydoruk, A. Radkovskaya, O. Zhuromskyy, E. Shamonina, M. Shamonin, C. J. Stevens, D. J. Edwards, G. Faulkner, and L. Solymar, Tailoring the near-field guiding properties of magnetic metamaterials with two resonant elements per unit cell, *Phys. Rev. B.* **73**, 224406-1-12 (2006).

4. L. Solymar, O. Zhuromskyy, O. Sydoruk, E. Shamonina, I. R. Young, and R. R. A. Syms, Rotational resonance of magnetoinductive waves: basic concept and application to Nuclear Magnetic Resonance, *J. Appl. Phys.* **99**, 123908-1-8 (2006).

5. R. R. A. Syms, O. Sydoruk, E. Shamonina, and L. Solymar, Higher order interactions in magneto-inductive waveguides, *Metamaterials* **1**, 44-51 (2007).

6. A. Radkovskaya, O. Sydoruk, M. Shamonin, C. J. Stevens, G. Faulkner, D. J. Edwards, E. Shamonina, and L. Solymar, Experimental study of a bi-periodic magnetoinductive waveguide: comparison with theory, *IET Microw. Antennas Propag.* **1**, 80-83 (2007).

7. A. Radkovskaya, O. Sydoruk, M. Shamonin, C. J. Stevens, G. Faulkner, D. J. Edwards, E. Shamonina, and L. Solymar, Transmission properties of two shifted magnetoinductive waveguides, *Microw. Opt. Technol. Lett.* **49**, 1054-1058 (2007).

8. O. Sydoruk, V. Kalinin, and E. Shamonina, Parametric amplification of magnetoinductive waves supported by metamaterial arrays, *phys. stat. sol. (b)* **244**, 1176-1180 (2007).

9. O. Sydoruk, M. Shamonin, A. Radkovskaya, O. Zhuromskyy, E. Shamonina, R. Trautner, C. J. Stevens, D. J. Edwards, G. Faulkner, and L. Solymar, Mechanism of subwavelength imaging with bilayered magnetic metamaterials: theory and experiment, *J. Appl. Phys.* **101**, 073903-1-8 (2007).

10. O. Sydoruk, E. Shamonina, and L. Solymar, Tailoring of the subwavelength focus, *Microw. Opt. Technol. Lett.* (in print).

and the following contributions to the conferences

1. O. Sydoruk, O. Zhuromskyy and E. Shamonina, Phonon-like dispersions of magneto-inductive waves in metamaterials, *Latsis Symposium on Negative Refraction*, Lausanne 28 February – 3 March 2005.

2. O. Sydoruk, O. Zhuromskyy and E. Shamonina, Dispersion characteristics of magneto-inductive waves made up by doubly periodic elements, *SPIE-COO Symposium*, Warsaw, Poland, 28 August–1 September 2005.

3. O. Sydoruk, O. Zhuromskyy, E. Shamonina and L. Solymar, Parametric amplification of magnetoinductive waves, 12^{th} *Int. Student Seminar on Microwave Applications of Novel Physical Phenomena*, St. Petersburg, Russia, 17–19 October 2005.

4. A. Radkovskaya, O. Sydoruk, E. Shamonina, C. J. Stevens, D. J. Edwards and L. Solymar, Waves on coupled lines of resonant metamaterial elements: Theory and experiments, *Progress in Electromagnetics Research Symposium PIERS 2006*, Cambridge MA, USA, 26–29 March 2006.

5. M. Shamonin, A. Radkovskaya, C. J. Stevens, G. Faulkner, D. J. Edwards, O. Sydoruk, O. Zhuromskyy, E. Shamonina, and L. Solymar, Waveguide and sensor systems comprising metamaterial elements, *DPG-Tagung*, Dresden, Germany, 26–31 March 2006.

6. O. Sydoruk, O. Zhuromskyy, E. Shamonina and L. Solymar, Parametric amplification of magnetoindcutve waves in bi-periodic metamaterial arrays, *DPG-Tagung*, Dresden, Germany, 26–31 March 2006.

7. A. Radkovskaya, N. Perov, A. Granovsky, M. Shamonin, O. Sydoruk, E. Shamonina, C. J. Stevens, D. J. Edwards, L. Solymar and O. Zhuromskyy, Magnetic metamaterials with tunable dispersion properties, *Annual Conference on New Materials*, Moscow, Russia, 13–16 June 2006.

8. O. Sydoruk, V. Kalinin, and E. Shamonina, Parametric amplification of magnetoinductive waves supported by metamaterial arrays, *DPG Summer School on Metamaterials*, Bad Honnef, Germany, 17–22 September 2006.

Chapter 1

Introduction

This work is devoted to metamaterials. What are they? Metamaterials are engineered electromagnetic composites demonstrating the properties not found in natural materials [1]. Usually they consist of resonant conductive elements arranged in a periodic manner. The properties of metamaterials are largely determined by the resonant properties of the individual elements and their interactions. The dimensions of the elements and the distances between them are typically much smaller than the operating wavelength of electromagnetic radiation. In this sense metamaterials are analogous to natural materials, where the sizes of the atoms and the distances between them are also much smaller than the wavelength.

It is known that interaction of atoms with an electric component of electromagnetic radiation gives birth to the electric permittivity of natural materials. Due to the resonant nature of the atoms, electric permittivity may exhibit strong dispersion around that resonance with its values changing in a wide range from positive to negative values. At the same time, most naturally occurring materials are insensitive to the magnetic component of electromagnetic radiation at optical frequencies, and their magnetic permeability is usually equal to unity. If there is, however, a need to alter the magnetic response of materials, artificial magnetism is a solution. Designing elements that exhibit magnetic resonance it is possible to create an artificial material – a metamaterial – with controllable magnetic properties.

What is the origin of the interest in metamaterials? In 2000, Pendry suggested that a slab of a metamaterial with a refractive index equal to -1 would act as a lens enabling total reconstruction of an object's spectrum, including its propagating and evanescent components [2]. One of the possibilities to achieve negative refraction is to realize a medium with simultaneously negative values of electric permittivity and magnetic permeability [3]. Smith et al. [4] suggested that a composite medium based on a combination of metallic rods and split rings would exhibit these properties. Shortly afterwards followed the experimental verification of negative refraction by Shelby et al. [5].

The history of metamaterials is full with exciting discoveries and rediscoveries. Negative refraction is the most famous example. At the time the work on this thesis has started, there seemed to be a general agreement about negative refraction, although the spirit of hot scientific discussions about its reality was still floating around. Further studies and historical surveys (see e.g. Ref. [6]) showed not only that negative refraction is feasible, but

also that it was known at least a century ago.

Less known rediscovery is the idea of nonlinear artificial media. It was suggested at the beginning of 1990s that a composite medium consisting of dipole antennas loaded by nonlinear elements should exhibit a much larger effective nonlinearity than is available with natural materials at microwaves [7]. It would allow to realize at microwaves a number of nonlinear effects known in optics. Phase conjugation was discussed as an example. Owing to a recent upsurge of the interest in metamaterials, this idea was revisited by Lapine et al. [8] and, shortly afterwards, by Zharov et al. [9]. Since then, nonlinear metamaterials have been at the focus of a number of studies (see eg. [10–15] and references therein).

Nowadays, the field of metamaterials has extended its borders to a range of problems much wider than negative refraction and imaging, although they still remain the mainstreams of contemporary research. Surprisingly enough, metamaterials are now seeking applications in a wide frequency range, from megahertz to visible and even beyond it.

At megahertz frequencies, metamaterials can be used for Magnetic Resonance Imaging. Being insensitive to constant magnetic fields, metamaterials have a potential for imaging [16–18] and detecting [19] signals coming from the human body.

At megahertz and gigahertz frequencies, miniaturized metamaterial structures can also be used for signal guiding and processing on a subwavelength scale. Waveguides, filters, couplers, delay lines, phase shifters etc., either directly based on metamaterial components or relying on similar principles, have already been suggested [20–26].

Terahertz frequencies have been so far the part of the electromagnetic spectrum less covered by devices; the reason is that many naturally occurring materials do not respond to radiation at these frequencies. Terahertz metamaterials aim at closing this gap [27–30].

With recent advances in the miniaturization of resonant elements [31–34], metamaterial research is pacing to optics – back to its origin. At the beginning of 2007, a magnetic metamaterial operating at the record value of 780 nm was reported [35].

In can be seen that most of the metamaterial research is application driven. It is natural, therefore, to search for possible applications, the main aim of this thesis. We shall concentrate on metamaterials operating at frequencies from 10 MHz to 1 GHz.

Our first goal is to understand how the properties of metamaterials should be modified and tailored in order to satisfy the specified requirements. The next goal is to apply the developed tailoring mechanisms to a number of effects, both linear and nonlinear, that are likely to be used in applications for Magnetic Resonance Imaging, signal guiding and processing.

We start in Chapter 2 by briefly summarizing the existing knowledge about the physical principles that govern the near-field behavior of metamaterials. The main concepts introduced in this Chapter are, first, magnetic coupling between a pair of metamaterial elements and, second, magnetoinductive waves propagating on the arrays consisting of a large number of elements.

In Chapter 3, we go deeper into the problem of magnetic coupling between the elements and develop a mechanism for tailoring the dispersion of magnetoinductive waves propagating on "diatomic" arrays comprising two metamaterial elements per unit cell.

In Chapters 4 and 5, we discuss a number of effects observed in one-dimensional magnetic

metamaterials. They are shift-dependent transmission, subwavelength imaging and focusing, rotational resonance, and parametric amplification. Finally, in Chapter 6 we summarize the results obtained and give an outlook for possible further research.

Chapter 2

Near-field properties of metamaterials

In this Chapter, we give a brief overview of the physical mechanisms governing the near-field properties of metamaterials and introduce necessary mathematical relationships. We shall analyze step-by-step the cases of single metamaterial elements, two coupled elements, and, finally, metamaterial arrays consisting of a large number of elements (see Fig. 2.1).

2.1 A metamaterial element

The forerunners of the contemporary magnetic metamaterial elements are the Split Ring Resonator (SRR) of Hardy and Whitehead [36] and the Loop-Gap Resonator of Froncisz and Hyde [37]. There is by now a large variety of such elements available: the Swiss Roll [38], the Capacitively Loaded Loop [23, 39, 40], the Spiral Resonator [41, 42], the Broadside-Coupled SRR [43], the Singly Split Double Ring [44] and the Twin Split Ring [45] to give a few examples. The common feature between them is that with good approximation they can be treated as resonant LCR circuits, as it is shown in Fig. 2.1 a. The parameters of the circuit are the inductance, L, the capacitance, C, and the resistance, R. The resonant element can then be characterized by two parameters: the resonant frequency,

$$\omega_0 = \frac{1}{\sqrt{LC}}\,, \tag{2.1}$$

and the quality factor,

$$Q = \frac{1}{R}\sqrt{\frac{L}{C}}\,. \tag{2.2}$$

The voltage, $V(t)$, induced by an external magnetic field, excites a current in the element that is governed by Kirchhoff's law

$$L\frac{\mathrm{d}I}{\mathrm{d}t} + \frac{1}{C}\int I\mathrm{d}t + RI = V(t)\,. \tag{2.3}$$

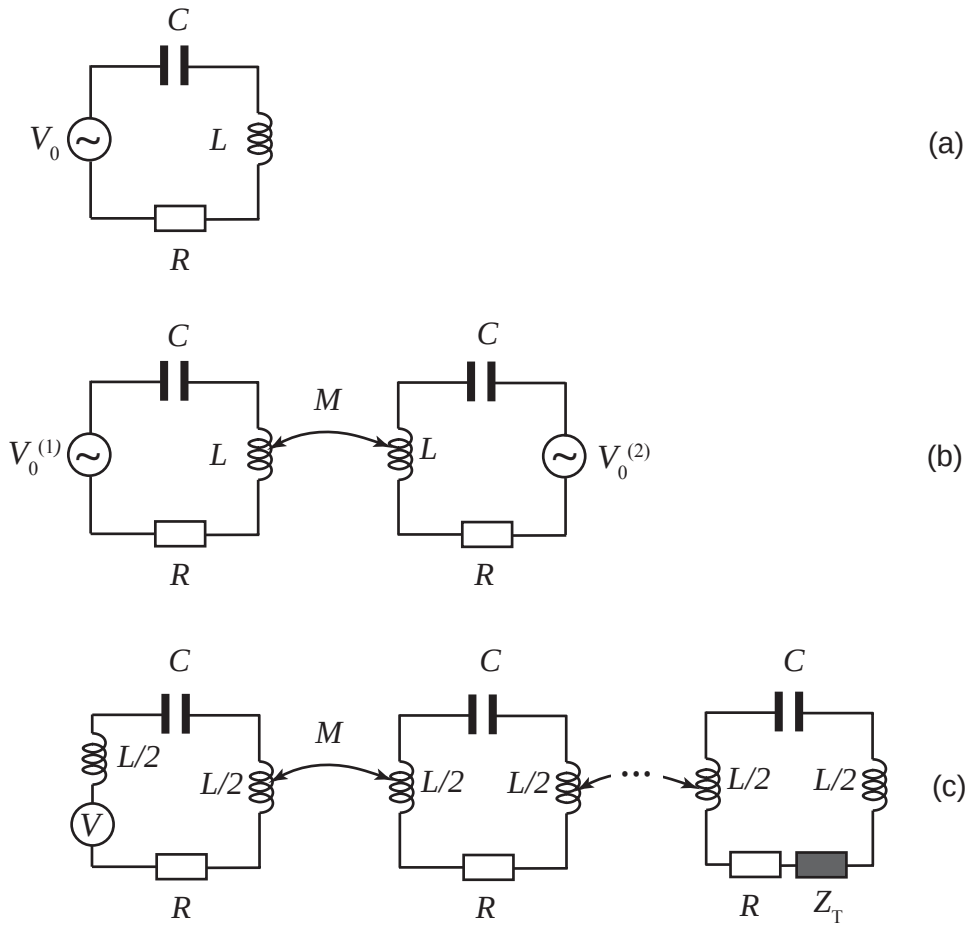

Figure 2.1: *An equivalent circuit of* (a) *an individual metamaterial element,* (b) *two magnetically coupled elements, and* (c) *a finite metamaterial array supporting magnetoinductive waves.*

In the case of a harmonically varying external field with a frequency ω, Kirchhoff's equation can be written in a simple algebraic form

$$\left(j\omega L + \frac{1}{j\omega C} + R\right) I_0 = V_0\,, \tag{2.4}$$

where I_0 and V_0 are the amplitudes of the current and of the voltage, respectively. If the element has a loop form then the relationship between the external magnetic field and the induced voltage in the element is

$$|V_0| = \mu_0 H_0 A\,, \tag{2.5}$$

where μ_0 is the free space permeability, H_0 is the amplitude of the applied magnetic field, and A is the area of the loop. The function

$$Z(\omega) = j\omega L + \frac{1}{j\omega C} + R \tag{2.6}$$

is the complex impedance of the element.

2.2 Interaction between metamaterial elements

The study of the properties of the individual elements was closely followed by further research on the interaction between them [23, 46–49]. The most obvious mechanism of interaction between the elements is magnetic coupling [50, 51]. Its origin can be understood from Figs. 2.2a and b showing two metamaterial elements close to each other. The current flowing in one of the elements generates a magnetic field. This field, going through the area of the neighboring element, affects the current flowing in it. As a result, the currents in both elements are coupled to each other via magnetic field. Since the distance between the neighboring elements in a metamaterial is typically much smaller than the wavelength of the corresponding electromagnetic radiation[1], this magnetic coupling is obviously of the near-field nature.

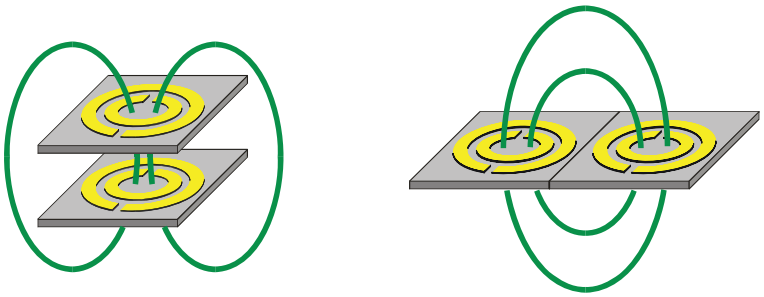

Figure 2.2: *Interaction between metamaterial elements; axial* (a) *and planar* (b) *configurations. The magnetic field generated by one of the elements affects the current in the other one giving birth to magnetic coupling.*

The equivalent circuit of two resonant elements with magnetic coupling between them is shown in Fig 2.1b. The new parameter is M, the mutual inductance between the elements. In the quasistatic, near-field, approximation it is defined as

$$M = \frac{\mu_0}{4\pi} \int_{\text{element 1}} \int_{\text{element 2}} \frac{\mathbf{dl}_1 \mathbf{dl}_2}{r_{12}}, \tag{2.7}$$

where $\mathbf{dl}_{1,2}$ are the current elements in the first and the second element, and r_{12} is the distance between them.

[1]This is true for low-frequency MHz metamaterials. If the size of the elements and/or the distance between them become comparable with the wavelength of the electromagnetic wave, retardation effects may become important and the coupling constant may have a more complicated, far-field, character [52, 53].

We can now rewrite Kirchhoff's equations for the currents in the first and the second elements in the form (we again assume here harmonic signals)

$$\begin{cases} ZI_1 + j\omega MI_2 = V_0^{(1)} \\ j\omega MI_1 + ZI_2 = V_0^{(2)} \end{cases} . \tag{2.8}$$

Here $V_0^{(1,2)}$ are the voltages in the first and the second elements, respectively.

The value and the sign of the mutual inductance between two elements depend on their relative orientation. Figure 2.2 shows two traditional cases, an axial and a planar one. In the axial configuration (Fig. 2.2 a), the magnetic fields of each of the elements in their centers have the same directions, and, hence, the mutual inductance is positive, $M > 0$. In the planar configuration (Fig. 2.2 b), the magnetic field generated by one element is in the opposite direction at the center of the other element and, correspondingly, the mutual inductance is negative, $M < 0$.

2.3 Waves on the arrays of elements

Let us now analyze the case when an infinite number of coupled elements is arranged into a one-dimensional periodic array. Two examples, an axial and a planar configuration, are shown in Fig. 2.3. It is well known that the solution of the eigenproblem for a system with an infinite number of degrees of freedom is given in the form of a traveling wave. In metamaterial arrays, these eigenmodes are waves of currents and they are called *magnetoinductive* (MI) waves [23,39]. The current in an arbitrary n^{th} element of the array is then of the form

$$I_n = I_0 e^{-jkan} , \tag{2.9}$$

where a is the period of the array and k is a wave number. In the presence of losses, k is complex and can be written in the form

$$k = \beta - j\alpha \tag{2.10}$$

with the propagation, β, and attenuation, α, constants.

Assuming that elements interact only with their nearest neighbors we can write Kirchhoff's equation for the n^{th} element of the array[2] in the form

$$\left(j\omega L + \frac{1}{j\omega C} + R \right) I_n + j\omega M(I_{n+1} + I_{n-1}) = 0 . \tag{2.11}$$

Substituting the wave ansatz (2.9) into Kirchhoff's equation (2.11) yields the dispersion relation of MI waves [23, 39]

$$1 - \frac{\omega_0^2}{\omega^2} - \frac{j}{Q} + \kappa \cos ka = 0 , \tag{2.12}$$

[2]Generalizations for two- and three-dimensional cases as well as for the case when higher-order couplings are significant can be found in Refs. [39, 54].

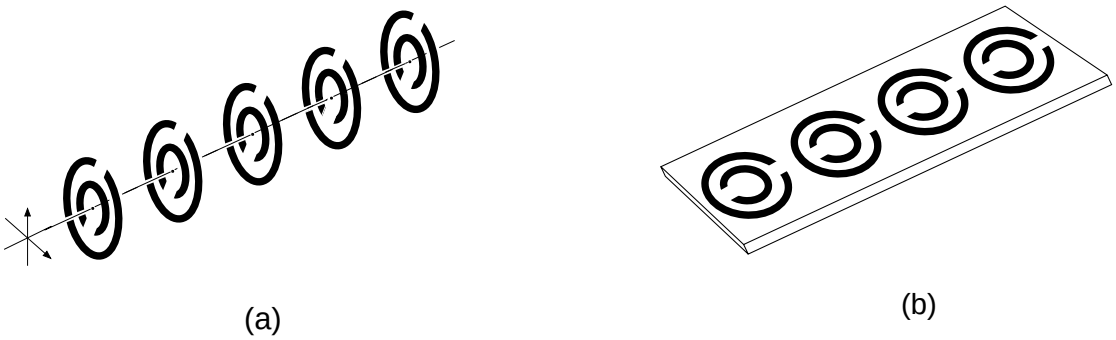

Figure 2.3: *Two traditional, an axial* (a) *and a planar* (b)*, configurations of metamaterial arrays.*

where

$$\kappa = \frac{2M}{L} \tag{2.13}$$

is the coupling constant.

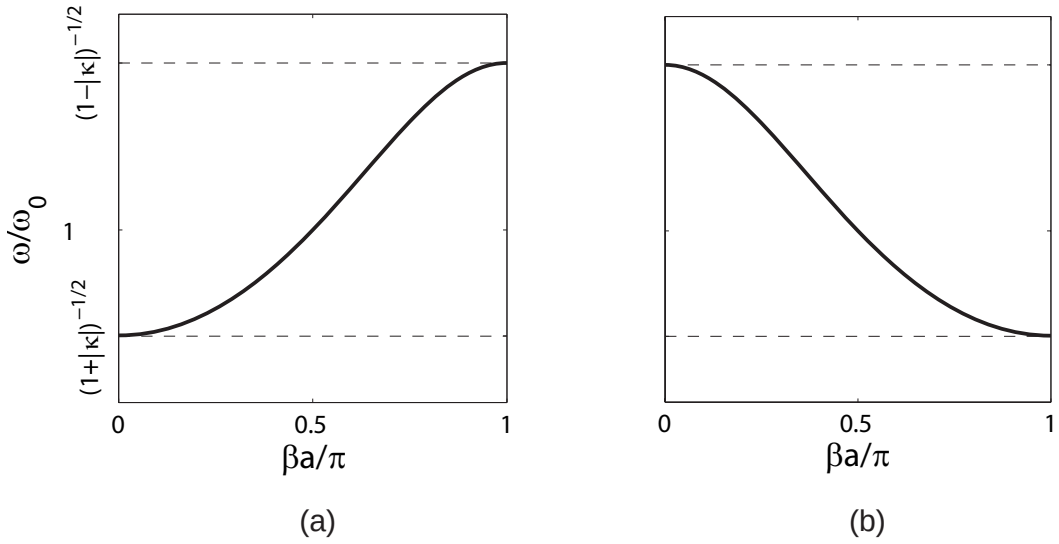

Figure 2.4: *Dispersion curves for an axial* (a) *and planar* (b) *configurations of metamaterial elements. MI waves are forward in the axial and backward in the planar array.*

Two typical dispersion curves, one for an axial array, Fig. 2.3 a, and the other for a planar array, Fig. 2.3 b, are shown in Fig. 2.4 for the lossless case. The dispersive nature of MI waves can be clearly seen. First, they can propagate only in a pass band around the resonant frequency of the elements, where the frequency ω takes the values

$$\frac{1}{\sqrt{1+|\kappa|}} < \frac{\omega}{\omega_0} < \frac{1}{\sqrt{1-|\kappa|}} \ . \tag{2.14}$$

Second, the type of the propagated wave depends on the sign of the coupling constant. MI waves are forward in the axial array, Fig. 2.3 a, with positive coupling between the elements. They are backward in planar arrays, Fig. 2.3 b, with negative coupling.

We have been talking so far about infinitely long arrays. In practice, they are, of course, finite. In order to propagate traveling waves in the form (2.9) a finite array should be loaded by proper matching impedances, which absorb power at its end. If only the nearest neighbors are taken into account the value of the matching impedance in the last element of the array is given by [39]

$$Z_{\mathrm{T}} = j\omega M e^{-jka} \,. \tag{2.15}$$

It has, in the general case, both non-zero real and imaginary parts whose values depend on frequency. A theory for the case where higher-order interactions are significant is also available [55].

An equivalent circuit of an array consisting of N elements is shown in Fig. 2.1 c. The first element is excited, and the last element is loaded by the matching impedance. For each element of the array, we can then write Kirchhoff's equation in the form analogous to Eqs. (2.4) and (2.8). As a result, we obtain a system of N algebraic equations that can be written in a compact matrix form

$$\mathbf{ZI} = \mathbf{V} \,. \tag{2.16}$$

Here $\mathbf{V}$ and $\mathbf{I}$ are the column-vectors of, respectively, the voltages and the currents in the elements, and $\mathbf{Z}$ is the impedance matrix

$$\mathbf{Z} = \begin{pmatrix} Z(\omega) & j\omega M & 0 & \dots & \dots & \dots & 0 \\ j\omega M & Z(\omega) & j\omega M & 0 & \dots & \dots & \vdots \\ 0 & j\omega M & Z(\omega) & j\omega M & 0 & \dots & \vdots \\ \vdots & \ddots & \ddots & \ddots & \ddots & \ddots & \vdots \\ \vdots & \dots & \ddots & \ddots & \ddots & \ddots & 0 \\ \vdots & \dots & \dots & \ddots & \ddots & \ddots & j\omega M \\ 0 & \dots & \dots & \dots & 0 & j\omega M & Z(\omega) + Z_{\mathrm{T}} \end{pmatrix} , \tag{2.17}$$

where the self-impedance of a single element, $Z(\omega)$, is given by Eq. (2.6). Knowing the applied voltages, $\mathbf{V}$, and the impedances, $\mathbf{Z}$, it is then possible to calculate currents in each element of a finite array.

MI waves are slow waves: their phase velocity is much smaller than the velocity of light. Based on this property, a number of potential applications that allow manipulating magnetic field on a subwavelength scale was suggested. The first and the most obvious application for any type of waves is waveguiding. Discrete magnetoinductive waveguides were investigated both theoretically [23] and experimentally [40, 56]. Further studies were concerned with the design of couplers, power dividers [57], delay lines [48], filters [49], and quasioptical components such as Fabry-Perot resonators, mirrors, and Bragg gratings [26]. MI waves can couple to electromagnetic waves [58] and they can exhibit positive and negative refraction at the boundary of two metamaterial media [59].

MI waves have their analogs both in microwave and optical frequency regions. Dispersion equations for waves propagating along arrays of magnetically coupled resonators were derived in Refs. [60] and [61] with applications to electric filters and to slow wave structures in mind. An antenna array excited by a single element was shown to be able to support a leaky wave [62], which is partially guided and partially radiating. A physical realization of such an array of resonant elements became available in the late 1990s due to the technological advances in producing features on the nanometer scale. Tiny spheres of resonant metallic elements were produced and shown to be able to support waves [63]. Wave propagation both by transverse and longitudinal electric dipoles was demonstrated at optical wavelengths [64, 65]. A similar theoretical analysis for waves along an array of loaded, electrically coupled metallic rods was carried out in Ref. [66]. In photonic crystals, the possibility of guiding a wave within an impurity band by chains of coupled resonators was demonstrated [67]. An optical waveguide based on similar principles was proposed in Ref. [68].

Chapter 3

Tailoring the dispersion properties

We have summarized in the previous Chapter the conventional wisdom about the near-field properties of metamaterials. In particular, we have shown that magnetic coupling between the resonant elements in an array leads to the propagation of MI waves. In this Chapter, we step onto the unexplored territory of tailoring the properties of metamaterials.

What do we understand here under the term *tailoring*? We could see in the previous Chapter that the performance of MI wave devices depends largely on the available dispersion characteristics. That is why tailoring means for us first of all designing such dispersion characteristics that would satisfy specific, predetermined, requirements.

These requirements may, of course, vary from application to application. Therefore, we should aim at a tailoring mechanism that is flexible enough to satisfy diverse demands of different applications. Fortunately, metamaterial engineering supplies a researcher with an effective tool to meet this challenge: a possibility to freely control microscopic parameters of metamaterials and in such a way to influence their macroscopic properties.

In particular, the dispersion characteristics of MI waves (a macroscopic property) depends on two microscopic constituents: first, individual elements (resonance frequency, ω_0, and quality factor, Q) and, second, near-field magnetic coupling between the elements.

The properties of individual elements are determined by their actual design. In the case of capacitively-loaded loops [23, 40], for example, the resonant frequency can be easily changed by changing the value of the externally soldered capacitor. This method is employed in the experiments described later in this Chapter.

The value of magnetic coupling between two elements is determined by their shape, mutual orientation, and relative position. It is natural, therefore, to start the discussion about tailoring the dispersion properties by studying in more detail the interaction between individual elements.

3.1 Anisotropy of magnetic coupling

We assume in our theoretical calculations that the elements have a circular form and can be presented by infinitely thin metallic loops. The mutual inductance between two arbitrary

oriented loops can be calculated as shown in Appendix A. Here we shall distinguish between two different orientations: with normals to the elements being parallel (Fig. 3.1 a) and perpendicular (Fig. 3.1 b) to each other. In both cases, the relative position of the second element can be described by two variables: the "lateral" shift in the plane of the first element, Δ, and the "vertical" shift in the direction of the normal of the first element, h.

Fig. 3.1 a shows the variation of the coupling constant with the relative position of two elements of radius r_0 with normals parallel to each other (both normals directed upwards) and Fig. 3.1 b, with normals perpendicular to each other (with the normal of the first element directed upwards and the normal of the second element directed to the right). Figure 3.1 a contains a number of known limiting cases. If $\Delta = 0$ then the elements are in the axial configuration, and the coupling is positive. If $h = 0$ then the elements are in the planar configuration with negative coupling. The coupling constant is identical for all four quadrants of the plane (Δ, h), so it is sufficient to discuss the properties of the first quadrant ($\Delta \geq 0$, $h \geq 0$). There is a curve of zero coupling in the plane (Δ, h). For any set of (Δ, h) above this curve the coupling is positive, and for any set of (Δ, h) below the curve it is negative. The situation is quite different (Fig. 3.1 b) when the normals of the elements are perpendicular to each other. The limiting cases here are as follows: there is no coupling if either of the shifts is zero, $\Delta = 0$ or $h = 0$, which follows from a symmetry argument. The coupling is positive for the first and third quadrants and negative for the second and fourth quadrants.

How accurately does this theory, based on the assumption of circular loops and filament currents, describe the properties of actual metamaterial elements? In order to answer this question we compare below the theoretical predictions with experimental data obtained for two different types of elements.

The elements of the first type[1] are capacitively-loaded split pipes. A photograph may be seen in Fig. 3.2 b and a schematic drawing in Fig. 3.2 a showing the dimensions: inner diameter, $2r_0 = 20$ mm, wall thickness, $w = 1$ mm, wall height, $l = 5$ mm, gap width, $g = 2$ mm. They are loaded by nominally identical capacitors of 330 pF. Their resonant frequencies and quality factors measured with the aid of a network analyzer of the type HP8753C were found as $f_0 = \omega_0/(2\pi) = (46.2 \pm 0.2)$ MHz and $Q = 105 \pm 5$.

The value of magnetic coupling between two elements can be determined by measuring the currents flowing into them. As follows from Eq. (2.8), the coupling leads to the split of the individual resonances of the elements into two. Measuring the frequencies of the two resonances,

$$\omega_{1,2} = \frac{\omega_0}{\sqrt{1 \pm \dfrac{M}{L}}},$$

it is possible to determine the ratio M/L and, hence, the coupling constant, κ. In the experiments, the elements were first placed in an axial configuration with a vertical shift $h = 10$ mm. Then one of the elements was shifted relative to the other in the lateral

[1]The experiments were carried out at Oxford University by Dr. A. Radkovskaya (Moscow University), Mr. G. Faulkner, Dr. C. J. Stevens and Prof. D. J. Edwards (Oxford University).

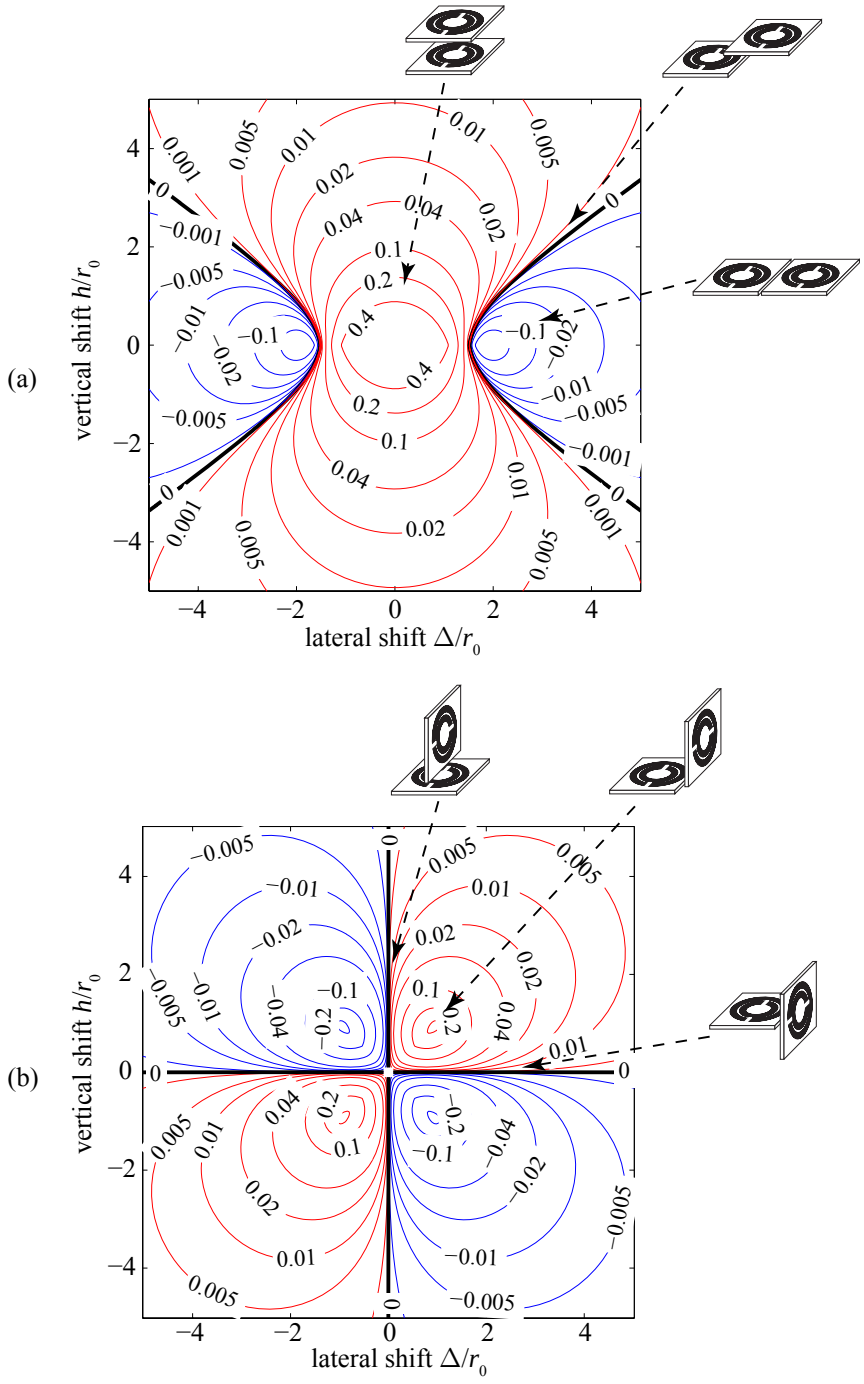

Figure 3.1: *Anisotropy of magnetic coupling between two elements. The contour plot for the coupling constant versus lateral and vertical shift,* (a) *with elements lying in parallel planes and* (b) *with elements lying in perpendicular planes.*

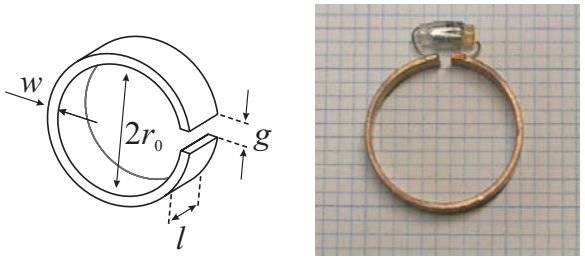

(a) (b)

Figure 3.2: *Schematic presentation of the capacitively-loaded split pipe* (a), *its photograph* (b).

direction at a distance $\Delta = 35$ mm, as shown in the inset to Fig. 3.4, and the coupling constant was determined in a number of points. The experimental values obtained are shown in Fig. 3.4 by filled circles. The corresponding theoretical values are shown by a solid line. The agreement between the theory and experiment is very good. The coupling constant is positive for $\Delta < 20$ mm, zero around $\Delta = 20$ mm, and negative for $\Delta > 20$ mm.

The elements of the second type[2] are planar three-turn inductors formed on printed-circuit board (type FR 4), as shown in Fig. 3.3, and made resonant using additional surface mount capacitors. The inductance and capacitance are $L = 140$ nH and $C = 100$ pF respectively, giving a resonant frequency of $\omega_0/(2\pi) = 42$ MHz. At this frequency, the quality factor (found from measurements of bandpass characteristics using an Agilent E5061A Network Analyser) is 50.

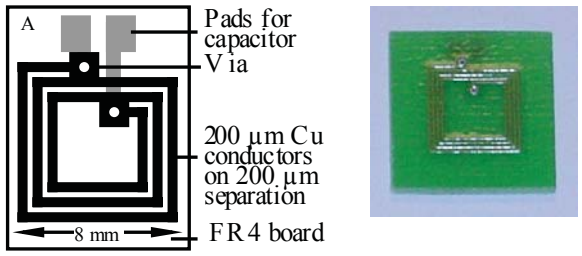

(a) (b)

Figure 3.3: *Schematic presentation of the planar capacitively-loaded inductor element* (a), *its photograph* (b).

Two elements were placed in an axial configuration at a distance $h = 0.2$ mm. Then one of them was shifted against the other at a distance $h = 13.5$ mm, as it is shown in the inset to Fig. 3.5. The coupling constant was again determined in a number of points. The experimentally determined values are shown in Fig. 3.5 by filled circles and the corresponding theory, by a solid line. We can see that, similarly to the previous case, the agreement between the theory and experiment is very good confirming the reliability of the theoretical model.

[2]The experiments were carried out by Prof. R. R. A. Syms at Imperial College, London.

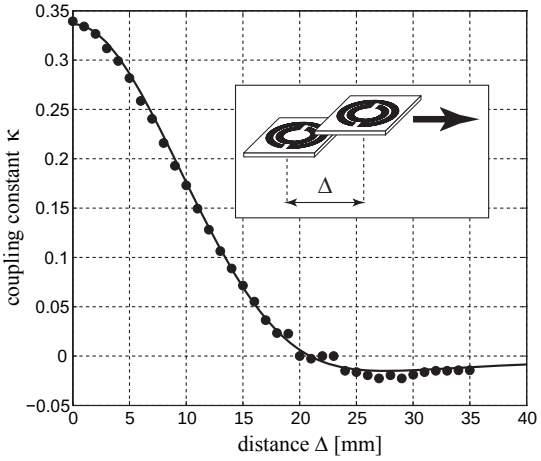

Figure 3.4: *Experimental (filled circles) and theoretical (solid line) values of the coupling constant between two capacitively-loaded split pipes.*

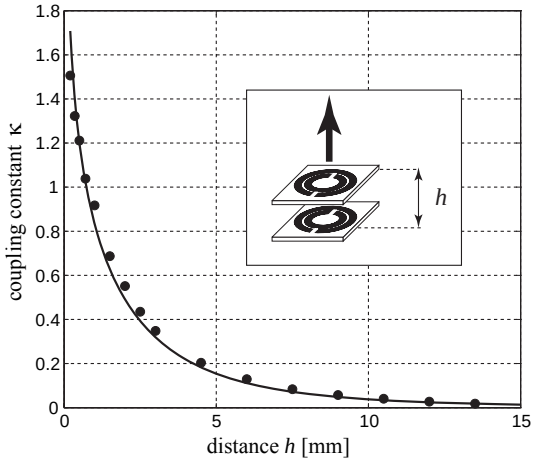

Figure 3.5: *Experimental (filled circles) and theoretical (solid line) values of the coupling constant between two capacitively-loaded inductor elements.*

We can conclude that magnetic coupling between two elements is highly anisotropic; positive, negative and zero values of the coupling constant can be realized by placing elements in different positions relative to each other. In the following, we shall employ the anisotropy of magnetic coupling in constructing a variety of structures supporting MI waves with distinct dispersion relations.

3.2 Phonon-like dispersion

We can now make use of the ability to vary the resonant properties of the elements and the coupling between them for tailoring the dispersion properties of MI waves. The way forward is suggested by the close analogy between MI waves and acoustic waves in solids. It is well known that the dispersion characteristics of diatomic solids differ greatly from those having identical atoms (see e. g. [69]). It is not only that the width of the pass band and the initial slope of the curve are different, but also a new, "optical", branch appears. The new branch is a direct consequence of bi-periodicity known in Solid State Physics (see e. g. [70, 71]). It may, therefore, be expected that metamaterial arrays made up by elements in a "diatomic" arrangement will follow similar trend and will give us some additional flexibility in design.

The transition from a "monatomic" to a "diatomic" metamaterial array is demonstrated in Fig. 3.6. There are two obvious ways to realize a diatomic metamaterial: to change periodically some parameter of the elements (resulting in a change of the resonant frequency)

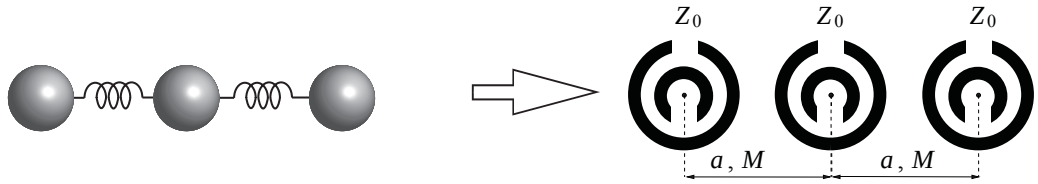

(a)

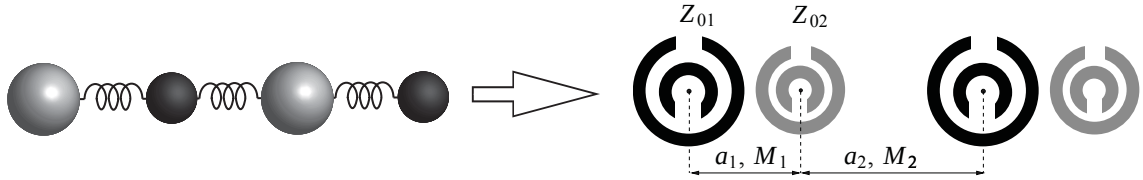

(b)

Figure 3.6: *Analogy between acoustic waves in solids and MI waves in metamaterials. Both phonons in a monatomic solid and MI waves in a "monatomic" metamaterial array have a single branch of the dispersion characteristics* (a). *Two branches appear in a diatomic solid and in a "diatomic" metamaterial array* (b).

and to vary the distance between them (resulting in a change of the mutual inductance). Both possibilities are shown. Whereas the monatomic metamaterial array of Fig. 3.6 a consists of a single type of elements with a distance a between them, the diatomic metamaterial array of Fig. 3.6 b consists of two different types of elements with two different periods a_1 and a_2.

3.2.1 Theory

The derivation of the dispersion relation for MI waves propagating along a diatomic metamaterial array relies on Kirchhoff's equations for the currents in two neighboring elements and is analogous to the derivation of the dispersion for phonons [69, 71]. Let us denote the currents in the neighboring elements of the array by I_{01} and I_{02}. Assuming no applied voltage and traveling wave propagation, Kirchhoff's equations can be written as

$$\begin{cases} Z_{01}I_{01} + j\omega I_{02}\left[M_1 \exp\left(-jka_1\right) + M_2 \exp\left(jka_2\right)\right] = 0 \\ Z_{02}I_{02} + j\omega I_{01}\left[M_1 \exp\left(jka_1\right) + M_2 \exp\left(-jka_2\right)\right] = 0 \end{cases}, \tag{3.1}$$

where $Z_{01,02}$ are the impedances of the elements. Equation (3.1) has nontrivial solutions only if the determinant of coefficients for I_{01} and I_{02} vanishes

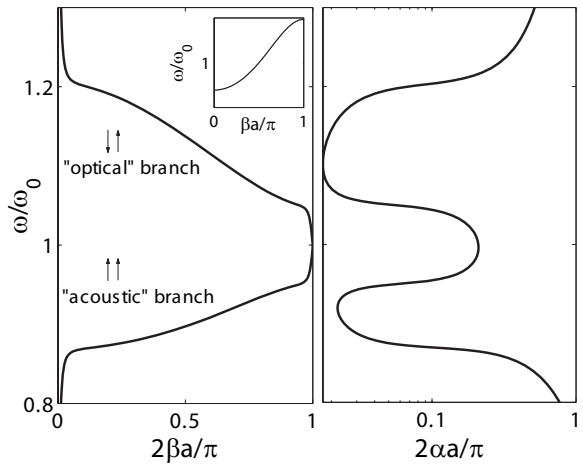

Figure 3.7: *Dispersion curve for the diatomic axial configuration. Currents within a unit cell are in anti-phase in the upper ("optical") and in phase in the lower ("acoustic") branch. Inset shows the dispersion curve for the monatomic case.*

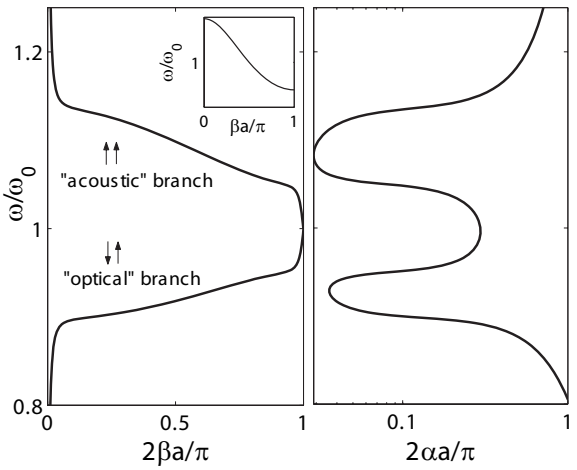

Figure 3.8: *Dispersion curve for the diatomic planar configuration. Currents within a unit cell are in phase in the upper ("acoustic") branch and in anti-phase in the lower ("optical") branch. Inset shows the dispersion curve for the monatomic case.*

$$\begin{vmatrix} Z_{01} & j\omega\left[M_1\exp\left(-jka_1\right)+M_2\exp\left(jka_2\right)\right] \\ j\omega\left[M_1\exp\left(jka_1\right)+M_2\exp\left(-jka_2\right)\right] & Z_{02} \end{vmatrix} = 0\,. \quad (3.2)$$

Solution of Eq. (3.2) yields the dispersion equation. It can be written in the form

$$\cos k\frac{a_1+a_2}{2} = \pm\frac{1}{2\sqrt{M_1M_2}}\sqrt{-\frac{Z_{01}Z_{02}}{\omega^2}-\left(M_1-M_2\right)^2}\,. \quad (3.3)$$

The frequency information is contained in the impedances

$$Z_{01,02} = j\omega L_{1,2}+\frac{1}{j\omega C_{1,2}}+R_{1,2}\,. \quad (3.4)$$

Let us now look at two practical examples, one for the axial and one for the planar array of capacitively-loaded loops [23, 40]. In both cases we shall assume that the distances and the inductances are the same and only the capacitances vary from element to element. The parameters chosen are as follows: loop radius, $r_0 = 10$ mm, wire thickness, $r_w = 2$ mm. The circuit parameters are $L = 33$ nH, $C_1 = 208$ pF, $C_2 = 177$ pF. Then $\omega_{01} = 0.95\omega_0$

and $\omega_{02} = 1.05\omega_0$ with $\omega_0/(2\pi) = 63.87$ MHz, which is the frequency at which the nuclear magnetic moment of a proton precesses in a magnetic field of 1.5 T in MRI applications. For the axial configuration, we choose $a = 10$ mm resulting in $M_1/L = M_2/L = 0.149$ and for the planar case, $a = 20.5$ mm corresponding to $M_1/L = M_2/L = -0.104$. The losses will be characterized by a quality factor of 150.

The dispersion curves with both propagation and attenuation constants are shown in Figs. 3.7 and 3.8. Note that there is a stop band in the middle in both cases for the range $\omega_{01} < \omega < \omega_{02}$. The physical reason is that within this band the loops' impedances have different characters, one is inductive and the other one is capacitive.

We can immediately see from Figs. 3.7 and 3.8 that the major distinction between the axial and planar configurations is no longer there. We have forward propagating waves in the lower and backward propagating waves in the upper branch independently of the configuration. There is, however, a difference if we consider the phases of the currents within a unit cell. For the axial line, the currents of the neighboring elements in the upper branch are in anti-phase and the currents in the lower branch are in phase. Using the analogy with the diatomic model we can refer to the upper branch of the dispersion characteristics as "optical" and to the lower branch as "acoustic" (Fig. 3.7). For the planar line, the situation is reversed: the currents of the lower branch are now in anti-phase, thus this is the one that we should call "optical" branch (Fig. 3.8). It is worth noting that, in contrast to the dispersion of phonons, both branches of the MI wave dispersion curve may be responsible for interaction with electromagnetic waves [58].

3.2.2 Experiment

One of the interesting conclusions drawn above is that for the diatomic case the lower one of the two branches is always a forward wave and the upper one is always a backward wave independently of the orientation of the elements, whether they are planar or axial. A series of experiments was performed[3] in order to compare this and other theoretical predictions with the measured results.

The elements are identical split pipes loaded with two different sets of capacitors so that alternating elements in the one-dimensional array are tuned to different resonant frequencies as shown in Figs. 3.9 a and b for the planar and axial configurations respectively. For the elements' dimensions, see Fig. 3.2 and the text therewith. C_{A} and C_{B}, the capacitances inserted into elements A and B, were 330 pF and 680 pF respectively, resulting in resonant frequencies of $\omega_{0\mathrm{A}}/(2\pi) = 46.21$ MHz and $\omega_{0\mathrm{B}}/(2\pi) = 32.46$ MHz. Careful selection of the capacitors ensured that the resonant frequencies varied by no more than 0.3%. The quality factor extracted from the measured resonance curve was found to be between 100 and 110 for both kinds of elements.

In experiments, diatomic lines consisting of altogether 16 elements, in which elements A and B alternate, were studied. The spacing between the elements was $a = 20$ mm for

[3]The experiments were carried out at Oxford University by Dr. A. Radkovskaya (Moscow University), Mr. G. Faulkner, Dr. C. J. Stevens and Prof. D. J. Edwards (Oxford University).

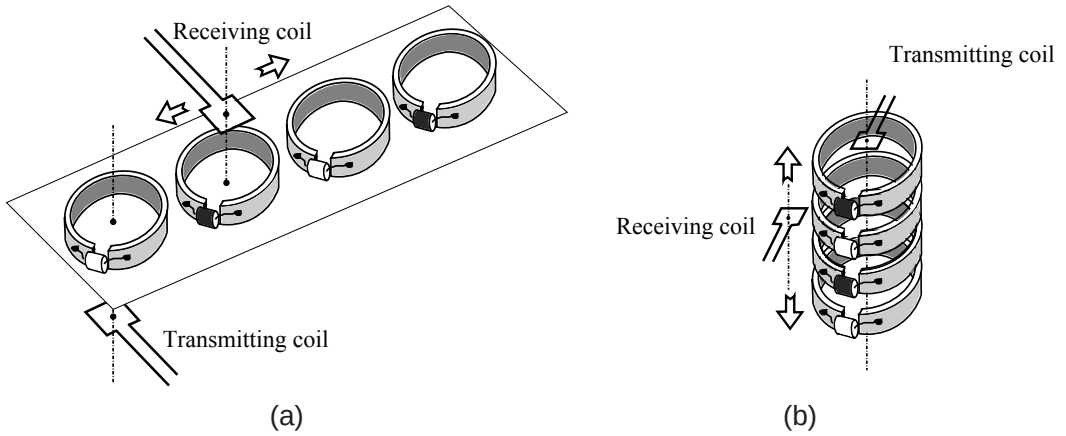

Figure 3.9: *Schematic presentation of* (a) *planar and* (b) *axial configurations with measuring coils.*

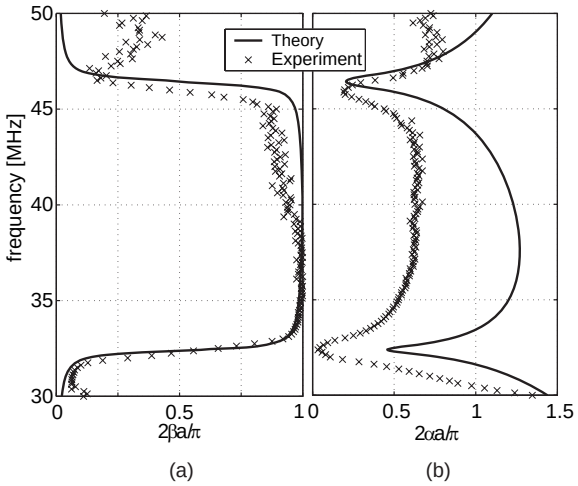

Figure 3.10: *Dispersion characteristics for a diatomic axial array,* (a) *propagation and* (b) *attenuation constants.*

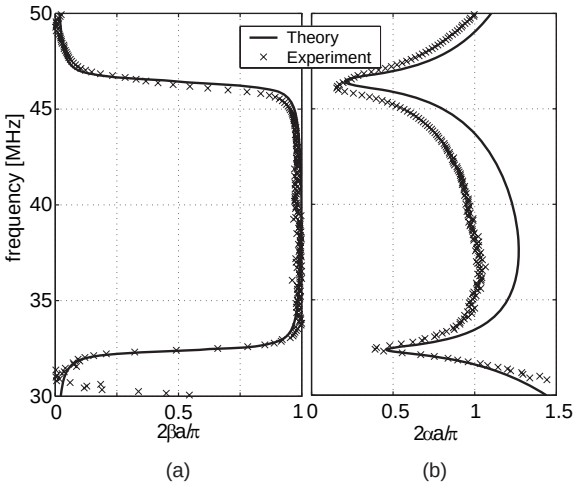

Figure 3.11: *Dispersion characteristics for a diatomic planar array,* (a) *propagation and* (b) *attenuation constants.*

the axial and $a = 24$ mm for the planar configuration. The coupling constants were found to be $\kappa = 0.1$ and $\kappa = -0.1$ for the axial and planar cases respectively. The first element was excited. The phase and amplitude at each element were measured for 1601 frequency points in the range $25 - 55$ MHz for the planar and $25 - 65$ MHz for the axial arrangement. The dispersion curves are extracted from the phase and amplitude measurements at the first five elements. The experimentally obtained values, phase change and attenuation, are shown by crosses in Figs. 3.10 a and b for the axial and in Figs. 3.11 a and b for the planar configuration.

Substituting the parameters of the experiment into the dispersion relation (3.3) we obtain the phase change and attenuation for both configurations. They are shown by continuous lines in Fig. 3.10 for the axial and in Fig. 3.11 for the planar case. It is gratifying to note that the principal prediction of the theory, that the diatomic dispersion curves look the same for the planar and axial configurations, is indeed borne out by the experimental results. The detailed agreement is excellent for the phase changes. For the attenuation, there is only qualitative agreement: it can be seen that the theoretically predicted attenuation is larger than the measured one. The likely reason is higher order interactions that increase the amplitude measured.

3.3 Coupled modes in diatomic metamaterials

In a diatomic array, MI waves have two branches of the dispersion characteristics, a forward and a backward one. We have control over the positions and the width of the branches via the resonant frequencies of the elements and the coupling between them. Additional freedom of tailoring the dispersion of a diatomic metamaterial in comparison to the monatomic case is, obviously, a result of having more parameters that could be varied.

Is there room for further improvement? Yes, there is. The diatomic configurations considered in the previous Section are limited to the traditional axial and planar arrangements (see Figs. 2.3 and 3.9). On the other hand, as we have seen in Section 3.1, additional flexibility could be gained also with alternative arrangements. We could then generalize a diatomic metamaterial in the way it is shown schematically in Fig. 3.12. The similarity to the previous case is a unit cell consisting of two different elements. In this case, however, each element has not two but five neighbors to which it couples via the mutual inductances M_1, M_2, M, M_3 and M_4.

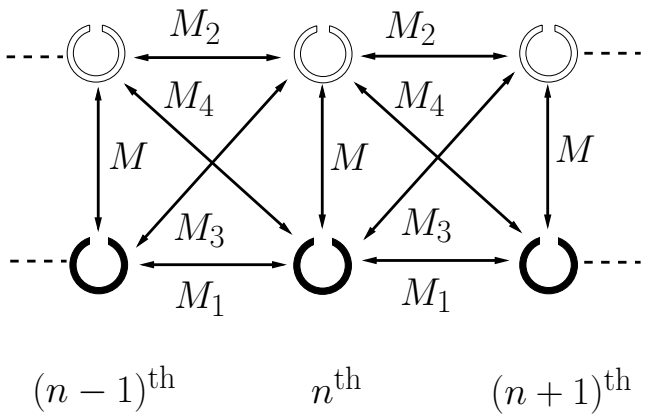

Figure 3.12: *Schematic presentation of the coupling between two lines of resonant magnetic metamaterial elements. Mutual inductances M_1, M_2, M, M_3 and M_4 between the nearest neighbors are shown by arrows.*

First, we shall theoretically analyze the interaction mechanisms in a diatomic metamaterial array with magnetic coupling between nearest neighbors and then check the theoretical predictions experimentally.

3.3.1 Theory

General formulation

The derivation presented here can easily be generalized to the case of couplings between any pair of elements. However, the mutual inductances between the elements decline fast and it may be justified (at least in the pass bands) to take only nearest neighbor interactions into account. We shall return to the problem of higher-order interactions in Section 3.3.2.

We start with an equidistant linear array of identical resonant elements. Kirchhoff's voltage equation for the n^{th} element is of the form (see Section 2.3)

$$Z_{01} I_n + Z_1 \left(I_{n-1} + I_{n+1} \right) = V_n^{(1)}, \tag{3.5}$$

where harmonically varying signals of frequency ω are assumed. Here Z_{01} is the complex self-impedance of each one of the elements. Z_1 is the purely imaginary mutual impedance between the neighboring elements, I_n is the current in and $V_n^{(1)}$ is the voltage applied to the n^{th} element.

Let us now consider a second linear array. Kirchhoff's equation may similarly be written as

$$Z_{02} J_n + Z_2 \left(J_{n-1} + J_{n+1} \right) = V_n^{(2)}, \tag{3.6}$$

where subscript 1 has now been replaced by subscript 2 and the current in the n^{th} element is denoted by J_n. The complex self-impedance of elements of each line has the form $Z_{0i} = R_i + j\omega L_i + 1/(j\omega C_i)$ with resistance R_i, self-inductance L_i and capacitance C_i $(i = 1, 2)$. The purely imaginary mutual impedance Z_i is equal to $j\omega$ times the mutual inductance M_i.

If the lines are close enough to each other their elements are coupled not only to the elements of their own lines but also to the elements of the other line, as may be seen in Fig. 3.12. Kirchhoff's equations must then be modified by adding the interaction terms due to mutual impedances $Z = j\omega M$, $Z_3 = j\omega M_3$ and $Z_4 = j\omega M_4$ to the left-hand sides of Eqs. (3.5) and (3.6) yielding

$$\begin{cases} Z_{01} I_n + Z_1 \left(I_{n-1} + I_{n+1} \right) + Z J_n + Z_4 J_{n-1} + Z_3 J_{n+1} = V_n^{(1)} \\ Z_{02} J_n + Z_2 \left(J_{n-1} + J_{n+1} \right) + Z I_n + Z_3 I_{n-1} + Z_4 I_{n+1} = V_n^{(2)} \end{cases} . \tag{3.7}$$

Our next aim is to find the dispersion equation, i. e. to relate the frequency ω to the wave number k, Eq. (2.10), $(k = \beta - j\alpha)$. We disregard the applied voltages and look for wave solutions in the form $I_n = I_0 \exp[j(\omega t - nka)]$ and $J_n = J_0 \exp[j(\omega t - nka)]$, where I_0 and J_0 are constants, ω is the frequency and a is the period of the lines. Eqs. (3.7) may then be recast in the form

$$\begin{cases} Z_{01} I_0 + 2j\omega M_1 I_0 \cos ka + j\omega \left(M + M_4 e^{jka} + M_3 e^{-jka} \right) J_0 = 0 \\ Z_{02} J_0 + 2j\omega M_2 J_0 \cos ka + j\omega \left(M + M_3 e^{jka} + M_4 e^{-jka} \right) I_0 = 0 \end{cases} . \tag{3.8}$$

Equations (3.8) have non-trivial solutions when the determinant of the coefficients of I_0 and J_0 vanishes yielding the relationship between ω and ka

$$(Z_{01} + 2j\omega M_1 \cos ka)\,(Z_{02} + 2j\omega M_2 \cos ka) = -\omega^2 \sigma(ka) \tag{3.9}$$

with the coupling coefficient

$$\sigma(ka) = M^2 + M_3^2 + M_4^2 + 2M\,(M_3 + M_4)\cos ka + 2M_3 M_4 \cos 2ka\,. \tag{3.10}$$

Note that we distinguish here between the coupling *coefficient* $\sigma(ka)$ in Eq. (3.10), which characterizes the overall coupling strength between the lines, and the coupling *constant* κ, which determines the coupling between the individual elements.

Equation (3.9) is clearly in the form of coupled wave equations [69, 72] with $\sigma(ka)$ as the coupling coefficient. If $\sigma(ka) = 0$ then the brackets on the left-hand side of Eq. (3.9) give the dispersion equations of the uncoupled lines.

Let us now discuss the properties of Eq. (3.9). It can be solved either for ω or for ka. In terms of $\cos ka$, Eq. (3.9) is an algebraic equation of the second order giving two solutions. This means that there are two (in general complex) values of ka corresponding to one real value of ω. Such situation was discussed by Brillouin [69]. For ω, it is a biquadratic equation. For the lossless case (self-impedances Z_{01} and Z_{02} have no real parts), we find that, as long as $\omega^2\sigma(ka)$ is positive, real values of ka give real values of ω leading to two branches of the dispersion characteristics

$$\omega_{1,2} = \sqrt{\frac{\omega_{01}^2\Gamma_2 + \omega_{02}^2\Gamma_1 \pm \sqrt{\left(\omega_{01}^2\Gamma_2 - \omega_{02}^2\Gamma_1\right)^2 + 4\dfrac{\omega_{01}^2\omega_{02}^2}{L_1L_2}\sigma(ka)}}{2\left(\Gamma_1\Gamma_2 - \dfrac{1}{L_1L_2}\sigma(ka)\right)}}\,, \tag{3.11}$$

where $\omega_{0i} = 1/\sqrt{L_iC_i}$ is the resonant frequency of the elements in line i and $\Gamma_i = 1 + (2M_i/L_i)\cos ka \equiv 1 + \kappa_i \cos ka$. The subscripts 1 and 2 in Eq. (3.11) refer to lines 1 and 2, but note that ω_1 and ω_2 denote the variations with frequency in branches 1 and 2 respectively.

It may be seen from Eq. (3.11) that the group velocity, $d\omega/dk$, is zero at the edges of the band, at $ka = 0$ and $ka = \pm\pi$, but it can also be zero within the Brillouin zone when the following equation is satisfied

$$\frac{\left[\frac{j}{\omega}(M_1Z_{02} + M_2Z_{01}) + M(M_3 + M_4)\right]^2}{4\,(M_3M_4 - M_1M_2)} = \frac{Z_{01}Z_{02}}{\omega^2} + M^2 + (M_3 - M_4)^2\,. \tag{3.12}$$

If Eq. (3.12) has real solutions for ω then it must refer to either a minimum or a maximum

of the dispersion curve $\omega(ka)$. The presence of such an extremum in one or both branches of the dispersion curve obviously means that the same branch may support both forward and backward waves for different ranges of ka. It is also known [73–75] that the presence of an extremum within the interval $0 < ka < \pi$ will give rise to complex modes.

In the stop bands, in the lossless case, ka is either purely imaginary or complex. Two limiting cases occur at $ka = 0 - j\alpha a$ and $ka = \pi - j\alpha a$. The decay is monotonic in the first case, whereas the sign of the amplitude alternates in the second case. They correspond to evanescent waves [69].

We shall now apply the developed theoretical formulation of coupled chains of metamaterial elements to a variety of configurations with the aim to tailor their near-field guiding properties. It is customary to put couplers into two distinct categories, co-directional and contra-directional, depending on whether the group velocities of the two lines are in the same or in opposite directions. In our case, MI waves allow us to choose for the unperturbed lines both forward (axial configuration) and backward (planar configuration) wave propagation [39]. The freedom in choosing the relative position of both chains will lead to a great variety of mutual coupling effects and would provide an additional flexibility in tailoring the dispersion characteristics of coupled MI waves. For simplicity, we shall from now on assume all elements to be identical, $Z_{01} = Z_{02} = Z_0$.

Coupled modes with co-directional and contra-directional power flow

For a detailed investigation, we have chosen configurations shown schematically in Fig. 3.13. The cases of interest are two coupled planar lines, (a) and (b), and coupled planar and axial line, (c) and (d). The unit cell in each case consists of two elements. The elements within the unit cell are exactly above each other in cases (a) and (c) and shifted by one half of a period in cases (b) and (d). The mutual inductances, taken as different from zero, are shown in Figs. 3.13 a-d for all four cases.

In cases (a) and (b), both lines, when uncoupled, support backward waves. For these cases, $M_1 = M_2 < 0$. In cases (c) and (d), one line is planar and the other one is axial. For these two configurations, the mutual inductances M_1 and M_2 have both different signs and absolute values, $M_1 < 0$ and $M_2 > 0$, so that one line supports backward and the other one forward waves.

In case (a), the identical planar lines are exactly above each other. As may be expected, the mutual inductances M_3 and M_4 do not greatly influence the coupling between the lines and can be neglected. The dispersion equation (3.9) reduces to

$$(Z_0 + 2j\omega M_1 \cos ka)^2 = -\omega^2 M^2 \ . \tag{3.13a}$$

In case (b), when the two planar lines are shifted relative to each other by one half of the period $M_3 = M$ for symmetry reasons, while M_4 can be neglected. The dispersion relation is

$$(Z_0 + 2j\omega M_1 \cos ka)^2 = -2\omega^2 M^2 (1 + \cos ka) \ . \tag{3.13b}$$

In case (c), the planar and axial lines are exactly above each other. Since the planes of the loops within the unit cell are perpendicular to each other, the mutual inductance within

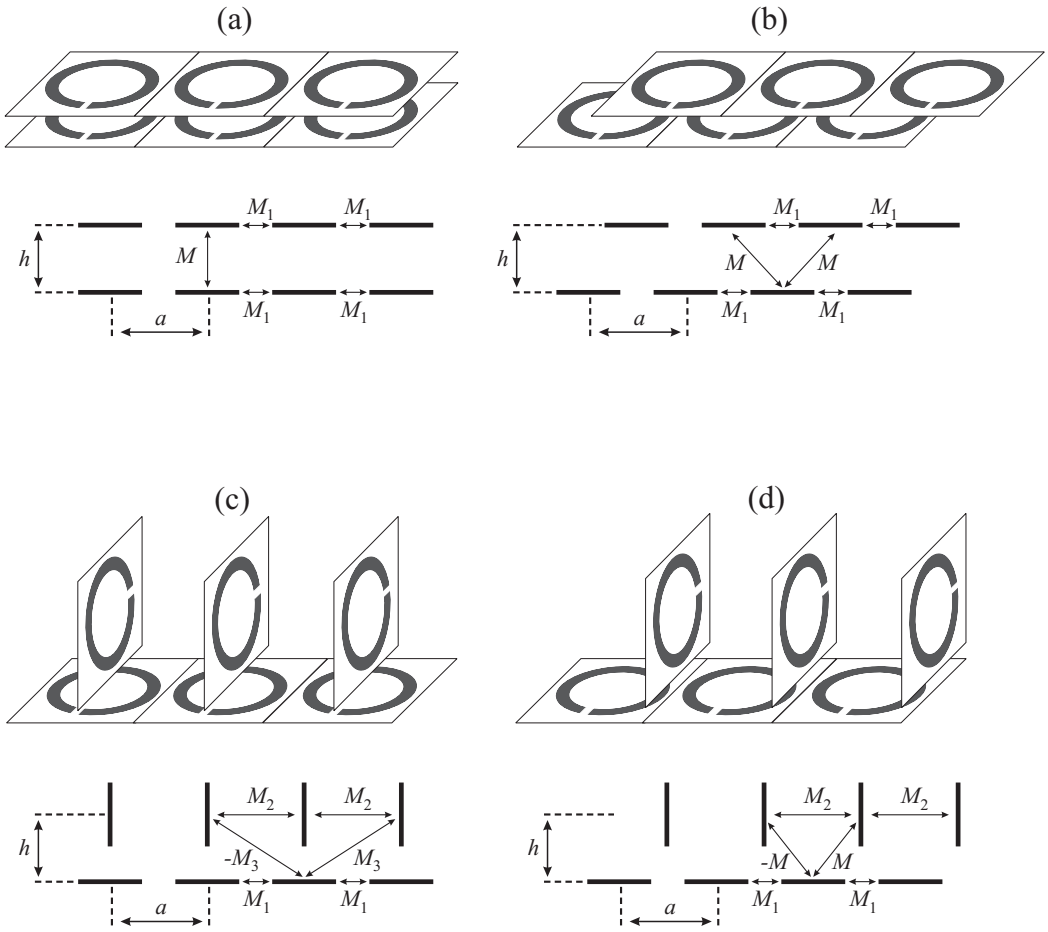

Figure 3.13: *Configurations of diatomic metamaterial structures with co-directional* (a,b) *and contra-directional* (c,d) *power flow:* (a) *planar lines above each other,* (b) *shifted planar lines,* (c) *planar and axial line above each other,* (d) *shifted planar and axial lines. The non-zero mutual inductances are shown by arrows.*

the unit cell, M, is zero so that interaction takes place via M_3 and M_4 which have equal absolute values and opposite signs, $M_4 = -M_3$. The dispersion equation is of the form

$$(Z_0 + 2j\omega M_1 \cos ka)\,(Z_0 + 2j\omega M_2 \cos ka) = -2M_3^2\omega^2\,(1 - \cos 2ka)\ . \tag{3.13c}$$

In case (d), the planar and the axial lines are in the half-period-shifted configuration. In this case, $M_3 = -M$ while M_4 can be neglected. The corresponding dispersion equation is of the form

$$(Z_0 + 2j\omega M_1 \cos ka)\,(Z_0 + 2j\omega M_2 \cos ka) = -2\omega^2 M^2\,(1 - \cos ka)\ . \tag{3.13d}$$

We now illustrate the properties of the dispersion relations Eqs. (3.13a)-(3.13d) choosing as an example a set of parameters relevant to the actual realization of the elements used

in our experiments. We choose $f_0 = \omega_0/(2\pi) = 46.2$ MHz corresponding to a magnetic field close to 1 T in Magnetic Resonance Imaging applications. The radius of the element is taken as $r_0 = 10$ mm. The losses are characterized by the quality factor of $Q = 105$. The stop bands are indicated by a significant increase of the attenuation constant.

For a clearer comparison of dispersion relations, we choose for all four configurations the same period a and the same distance h between the two lines (see Figs. 3.13 a-d). Note that the distance between neighboring elements within a planar line cannot be smaller than $2r_0$. We shall choose $a = 24$ mm close to this minimum. The distance between the planar and the axial line cannot be smaller than r_0. We shall choose $h = 15$ mm.

The dispersion characteristics (3.13a)-(3.13d) with propagation and attenuation constants versus frequency for the four diatomic configurations are plotted in Figs. 3.14 a-d. The dashed lines show the dispersion curves for the unperturbed lines (with the interaction between the lines switched off, $M = M_3 = M_4 = 0$), whereas the solid lines are for the coupled lines.

In case (a), two planar lines are exactly above each other. Since the lines are identical, the unperturbed dispersion characteristics (dashed line) must be identical as well. The unperturbed dispersion equation describes a backward wave corresponding to the coupling constant $\kappa_1 = -0.09$ with the pass band given by $(1-\kappa_1)^{-1/2} < \omega/\omega_0 < (1+\kappa_1)^{-1/2}$. In the presence of coupling between the lines, one dispersion curve (black solid line) moves upwards and the other one (grey solid line), downwards, as may be clearly seen from Fig. 3.14 a. The separation in frequency between the two branches is determined by the strength of the coupling constant κ, which for the chosen parameters has the value $\kappa = 0.19$. The separation in frequency remains the same for all values of β; this conclusion follows also from the form of Eq. (3.13a) with the right-hand side independent of k. For the chosen parameters, the interaction between the lines is so large that the two branches are separated by a complete stop band. It could be expected that if the distance h between the lines were larger, the interaction between the lines would be weaker and the separation between the two branches would not result in a complete stop band between them. In such a case, we would expect the behavior typical for couplers: two values of β for a single ω leading to a beating of two signals. This prediction shall be checked in Section 3.3.2 where we discuss experimental results.

In case (b), the identical planar lines are shifted relative to each other by half a period. The unperturbed dispersion equation of course does not change, but the behavior of the dispersion equations for coupled lines changes drastically in comparison with case (a). It can be seen from the right-hand side of Eq. (3.13b) that the coupling coefficient (and consequently the interaction process) between the MI waves is now different within the Brillouin zone itself: it is maximum at $\beta a = 0$ and is absent at $\beta a = \pi$. It may, therefore, be expected that the amount of split depends on βa. This is indeed what happens as may be seen in Fig. 3.14 b. For the parameters chosen, the coupling constants are $\kappa_1 = -0.09$ and $\kappa = 0.1$. The resulting two branches are very different from each other. The interaction results in an upper branch with a larger width than in the unperturbed case (black solid line) and in a lower branch with a smaller width (grey solid line). There is a noticeable minimum at the lower edge of the pass band. This means that forward waves may also exist for a

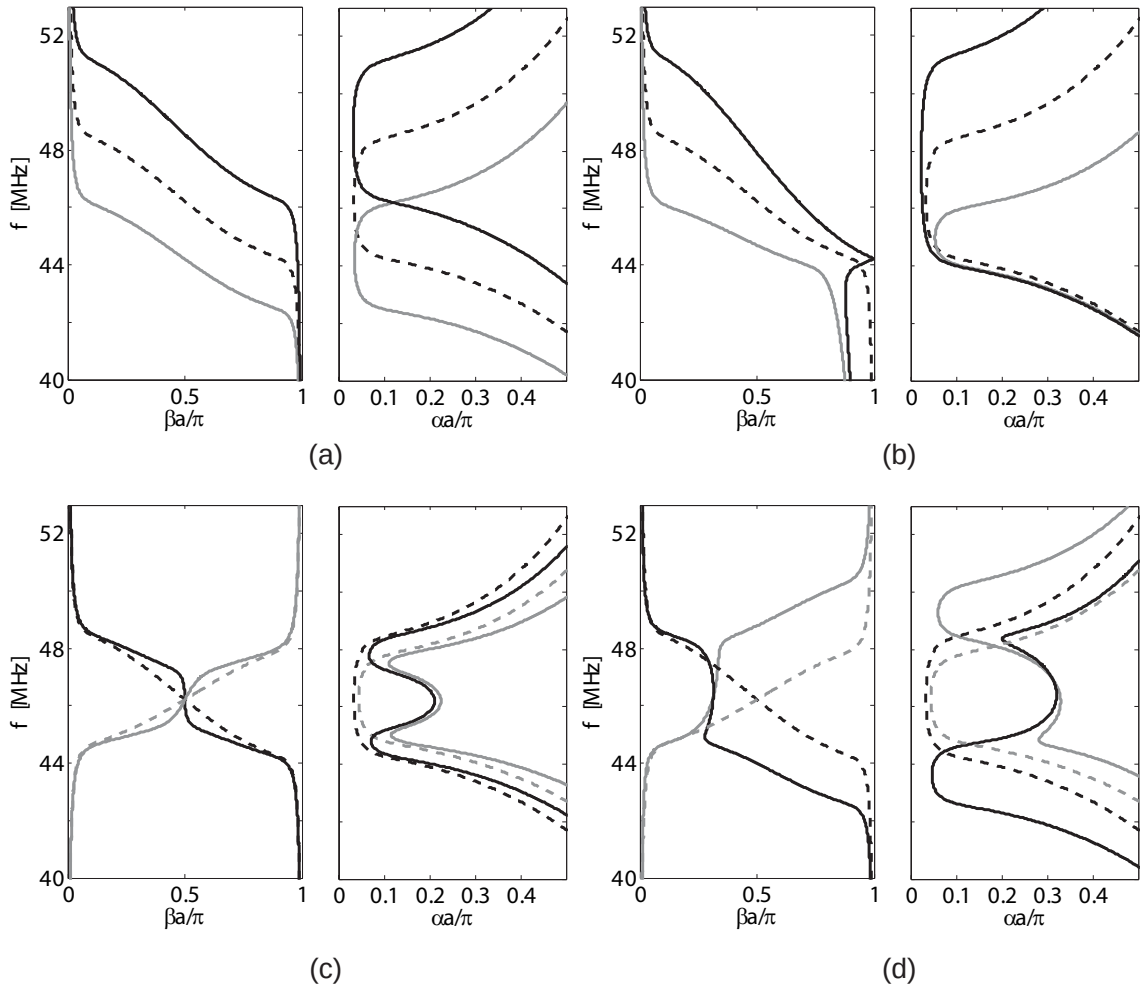

Figure 3.14: *Dispersion characteristics of the coupled lines of Fig. 3.13. Dashed lines show the unperturbed dispersion curves.*

certain range of frequency. The probable physical reason is that the mutual inductance M is positive and large enough to suppress the negative mutual inductance M_1. The position of the minimum may be obtained from Eq. (3.13b) as follows

$$\frac{\omega}{\omega_0} = \left(1 - \kappa_1 - \frac{\kappa^2}{8\kappa_1}\right)^{-1}, \quad \cos ka = \frac{\kappa^2}{8\kappa_1^2} - 1\,. \tag{3.14}$$

Below this point, the propagation and attenuation constants represent the complex modes. Note that we take $|\beta a|$ so that waves propagating in different directions are in the same half of the Brillouin zone.

In case (c), the planar and axial lines are exactly above each other. The interaction mechanism in this case is quite different from the cases of two planar lines (a) and (b). The two unperturbed dispersion curves show a backward wave for the planar line (black dashed

line in Fig. 3.14 c) and a forward wave for the axial line (grey dashed line in Fig. 3.14 c). These curves correspond to the coupling constants $\kappa_1 = -0.09$ and $\kappa_2 = 0.07$. Since $|\kappa_1| > |\kappa_2|$, the pass band of the backward wave in the planar line 1 is slightly wider than the pass band of the forward wave in the axial line 2. The unperturbed dispersion curves cross at $\beta a = \pi/2$, which can be regarded as a point of degeneracy. The interaction between the lines is governed by relatively weak coupling constants $\kappa_{3,4} = \pm 0.05$. As can be seen from Eq. (3.13c) the interaction is absent for $ka = 0, \pi$ where the unperturbed dispersion curves are far away from each other and it is maximum for $ka = \pi/2$, at their crossing point. The resulting dispersion curves show the split of the pass band into two with a stop band around the point of degeneracy. The coupled dispersion curves are quite close to the unperturbed ones except in the vicinity of the degenerate point $\beta a = \pi/2$, where complex modes of high attenuation appear. In both pass bands, there are frequency regions with two values of βa for a single ω which would result in a beating of two signals. Contrary to case (a) with two backward waves, we have here a contra-directional mode where both forward and backward waves can simultaneously propagate.

In case (d), the planar and axial lines are in the half-period-shifted configuration. The unperturbed dispersion curves (dashed lines in Fig. 3.14 d) are the same as for the unshifted configuration (c). The coupling mechanism governed by the coupling constants $\kappa = -\kappa_4 = 0.15$ changes drastically in comparison with case (c). As may be seen from Eq. (3.13d), the interaction is zero for $ka = 0$ and maximum for $ka = \pi$. The resulting dispersion in Fig. 3.14 d shows two complex pass bands supporting both forward and backward waves with the separation between the two branches increasing with βa. Another consequence of the interaction between the lines, which is varying within a Brillouin zone, is that the degenerate point is not at $\beta a = \pi/2$, as in the previous case, but shifts towards smaller values of βa. The attenuation of the two modes (solid black and grey lines in Fig. 3.14 d) is different within the pass bands: for the lower one, the backward-wave mode (black line) has lower attenuation, whereas for the upper pass band, the forward wave dominates.

To sum up, in addition to the two classical types of hybrid modes for coupled waves on unshifted lines, cases (a) and (c), we have also observed two novel hybrid modes for the half-period shifted lines, where the interaction is strongly dependent on the propagation constant. In case (b), maximum interaction is at $\beta a = 0$ and zero at $\beta a = \pi$, whereas for case (d) the points of maximum and zero interaction are reversed.

3.3.2 Experiment

A series of experiments was performed[4] in order to check the validity of our theoretical approach.

[4]The experiments were carried out at Oxford University by Dr. A. Radkovskaya (Moscow University), Mr. G. Faulkner, Dr. C. J. Stevens and Prof. D. J. Edwards (Oxford University).

Dispersion equations

The elements used in the experiments are capacitively-loaded split pipes, whose parameters have been described in detail in Section 3.1. The waveguiding properties of the four diatomic metamaterial configurations Figs. 3.13 a-d were analyzed arranging the elements into two lines each containing 16 elements. The photographs of the experimental configurations are shown in Fig. 3.15. The period a was kept to be 24 mm in all cases; for the distance h between the lines, three values were chosen for each configuration: $h = 10,\ 15,\ 20$ mm for cases (a) and (b) and $h = 15,\ 20$ and 30 mm for cases (c) and (d). The first element of line 1 was excited by a transmitting loop, and the frequency dependence of the currents in all elements was measured as the receiving loop was moved first along line 1 and then along line 2. The measurements were performed at 1601 frequency points for the range $34 - 58$ MHz with the aid of a network analyzer of the type HP8753C.

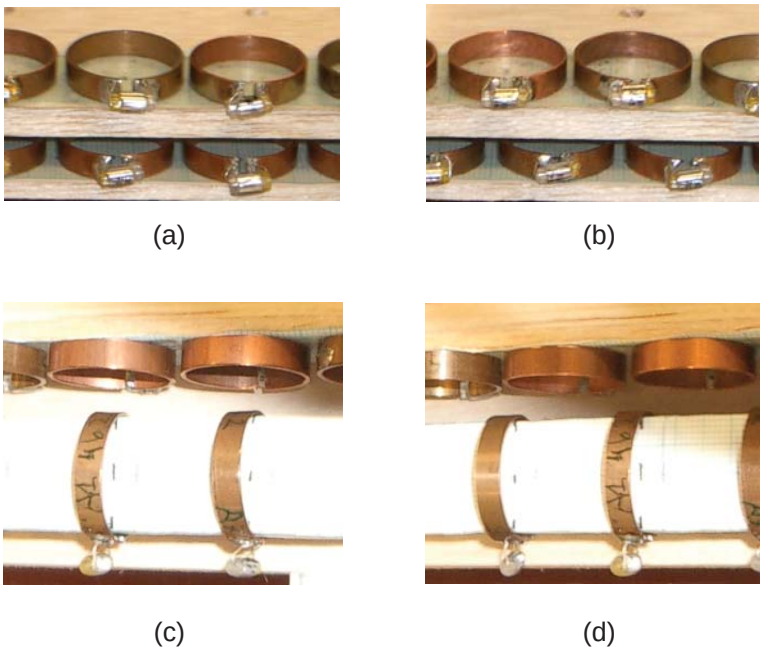

Figure 3.15: *Photographs of diatomic metamaterial structures:* (a) *planar lines above each other,* (b) *shifted planar lines,* (c) *planar and axial line above each other,* (d) *shifted planar and axial lines.*

To extract the dispersion equations for the coupled lines we used the following procedure. We assume that for each frequency ω the structure supports two modes with two complex values of ka. We should take into account that the structure has a finite length and that there are reflected waves as well. Then the currents in line 1 and line 2 can be written as

$$\begin{aligned} I_n &= a_1 \exp(-jnk_1a) + b_1 \exp(jnk_1a) + a_2 \exp(-jnk_2a) + b_2 \exp(jnk_2a) \\ J_n &= c_1 \exp(-jnk_1a) + d_1 \exp(jnk_1a) + c_2 \exp(-jnk_2a) + d_2 \exp(jnk_2a) \end{aligned} \quad . \tag{3.15}$$

k_1a and k_2a can thus be found from an algebraic expression containing values of any 6 neighboring currents within either line 1 or line 2. Following a similar procedure the unperturbed dispersion equations can be found from current measurements on isolated lines. Assuming in this case a single mode and its reflected wave, the dispersion equation can be extracted from the values of any three neighboring currents of the line.

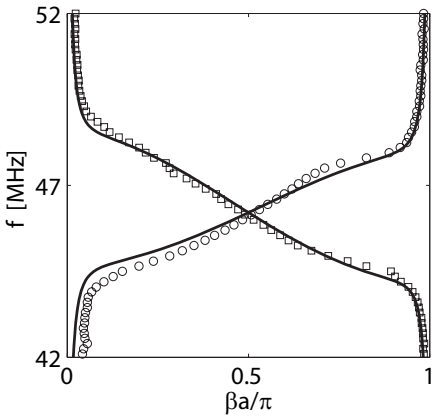

Figure 3.16: *Dispersion characteristics of the uncoupled planar and axial lines: theory (solid lines) and experiment (circles and squares).*

Figure 3.16 shows the dispersion curves for the case of uncoupled lines supporting backward and forward waves. The agreement between the experimental and theoretical values may be seen to be excellent. Figures 3.17 and 3.18 give a summary of the dispersion curves for each one of the coupled configurations. The first and second columns of Fig. 3.17 are for $h = 20$, 15 and 10 mm for unshifted and shifted planar-planar configurations. The first and second columns of Fig. 3.18 show the dispersion curves for $h = 30$, 20 and 15 mm for unshifted and shifted planar-axial configurations. In each of the four columns, the top figure corresponds to the largest separation between the lines and thus to the weakest interaction; the bottom figure corresponds to the smallest separation and thus to the strongest interaction. Comparing the figures in each column we can clearly see the different characters of the respective coupling mechanisms.

For the first, (a), column of Fig. 3.17, when two planar lines are exactly above each other (Fig. 3.13 a), the unperturbed dispersion curve splits into two similar branches; the separation between the branches grows as the distance, h, between the lines decreases.

For the second, (b), column of Fig. 3.17, when the planar lines are half-period shifted relative to each other, the upper branch is a backward-wave branch with a a larger width, and the lower branch supports both forward and backward waves with a minimum within a Brillouin zone (Fig. 3.13 b). The separation between the branches depends strongly on the propagation constant; it is maximum for $\beta a \to 0$ and minimum for $\beta a \to \pi$.

For the first, (a), column of Fig. 3.18, when the planar and the axial lines are exactly above each other (Fig. 3.13 c), the interaction between the backward and the forward wave of Fig. 3.16 results in a stop band around the resonant frequency. The coupled dispersion curves differ from the unperturbed ones mostly in the vicinity of the crossing point $\beta a = \pi/2$. The smaller the separation between the lines, the better pronounced is the effect.

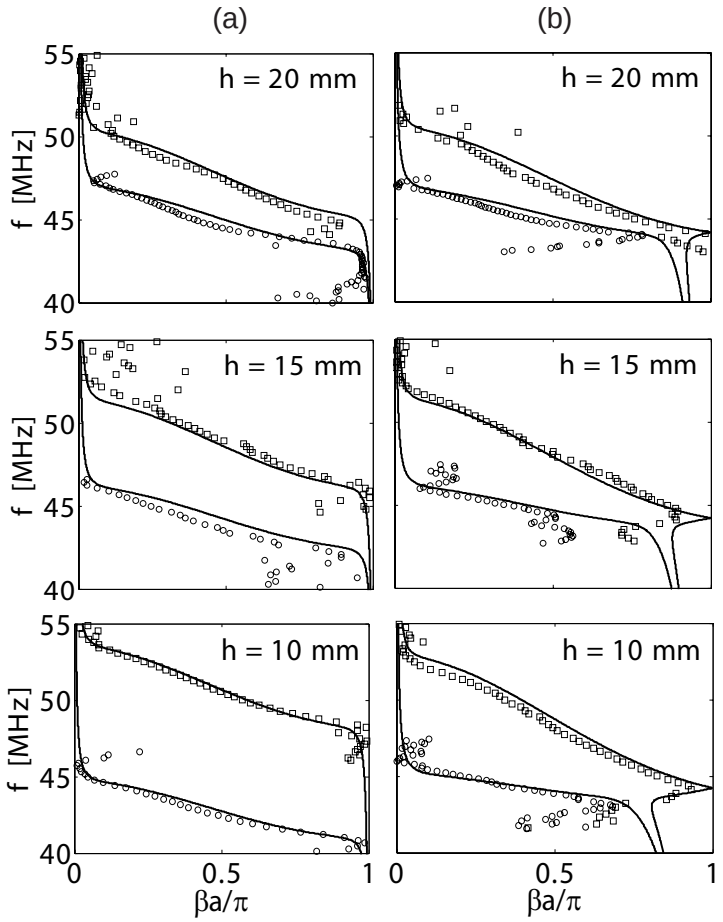

Figure 3.17: *Dispersion characteristics of the coupled lines: Theory (solid lines) and experiment (circles and squares). Unshifted* (a) *and shifted* (b) *planar-planar lines with* $h = 20$, *15, 10 mm.*

For the second, (b), column of Fig. 3.18, when the planar and the axial line are half-period shifted relative to each other, the separation between the branches depends strongly on the propagation constant (Fig. 3.13 d). The separation is maximum for $\beta a \to \pi$ and minimum for $\beta a \to 0$. The degenerate point may be seen to be around $\beta a = \pi/2$ for the distance $h = 30$ mm between the lines and it moves to the left as the distance between the lines decreases.

The agreement between theory and experiment may be seen to be very good in the pass bands in each one of the twelve diagrams of Figs. 3.17 and 3.18. Note that the experimental points in the stop bands have been derived from signals with magnitudes close to the noise level due to high attenuation, so they are probably spurious.

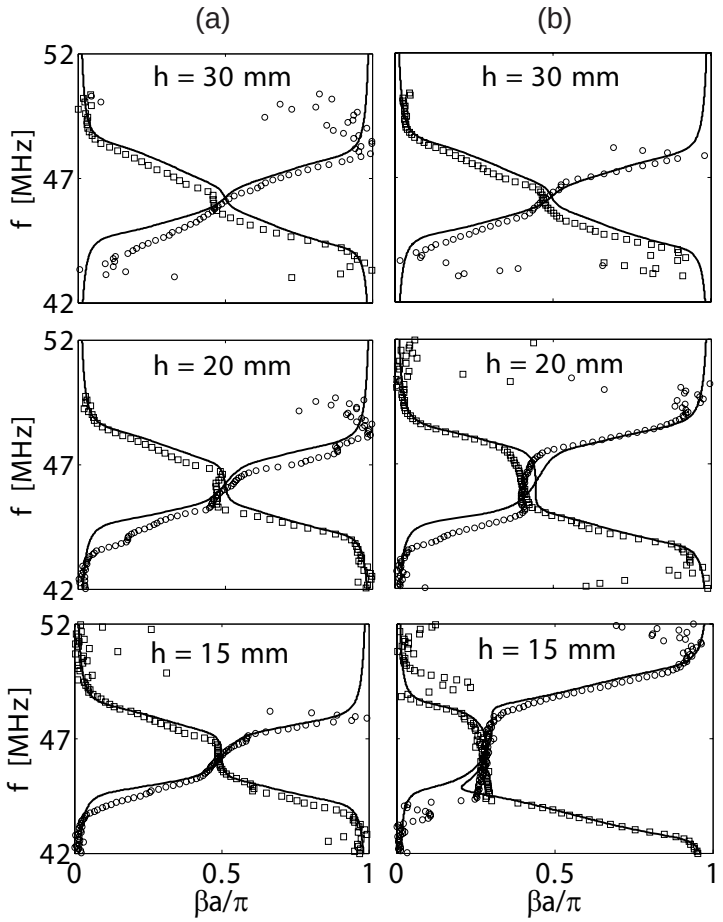

Figure 3.18: *Dispersion characteristics of the coupled lines: Theory (solid lines) and experiment (circles and squares). Unshifted* (c) *and shifted* (d) *planar-axial lines with* $h = 30$*, 20, 15 mm.*

Validity of nearest neighbor approximation

The theoretical curves were obtained in the approximation of nearest-neighbor interactions, where each element interacts with up to five neighbors (see Fig. 3.12). As an additional check of the validity of the model, we also performed numerical simulations modeling the signal propagation in the structures by taking all interactions into account. Figure 3.19 shows the power distributions along the structure for the unshifted planar-planar configuration with a separation between the lines $h = 20$ mm at the frequency $f = \omega/(2\pi) = 45.8$ MHz, which is close to the resonant frequency of the individual elements. Figures 3.19 a and 3.19 b show the distribution of detected power along line 1 and 2 respectively. The squares are the experimental values, the diamonds are the values obtained from the analytical theory with nearest neighbor interactions, and the circles are the numerical simulation values from impedance matrix calculation (see Section 2.3) taking all interactions into account. The agreement between experiment, theory, and numerical results may be seen to be good. The

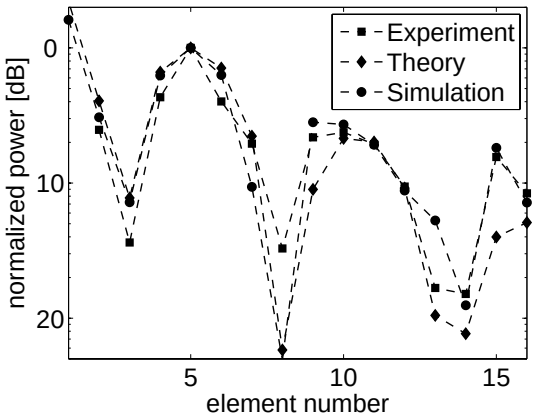

(a)

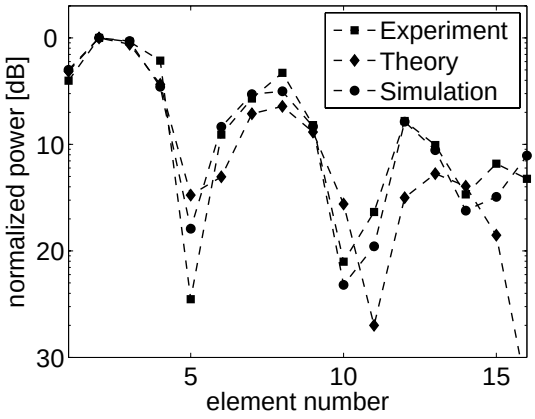

(b)

Figure 3.19: *Power distribution along the excited line 1* (a) *and along line 2* (b) *for the unshifted planar-planar configuration.* $h = 20$ *mm,* $f = 45.8$ *MHz. Experiment (squares), analytical theory with nearest-neighbor approximation (diamonds), numerical simulation from impedance matrix calculation including all interactions (circles). The lines connecting the symbols serve as a guide to the eye.*

beatings of the signals in line 1 and line 2 are in anti-phase, as the energy is transferred from line 1 to line 2 and back. At the frequency chosen, the two lines act as a co-directional coupler (Fig 3.17 a, $h = 20$ mm), and the corresponding values of the propagation constant are, from Eq. (3.13a), $\beta_1 a = 0.36\pi$ and $\beta_2 a = 0.73\pi$. The coupling length characterizing the period of energy transfer is $\Lambda = \pi/|\beta_1 - \beta_2|$. This gives the period of the energy exchange as about five elements.

A similar agreement between the calculated and measured values of current amplitudes within the structure is obtained for all configurations for frequency values corresponding to the pass bands.

Chapter 4

Linear applications

In the previous Chapter, we have developed a mechanism for tailoring the dispersion properties of MI waves with diatomic metamaterial arrays. We proceed now with a discussion of how this and other tailoring ideas can be employed for a number of potential applications. We shall consider here linear arrays, preserving the nonlinear case for the next Chapter.

We start in Sections 4.1 and 4.2 with two effects, shift-dependent transmission and subwavelength imaging, where diatomic arrays are employed for controlling the propagation of MI waves at the specified frequencies. Tailoring the subwavelength focus by metamaterial "lenses" – an issue closely related to subwavelength imaging – is discussed in Section 4.3. Finally, in Section 4.4, we consider rotational resonance of MI waves in ring metamaterial arrays, which can be beneficially used for signal detection in Magnetic Resonance Imaging.

4.1 Shift-dependent transmission

In the previous Chapter, we could see that the dispersion properties of diatomic configurations consisting of two planar lines exactly above each other differ significantly from the half-a-period shifted configuration (see Figs. 3.13 a,b and Figs. 3.14 a,b). It is natural, therefore, to expect that by changing the amount of shift between the lines we could acquire some control over their properties and behavior.

Our aim in this Section is to investigate in detail both theoretically and experimentally the properties of two metamaterial lines when one of them is mechanically shifted relative to the other one. The theoretical analysis is based on the coupled-modes approach for diatomic arrays (Section 3.3) and on the impedance matrix formalism (Section 2.3).

4.1.1 Experiment

Two different kinds of metamaterial elements were used in the experiments[1], capacitively-loaded split pipes and spirals. The split pipes are the same as described in Section 3.1

[1]The experiments were carried out at Oxford University by Dr. A. Radkovskaya (Moscow University), Mr. G. Faulkner, Dr. C. J. Stevens and Prof. D. J. Edwards (Oxford University).

(see Fig. 3.2 and the text therewith). Their resonant frequencies and quality factors are $f_0 = \omega_0/(2\pi) = (46.2 \pm 0.2)$ MHz and $Q = 105 \pm 5$, respectively.

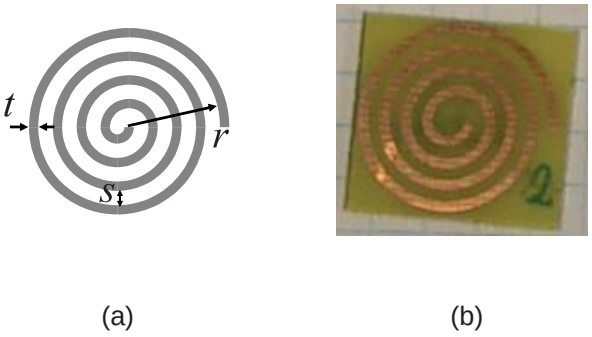

Figure 4.1: *Schematic presentation of the spiral resonator* (a) *and its photograph* (b).

The elements of the second type are four-turn spiral resonators [41, 42] produced on a printed circuit board (type FR 4) by selective etching. The radius, run width of the spiral, and the separation between the turns are $r = 9$ mm, $t = 0.9$ mm, and $s = 1.35$ mm as may be seen in Fig. 4.1 a. The photograph of the element is shown in Fig. 4.1 b. The resonant frequencies and quality factors of the spirals, measured with the aid of a network analyser of the type HP8753C, were found as $f_0 = (0.586 \pm 0.004)$ GHz and $Q = 49 \pm 4$.

The measurements of the coupling constant, κ, between two split pipes in different configurations have been presented in Section 3.1. For the spirals, additional measurements were performed in axial and planar configurations at 1601 values of frequency between 0.3 and 0.9 GHz. The coupling constant in the planar arrangement for a distance of $a = 19$ mm between the elements' centers was found as $2M_{\parallel}/L = -0.06$. In the axial configuration, the coupling constant was measured at distances $h = 5$ mm and $h = 10$ mm yielding $2M_{\perp}/L = 0.42$ and $2M_{\perp}/L = 0.14$, respectively.

For each kind of elements, two planar lines consisting of 13 elements were produced. The split-pipes were placed on a piece of balsawood with a period $a = 24$ mm between the centers of nearest neighbors. The arrays of spirals were produced on two pieces of a printed circuit board with a period $a = 19$ mm.

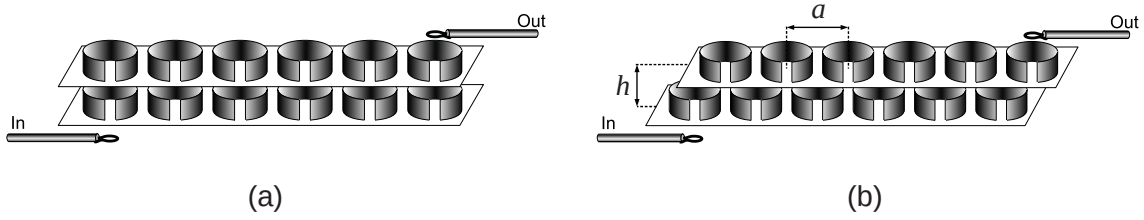

Figure 4.2: *Schematic presentation of the* (a) *unshifted and* (b) *half-a-period shifted diatomic array. The first element of the lower line is excited by a transmitting coil and the signal in the last element of the upper line is measured by a receiving coil.*

Arrays of identical elements were placed exactly above each other so that the first elements of the upper and lower arrays were in an axial configuration as shown in Fig. 4.2 a for split pipes. The first element of the lower array was excited by a transmitting coil, and the signal in the last element of the upper array was measured by a receiving coil. The aim of the experiment is to measure the ratio of the output to input power under the conditions when the upper array together with the receiving coil is mechanically shifted by different amounts, Δ, relative to the lower one. This is shown again for the split-pipes for a shift of half a period, $\Delta = a/2$, in Fig. 4.2 b. The transmission as a function of frequency was then measured for a large number of shifts.

The measurements of the split-pipe arrays were performed for a spacing of $h = 10$ mm between the arrays. They were shifted over a total distance of $\Delta = 80$ mm relative to each other in steps of 2 mm, and the transmission was measured in the frequency range $34 - 58$ MHz at 1601 discrete frequency points. The same experiments were conducted for the spiral arrays but for two different spacings, $h = 5$ mm and 10 mm respectively. For both experiments, the upper array was shifted again over a total distance of 80 mm in steps of 2 mm. The measurements were performed at 1601 discrete values of frequency between 0.3 and 0.9 GHz.

4.1.2 Theory

The present experimental results could be modeled by a theory based on a combination of nearest neighbor interactions and coupling between the arrays. However, since the coupling between the arrays changes with the amount of shift, for a quantitative model, we decided to resort to the impedance matrix, Eq. (2.16), which takes into account interaction between any two elements wherever they are. This can be done if all the elements of the impedance matrix are known. The impedance matrix, $\mathbf{Z}$, has a dimension of $N \times N$, where N is the total number of elements, 26 in our case.

We have measured the resonant frequencies and quality factors of all the elements thus we know the diagonal elements of $\mathbf{Z}$ at all the frequencies considered. As for the mutual impedances, we have a number of experimental data for split pipes (see Section 3.1) and only three values for the spirals. The approach of modeling actual elements by loops has been proven in Section 3.1 to adequately describe experiments for two different kinds of elements. It is, therefore, reasonable to employ it here as well for determining the rest of the mutual impedances. We assumed that the elements may be modeled by loops with a radius equal to the radius of the actual elements (10 mm for the split-pipes and 9 mm for the spirals). It is then possible to calculate the mutual inductances between any two elements. This is quite a simple calculation for the split-pipe arrays in which both the period and the total length of the structure are much smaller than the free-space wavelength at the operating frequencies. The retardation effects can then be neglected, and consequently the mutual impedance between the elements is purely imaginary, i. e. only the mutual inductance, due to the magnetic coupling, is significant. For the spiral arrays, the situation is different: the free space wavelength of about 50 cm is still much larger then the period ($a = 19$ mm), but the total length of the arrays is above half a wavelength when fully extended. Therefore,

for more accurate calculations, retardation effects have to be taken into account [52, 53]. In the presence of retardation, the mutual inductance acquires an imaginary part, and the decline of its real part with distance is less steep. Since the calculated values of the mutual impedances agreed well with those measured (for nearest neighbors as described above), we could assume that all the mutual inductances calculated from our model were close to the actual ones. Knowing both the voltage vector, $\mathbf{V}$, and the impedance matrix, $\mathbf{Z}$, we could determine the currents in each element for all frequencies and shifts by inverting numerically the relationship (2.16).

4.1.3 Results

We shall now plot the experimentally obtained values of the transmission and compare them with theoretical results. For split pipes, these are shown in Figs. 4.3 a and b. The power transmitted from the first element of the lower array to the last element of the upper array is normalized to its value for zero shift and is shown as a contour plot. It may be seen that within a certain frequency range near the resonant frequency of the elements the transmission varies greatly with the shift. Transmission is minimum when the shift is zero, one period, two periods, etc., and it is maximum when the shift is half a period, one and a half period, etc. The effect of the shift is quite radical: the difference between maximum and minimum transmission may be as much as 60 dB. The agreement between theory and experiment may be seen to be good in the whole frequency region.

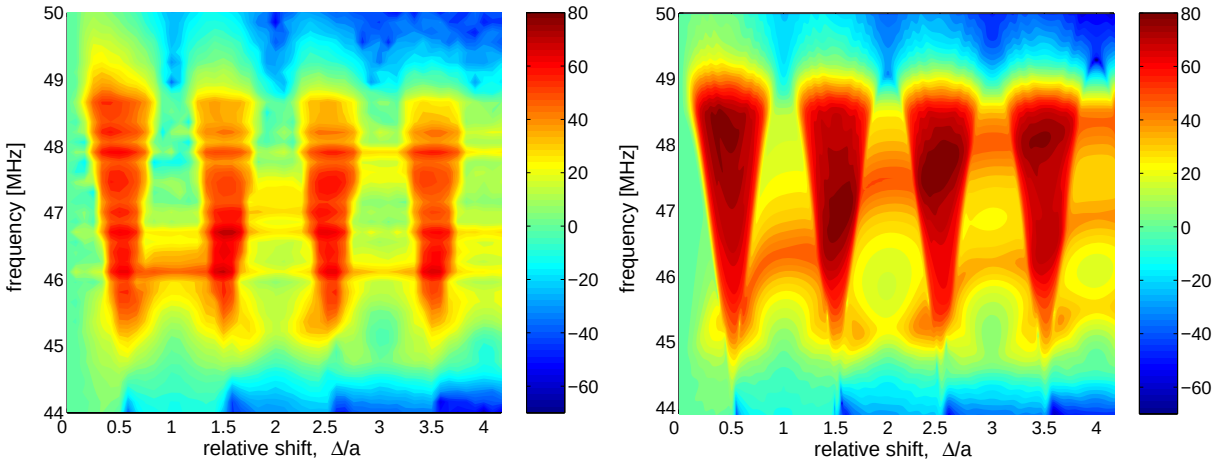

(a) (b)

Figure 4.3: *Contour plots of transmission between the lines of split-pipes ($h = 10$ mm) as a function of frequency and shift,* (a) *experiment,* (b) *theory.*

In order to show the results in a more comparable and more quantitative form we plotted the experimental (filled circles) and theoretical values of the transmission (solid line) as a

function of shift at two discrete frequencies in Figs. 4.4 a and b. The curves are normalized to the value of transmission at zero shift. The two selected values of frequency are the resonant frequency, $f = 46.2$ MHz, and one above it, $f = 48$ MHz. The agreement may be seen to be remarkably good.

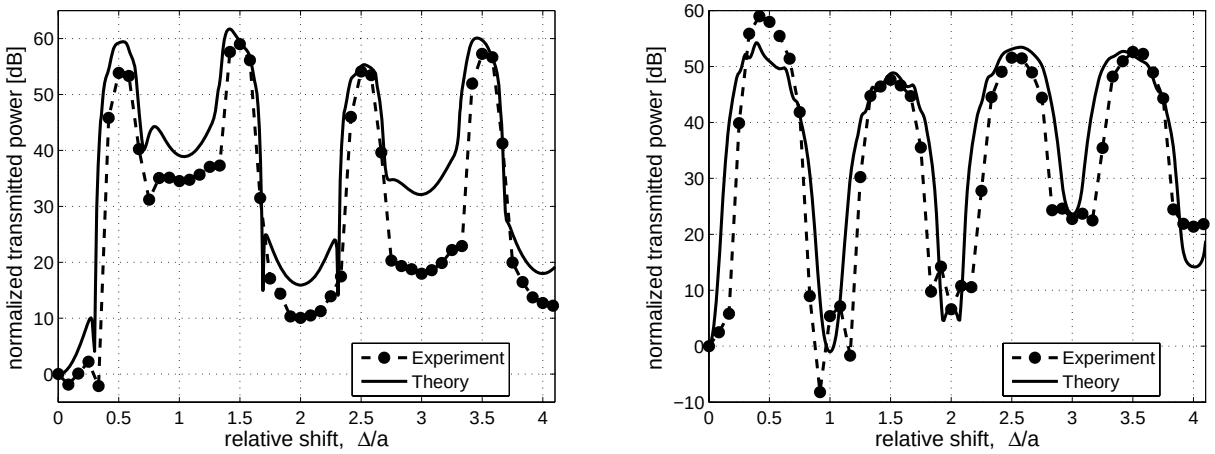

(a) (b)

Figure 4.4: *Transmitted power as a function of the shift between two lines of split-pipes, for different values of frequency,* (a) $f = 46.2$ *MHz,* (b) $f = 48.0$ *MHz. Dashed line with filled circles denotes experiment, solid line theory.*

The transmission results for the arrays made up by spirals are presented in Figs. 4.5 and 4.6 again in the form of contour plots for $h = 5$ mm and 10 mm respectively. It is gratifying to note that although the operating frequencies for these measurements are approximately ten times larger than those for split-pipes, the transmission of the spiral arrays (both for $h = 5$ mm and 10 mm) has a similar variation with shift: the regions of low and high transmission occur again for full-period and half-period shifts. The shape of high transmission regions is also similar: wider for the higher and narrower for the lower frequencies. The agreement appears to be better for $h = 5$ mm than for 10 mm. The possible explanation is that the latter configuration is more affected by retardation, and the model (replacing the actual elements by loops) is bound to be less accurate when retardation is present.

4.1.4 Tailoring the transmission

Let us now give a qualitative explanation of the transmission variation with the shift that is based on the theory of coupled MI waves developed in the previous Chapter. For this purpose, we choose the array made up by split pipes. The dispersion curves of MI waves for a lossless case are shown in Fig. 4.7 for three different values of shift between the lines:

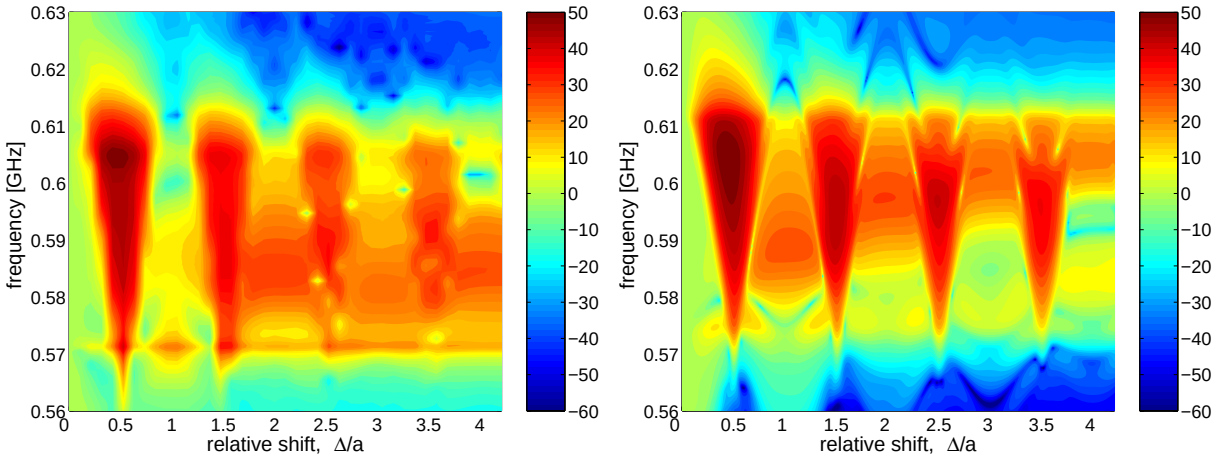

(a) (b)

Figure 4.5: *Contour plots of transmission between the lines of spirals ($h = 5$ mm) as a function of frequency and shift,* (a) *experiment,* (b) *theory.*

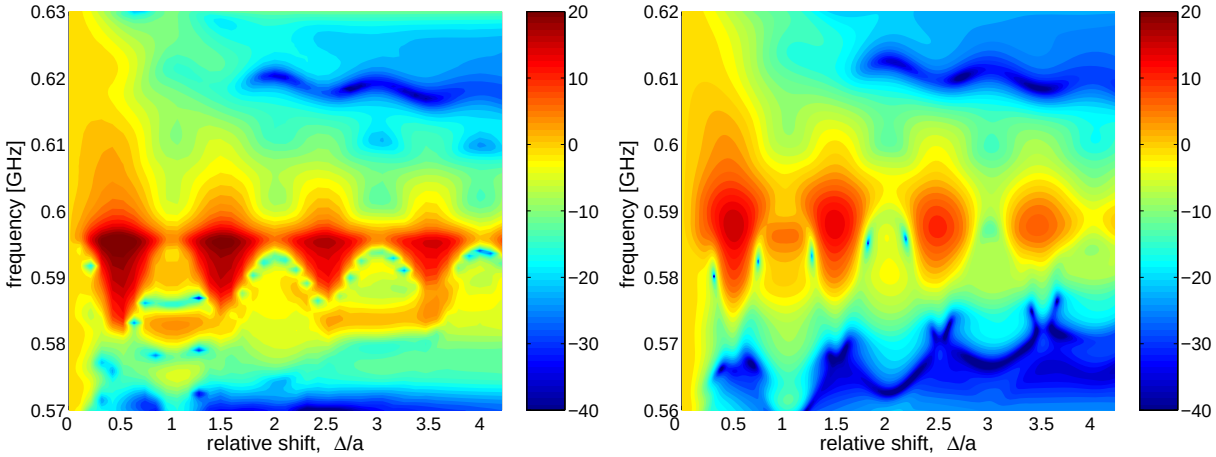

(a) (b)

Figure 4.6: *Contour plots of transmission between the lines of spirals ($h = 10$ mm) as a function of frequency and shift,* (a) *experiment,* (b) *theory.*

no shift (a), 0.35a-shift (b), and half a period shift (c). The horizontal dashed lines indicate the resonant frequency, 46.2 MHz. As can be seen from Fig. 4.7 a, when the lines are not shifted relative to each other (or shifted by an integer number of periods) the resonant frequency lies in a stop band of the dispersion characteristics. Consequently, MI waves do not propagate along the arrays and transmission is low. For the value of shift of 0.35a, the

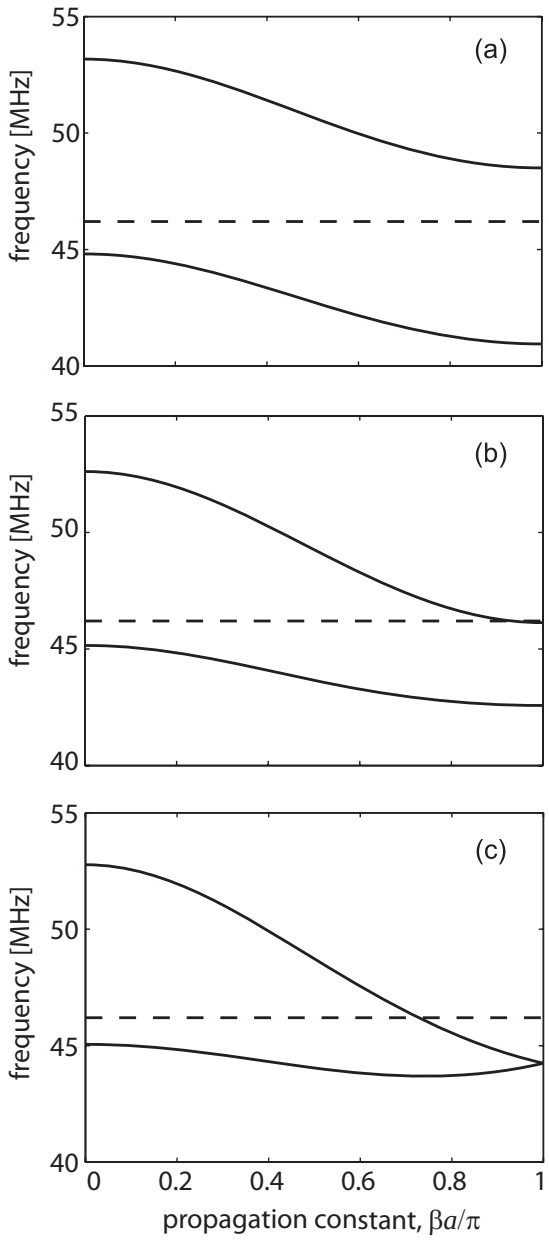

Figure 4.7: *Dispersion of the magnetoinductive waves for arrays made up by split-pipes* (a) *non-shifted*, (b) *shifted by 0.35 of the period, and* (c) *shifted by half of the period. No transmission at the resonant frequency (dashed lines) in case* (a), *abrupt increase of the transmission in case* (b), *and high transmission in case* (c).

resonant frequency lies at the edge of the pass band (see Fig. 4.7 b); this is the amount of shift when the transmission between the lines should undergo an abrupt change. Indeed, as seen in Fig. 4.4 a, in the vicinity of this point, the transmission between the lines increases up to 50 dB. The resonant frequency is close to the middle of the pass band for the shift of one half of the period (see Fig. 4.7 c). The losses are lower in the middle of the pass band than at its edges and, therefore, the transmission is bound to be higher. It also follows from this qualitative model that around 42 MHz transmission varies in an entirely different manner, as may be seen from Figs. 4.7 a-c: it is high for shifts corresponding to the whole

period and low for half-period shifts. The effect is, however, less pronounced due to high losses at frequencies far from the resonant one.

We see, therefore, that the key to understanding the transmission variation with shift lies in the properties of dispersion characteristics. Our theoretical model, based of the coupled modes approach, is a tool for a flexible design of dispersion and, hence, for tailoring the transmission to the predetermined requirements.

4.1.5 Concluding remarks

We have studied in this Section the transmission properties of two coupled metamaterial lines when one of them is mechanically shifted relative to the other. The agreement between the experimental results and theoretical calculations based on the impedance matrix is good. Moreover, the qualitative model based on the dispersion curves of MI waves in diatomic arrays adequately describes the experimental results. The large ratio achieved, 60 dB between maximum and minimum transmission, makes the effect potentially useful in devices.

4.2 Subwavelength imaging

Ever since Pendry's paper on the perfect lens [2] the idea of near-field imaging has been a driving force in the rapid development of the field of metamaterials as the search for suitable structures capable of near-field imaging continues. A large variety of physical mechanisms was suggested to be responsible for near field imaging, ranging from effective medium theory [76] and excitation of surface plasmon-polariton resonances [77] to imaging based on the curvature of the dispersion characteristics (see e.g. Ref. [78]), phase conjugation [79], or propagation of MI waves [80].

The first imaging experiment with magnetic metamaterials was reported by Wiltshire et al. [16]. Their lens consisted of a single two-dimensional layer of Swiss Rolls. As shown by Zhuromskyy et al. [17], the imaging properties of this lens can be explained by the excitation of MI waves. At the frequencies near the resonance of individual elements, MI waves form standing wave patterns, which, spreading the information about the field source over the whole area of the lens, prevent imaging. In order to avoid excitation of MI waves, one has to choose operating frequencies in stop bands either above or below the resonant frequency. It necessarily results in much weaker signals and, hence, less efficient imaging.

Freire and Marques proposed to use a two-layered structure of split ring resonators for the near-field imaging suggesting that, when the structure consists of two parallel planes of magnetic metamaterial elements, MI waves may play a positive role [80] resulting in growing fields in the inter-layer spacing. Our aim in this Section is to investigate in more detail, both theoretically and experimentally, the imaging mechanism of double-layered magnetic metamaterials.

4.2.1 Tailoring the imaging capabilities

A schematic presentation of the imaging device in its simplest form of two planar arrays parallel to each other (double lens) is shown in Fig. 4.8 a. For a practical realization, see Fig. 4.8 b. The single lens was obtained by omitting one of the layers from the double lens.

The elements are capacitively-loaded split pipes (see Section 3.1). Their resonant frequencies and quality factors are $\omega_0/(2\pi) = (46.2 \pm 0.2)$ MHz and $Q = 105 \pm 5$.

A single line of metamaterial elements is capable of propagating MI waves in the pass band around the resonant frequency (see Section 2.3). The dispersion curve for an isolated planar array is known to be in the form of a backward wave (see Fig. 4.9 a). There are two stop bands where the imaging is possible, one above 50 MHz and the other below 40 MHz. The resonant frequency lies in the pass band of MI waves and, therefore, cannot be used for imaging.

It is desirable, however, to be able to operate at the resonant frequency to have stronger signals, and at the same time suppress the propagation of MI waves at this frequency. The tailoring mechanism with diatomic arrays, which we developed in the previous Chapter, suggests a solution to the problem. As we have seen in Section 3.3, if two planar lines are brought close to each other, their dispersion curves retain the backward character but are split into an upper and lower branch. When the distance between the planar lines is

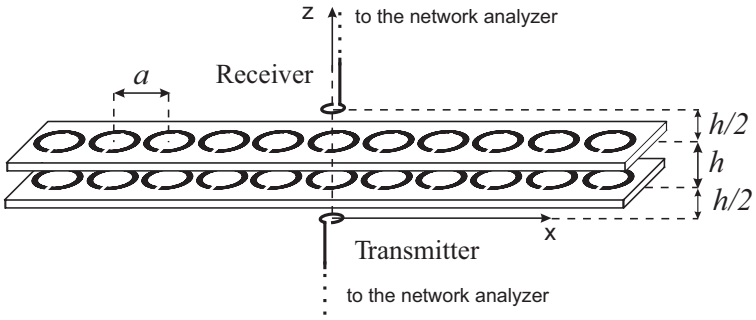

(a)

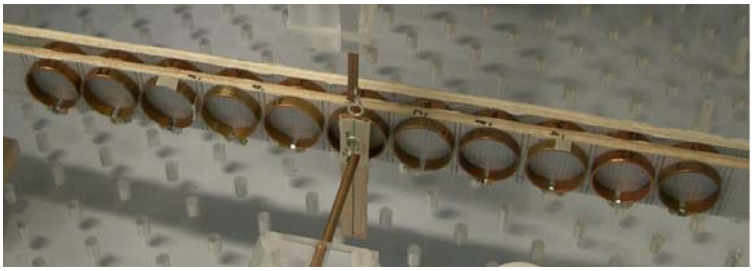

(b)

Figure 4.8: *Schematic presentation of the two-layer magnetoinductive lens* (a) *and photograph of the experimental setup* (b).

sufficiently small then the split may become so large that a stop band appears between the two backward wave regions. Examples for $h = 20$ mm and $h = 10$ mm are shown in Figs. 4.9 b and c. In the latter case, there is a complete bandgap around the resonant frequency which means that MI wave propagation along each one of the lines is suppressed for any value of β. The array with the tailored dispersion characteristics of Figs. 4.9 c is, therefore, a good candidate for effective imaging.

4.2.2 Experiment

To verify the theoretical predictions we performed a series of near field imaging experiments[2]. The spacing between the elements in the same line was $a = 24$ mm. For the single lens, the transmitting circular loop of 3 mm radius was placed at a distance 2.5 mm away from the line, and the magnetic field distribution in the imaging plane 2.5 mm above the line was scanned with the aid of the receiving loop of the same size. The measurements were performed at 1601 frequency points in the range of $30 - 62$ MHz with the aid of a Network Analyzer HP8753ES.

[2]The experiments were carried out at Oxford University by Prof. M. Shamonin (FH Regensburg), Dr. A. Radkovskaya (Moscow University), Mr. R. Trautner (FH Regensburg), Mr. G. Faulkner, Dr. C. J. Stevens and Prof. D. J. Edwards (Oxford University).

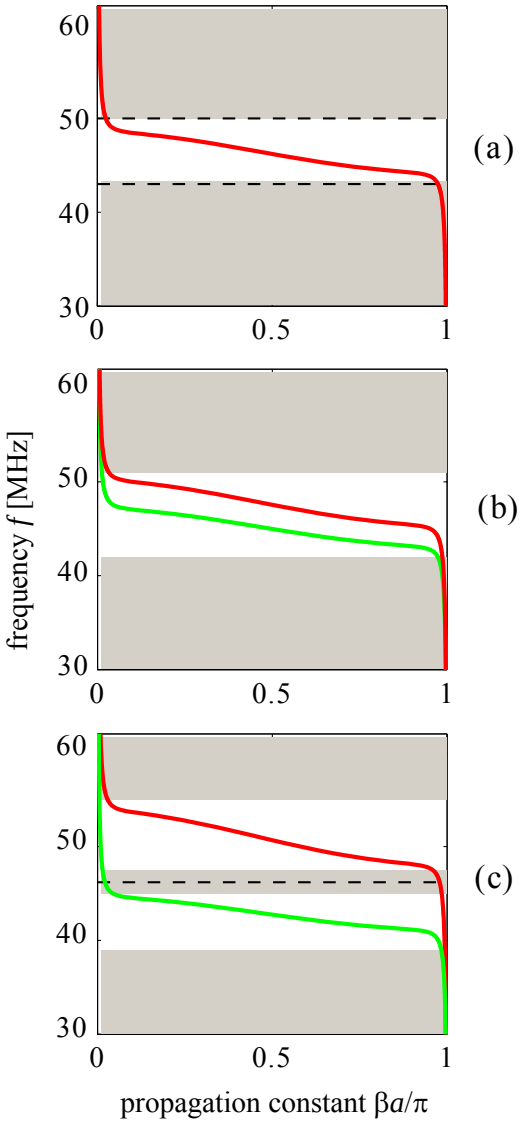

Figure 4.9: *Dispersion characteristics of an isolated line* (a), *two coupled lines separated by* $h = 20$ *mm* (b), *and the same two lines separated by* $h = 10$ *mm* (c). *Stop bands preventing image spreading in the* x*-direction are shown as grey areas. There are two stop bands for the single line* (a). *The separation between the stop bands is larger for two weakly coupled lines* (b). *An additional stop band around the resonant frequency (46.2 MHz) appears for the strongly coupled lines* (c).

For the double lens with the separation h between two lines, the transmitter was placed at a distance $h/2$ below the bottom line, and the receiver scanned the magnetic field at a distance $h/2$ above the top line.

The experimentally obtained image field distribution as a function of frequency is shown for the single lens by the contour plot of Fig. 4.10 a. Figures 4.11 a and 4.12a show the same for the double lens for $h = 20$ mm and $h = 10$ mm. The corresponding theoretical plots are presented in Figs. 4.10 b, 4.11 b and 4.12 b. The theoretical values of magnetic field in the image plane are determined as a superposition of the fields created by the currents in all elements of the setup. The currents are found by inverting the impedance matrix (2.16).

The agreement between theory and experiment is remarkably good. For each configuration, the experimental results reproduce all the details of the theoretical predictions.

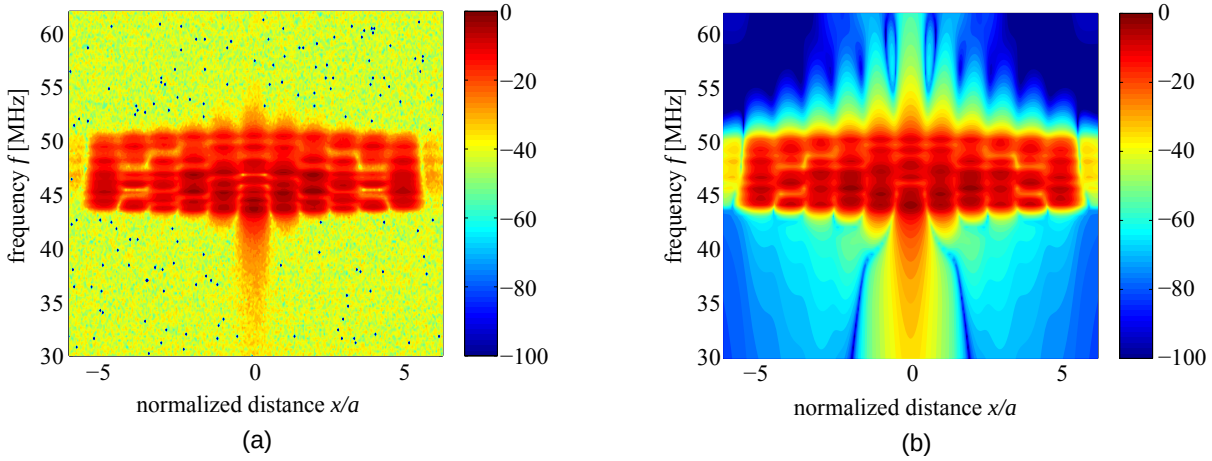

Figure 4.10: *Near field imaging for the single lens. Magnetic field distribution in the image plane versus frequency (contour plot). Experiment* (a) *and theory* (b).

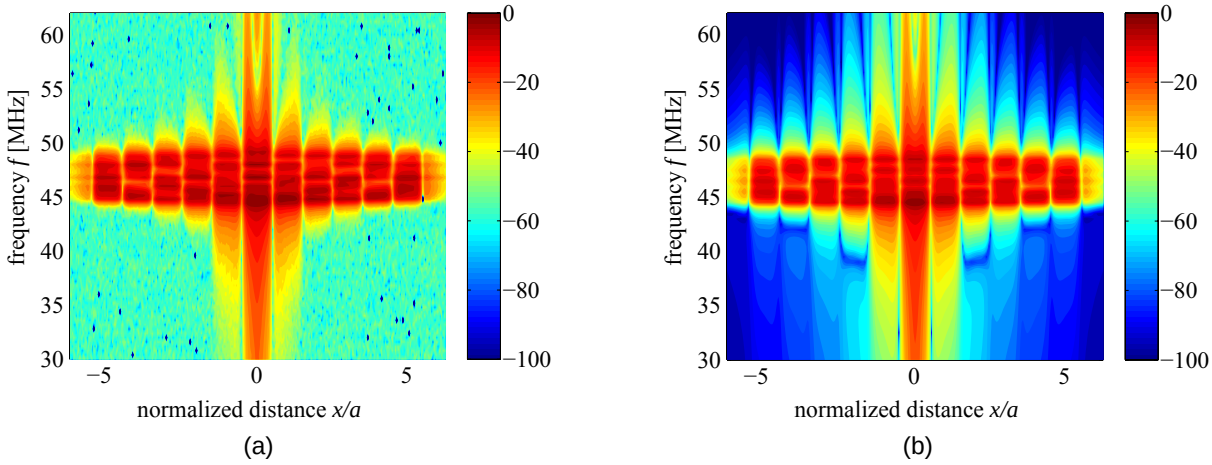

Figure 4.11: *Near field imaging for the double lens with* $h = 20$ *mm. Magnetic field distribution in the image plane versus frequency (contour plot). Experiment* (a) *and theory* (b).

In fact, the only difference between theory and experiment is the signal amplitude in the stop bands. In the experimental plots, they are green indicating the prevailing noise level of about 50 dB, whereas in the theoretical plots the signal level is shown by blue or deep blue indicating significantly lower values, as it should, because noise is not included in the theoretical model.

It may be seen in Figs. 4.10–4.12 that, as mentioned before, MI waves may propagate in the pass bands resulting in high magnetic fields at every element. One observes a broad field distribution corresponding to the excitation of the entire structure. There is a single pass band in Fig. 4.10. In Fig. 4.11, the pass bands may be seen to be overlapping, since

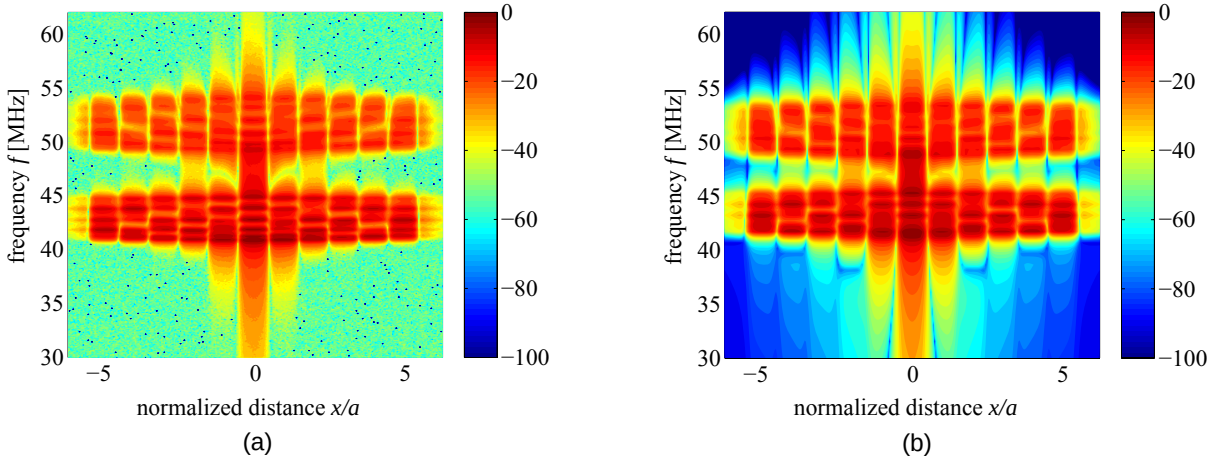

Figure 4.12: *Near field imaging for the double lens with $h = 10$ mm. Magnetic field distribution in the image plane versus frequency (contour plot). Experiment* (a) *and theory* (b).

the lines are only weakly coupled (see Fig. 4.9 b), whereas in Fig. 4.12, the pass bands are clearly separated for the arrangement with strong coupling (see Fig. 4.9 c).

If we wish to have a narrow image then we must use frequencies that are in one of the stop bands. As may be seen in Figs. 4.9 a-c, there are two outer stop bands in Figs. 4.10 and 4.11 and an additional stop band in Fig. 4.12 in the vicinity of the resonant frequency. Since excitation in the outer stop bands is bound to be weak, the signal-to-noise ratio must suffer. Hence the better candidate for successful imaging is the inner stop band.

The comparison between theoretical and experimental results shown in Fig. 4.12 by color coding offers an easily observable global picture. However, if we wish to see the details it is more informative to look at the curves at a single frequency. This is done in Fig. 4.13 where the comparison is for 46.2 MHz. There is excellent agreement between the theoretical (dashed line) and experimental (crosses) results.

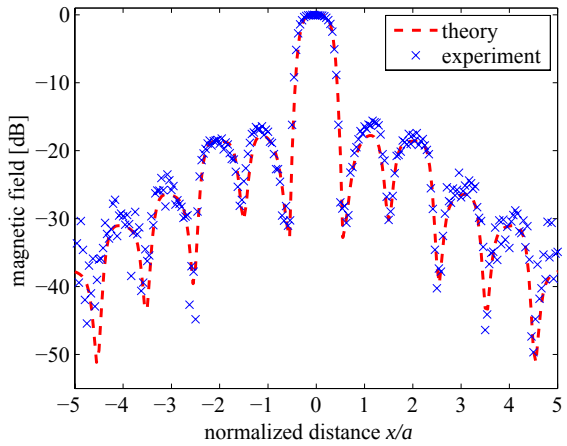

Figure 4.13: *Theoretical (dashed curve) and experimental (crosses) magnetic field distribution in the image plane along the x-axis for the double lens with $h = 10$ mm separation at the resonant frequency (46.2 MHz).*

4.2.3 Comparison between a single lens and a double lens

Our conclusion so far is that the double lens with closely coupled layers is better for imaging than the one with loosely coupled layers, and the reason is the presence of a stop band around the resonant frequency for the former structure. Next, we shall compare the single lens with the double lens. In order to make the comparison meaningful the positions of the transmitter and image plane for both cases remain at the same point, at $z = 0$ and $z = 20$ mm. The two layers of the double lens are at $z = 5$ mm and $z = 15$ mm, and the single lens (obtained by omitting one of the lines from the double lens) is assumed to be at $z = 10$ mm. The basis of the comparison is the distribution of the magnetic field along the x-axis in the image plane.

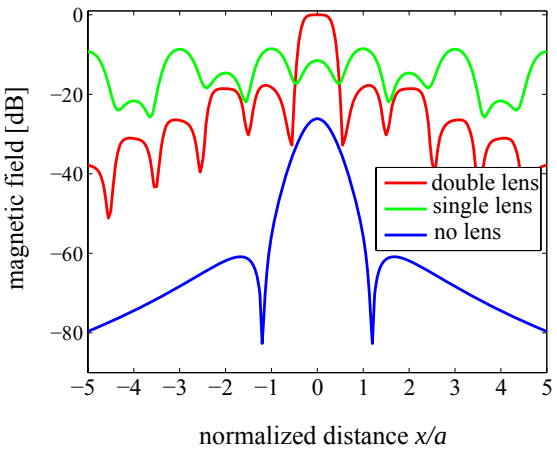

Figure 4.14: *Theoretical magnetic field distributions along the x-axis: double lens (red), single lens (green), in the absence of the lens (cyan). The frequency is 46.2 MHz. The image plane is 20 mm away from the transmitter in each case.*

In Fig. 4.14, three theoretical distributions are plotted at the resonant frequency of 46.2 MHz: in the absence of a lens (i. e. the magnetic field of the transmitter coil), in the presence of a single lens, and in the presence of the double lens. The field is lowest in the absence of the lens. It is just the magnetic field distribution of the current carrying transmitter loop. In the presence of the single lens, the field is higher everywhere but, as may be expected, there is no imaging due to the excitation of MI waves. The ability of the double lens to image may be clearly seen. The amplitude is the highest (normalized to 0 dB at the central peak) and there is no spread of the image. The next peak in the lateral direction is about 20 dB down.

Another comparison is shown in Fig. 4.15; the magnetic field distribution in the image plane is plotted at three different frequencies where imaging occurs: the single lens in the lower stop band at 43 MHz, the single lens in the upper stop band at 50 MHz, and the double lens at the resonant frequency of 46.21 MHz. It may be seen that in the stop bands of the single lens (green and blue curves) the imaging is quite good (the central peak is well distinguished from the secondary peaks) but the field amplitudes are much lower than for the double lens (red curve).

In Fig. 4.16, we show the theoretical distribution of the magnetic field along the z-axis from $z = -10$ mm to $z = 30$ mm for four cases: the double lens at the resonant frequency, single lens at 43 and 50 MHz, and in the absence of a lens. The curves confirm the superior

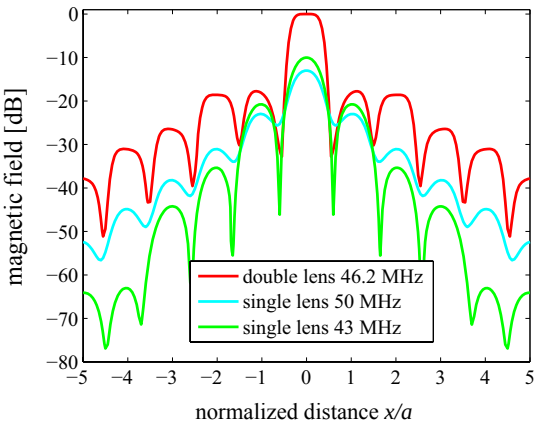

Figure 4.15: *Theoretical magnetic field distributions along the x-axis for the double lens at 46.2 MHz (red) and the single lens at 43 MHz (green) and 50 MHz (cyan). All three figures correspond to the frequencies in the stop bands of MI waves (see Figs. 4.9 a and c, horizontal dashed lines within the stopbands).*

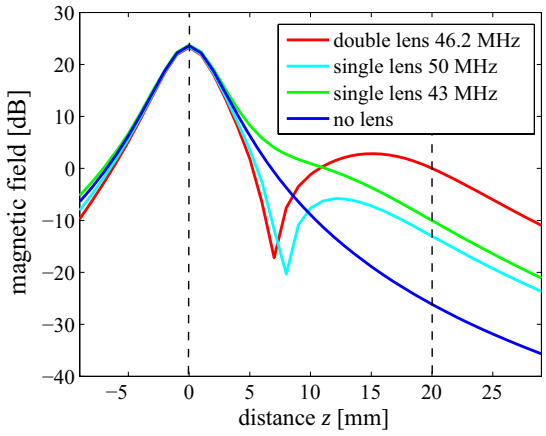

Figure 4.16: *Theoretical magnetic field distributions along the z-axis: double lens at 46.2 MHz (red), single lens at 43 MHz (green) and 50 MHz (cyan), and in the absence of lens (blue). The image plane is 20 mm away from the transmitter in each case, as indicated by the dashed lines.*

performance of the double lens. The amplitude in the image plane is the highest for the double lens, lower for the single lens and the lowest in the absence of the lens both at the output of the lens and at the image plane.

4.2.4 Concluding remarks

In this Section, we have employed the idea of diatomic arrays for tailoring the near-field properties of metamaterials. Our starting point was that strong signals required for good imaging can be achieved at the frequencies near the resonant frequency of the elements. However, in a single lens, excitation of MI waves at these frequencies leads to the spreading of the signal and prevents imaging.

This problem can be solved with diatomic arrays. If the coupling between two planar lines, constituting a double lens, is sufficiently large then two branches of the dispersion characteristics are separated by a stop band centered at the resonant frequency. Consequently, propagation of MI waves in the lateral direction is suppressed, and effective imaging at the resonant frequency is possible. Having developed a theoretical model based on the

coupled-mode approach in the previous Chapter, we have been equipped here with a tool for designing a double-layered lens with the performance superior to the single one.

The resolution of the lens has been shown to be related to element size. Hence, a search for smaller low frequency resonators could lead to further improvement in resolution.

4.3 Subwavelength focusing

Another issue closely related to subwavelength imaging is a possibility to employ metamaterials for subwavelength focusing as well [2]. At optical frequencies, focusing and imaging by classical lenses are strongly related to each other. There is, however, a fine distinction between them when the dimensions are all small relative to the wavelength as pointed out by Freire and Marques [80, 81], whose lens consisted of two planes of magnetically coupled resonant elements. They found, scanning the space behind the lens by a small detector, that the power received was maximum at a particular point. This point is not a focus in the optical sense because the field is not maximum there, but it could be regarded a focus in the sense that the power extracted by the receiver is higher there than that at any other point. The mechanism is matching the receiver to the transmitter [81]. In the experiments of Freire and Marques, the transmitter-lens-receiver positions were those postulated by Pendry [2], namely that the distance from the transmitter to the lens, l, and the distance from the lens to the receiver, f, are both equal to the half of the lens width, h. But is this relationship unique?

Our aim in this Section is to show that, wherever the positions of the transmitter and lens are, a focus can always be placed in an arbitrary position by adjusting the impedance of the receiver. We first provide a general treatment of the problem and then show two examples of how the focus can be tailored.

4.3.1 General formulation

The general model is shown in Fig. 4.17. We have $N + 2$ metamaterial elements, the transmitter, the receiver, and the elements of the lens, which can have arbitrary positions and orientations. The self-impedances of the elements are: Z_{T}, Z_{R} and Z_i $(i = 1 \ldots N)$, where the subscripts T, R and i refer to the transmitter, the receiver, and the elements of the lens. Their respective positions in space are at $(x_{\mathrm{T}}, y_{\mathrm{T}}, z_{\mathrm{T}})$, $(x_{\mathrm{R}}, y_{\mathrm{R}}, z_{\mathrm{R}})$ and (x_i, y_i, z_i). The mutual impedances are characterized by Z_{ij} $(i, j = 1 \ldots N;\ i \neq j)$, the elements of the lens matrix, $Z_{\mathrm{TL}i}$ and $Z_{\mathrm{RL}i}$ $(i = 1 \ldots N)$, the elements of row vectors related to the transmitter and receiver, respectively, and Z_{TR}, a scalar. The elements of the lens are assumed to be lossless. The transmitter and the receiver have impedances of $Z_{\mathrm{T}} = R_{\mathrm{T}} + jX_{\mathrm{T}}$ and $Z_{\mathrm{R}} = R_{\mathrm{R}} + jX_{\mathrm{R}}$, the latter to be determined from the condition that for a voltage V_0 applied to the transmitter, the power absorbed in the receiver should be maximum.

We can write equations for the currents in the elements in the matrix form analogous to Eq. (2.16)

$$\begin{pmatrix} Z_{\mathrm{T}} & \mathbf{Z}_{\mathrm{TL}} & Z_{\mathrm{TR}} \\ \mathbf{Z}_{\mathrm{TL}}^T & \mathbf{Z} & \mathbf{Z}_{\mathrm{RL}}^T \\ Z_{\mathrm{TR}} & \mathbf{Z}_{\mathrm{RL}} & Z_{\mathrm{T}} \end{pmatrix} \begin{pmatrix} I_{\mathrm{T}} \\ \mathbf{I} \\ I_{\mathrm{R}} \end{pmatrix} = \begin{pmatrix} V_0 \\ \mathbf{0} \\ 0 \end{pmatrix} , \tag{4.1}$$

where I_{T} and I_{R} are the currents flowing in the transmitter and receiver, respectively; $\mathbf{I}$ is the N-element column-vector of the currents in the elements of the lens and $\mathbf{0}$ is a column-vector

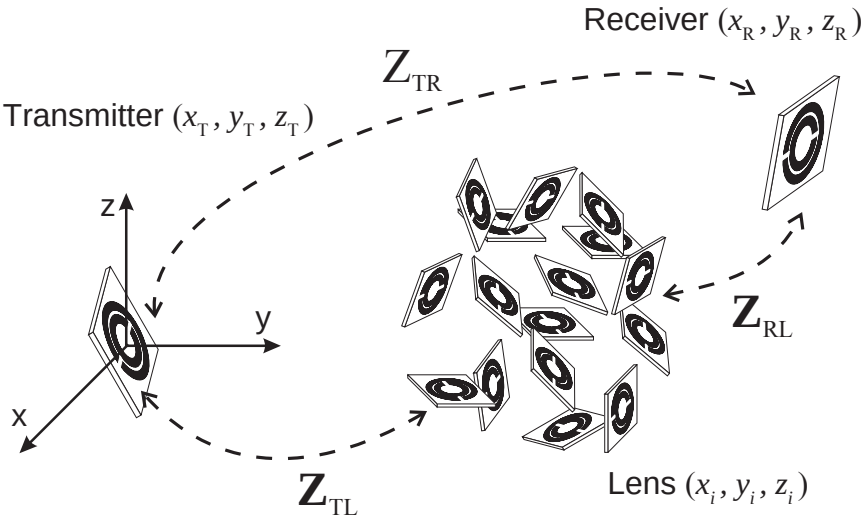

Figure 4.17: *Schematic presentation of the configuration in the general case. The transmitter, receiver, and the elements of the lens are at arbitrary positions and have arbitrary orientations. The coupling between the transmitter and lens is* $\mathbf{Z}_{\mathrm{TL}}$ *and that between the receiver and lens is* $\mathbf{Z}_{\mathrm{RL}}$*. The transmitter and receiver are coupled to each other via the mutual impedance* Z_{TR}*.*

of N zeros. The current in the receiver is, from Eq. (4.1),

$$I_{\mathrm{R}} = -\frac{Z_{\mathrm{TR}} - \mathbf{Z}_{\mathrm{RL}}\mathbf{Z}^{-1}\mathbf{Z}_{\mathrm{TL}}^{T}}{(Z_{\mathrm{R}} - \mathbf{Z}_{\mathrm{RL}}\mathbf{Z}^{-1}\mathbf{Z}_{\mathrm{RL}}^{T})\,(Z_{\mathrm{T}} - \mathbf{Z}_{\mathrm{TL}}\mathbf{Z}^{-1}\mathbf{Z}_{\mathrm{TL}}^{T}) - (Z_{\mathrm{TR}} - \mathbf{Z}_{\mathrm{RL}}\mathbf{Z}^{-1}\mathbf{Z}_{\mathrm{TL}}^{T})^{2}} V_0\,, \tag{4.2}$$

and the current in the transmitter is

$$I_{\mathrm{T}} = -\frac{Z_{\mathrm{R}} - \mathbf{Z}_{\mathrm{RL}}\mathbf{Z}^{-1}\mathbf{Z}_{\mathrm{RL}}^{T}}{(Z_{\mathrm{R}} - \mathbf{Z}_{\mathrm{RL}}\mathbf{Z}^{-1}\mathbf{Z}_{\mathrm{RL}}^{T})\,(Z_{\mathrm{T}} - \mathbf{Z}_{\mathrm{TL}}\mathbf{Z}^{-1}\mathbf{Z}_{\mathrm{TL}}^{T}) - (Z_{\mathrm{TR}} - \mathbf{Z}_{\mathrm{RL}}\mathbf{Z}^{-1}\mathbf{Z}_{\mathrm{TL}}^{T})^{2}} V_0\,. \tag{4.3}$$

The power extracted from the receiver, $P_{\mathrm{R}} = 1/2|I_{\mathrm{R}}|^2 \mathrm{Re}\, Z_{\mathrm{R}}$, depends on its impedance: $P_{\mathrm{R}} = P_{\mathrm{R}}(R_{\mathrm{R}}, X_{\mathrm{R}})$. Since the elements of the lens are lossless, $\mathbf{Z}_{\mathrm{RL}}\mathbf{Z}^{-1}\mathbf{Z}_{\mathrm{RL}}^{T}$, $\mathbf{Z}_{\mathrm{TL}}\mathbf{Z}^{-1}\mathbf{Z}_{\mathrm{TL}}^{T}$, and $\mathbf{Z}_{\mathrm{RL}}\mathbf{Z}^{-1}\mathbf{Z}_{\mathrm{RL}}^{T}$ are purely imaginary. Finding the derivatives of the power in the receiver, $\partial P_{\mathrm{R}}/\partial R_{\mathrm{R}}$ and $\partial P_{\mathrm{R}}/\partial X_{\mathrm{R}}$, and equating them to zero we find the following relationship for the values of the optimum resistance, $R_{\mathrm{R}}^{(\mathrm{opt})}$, and reactance, $X_{\mathrm{R}}^{(\mathrm{opt})}$,

$$Z_1 = \frac{R_3^2}{Z_2^*}\,, \tag{4.4}$$

where

$$\begin{aligned} Z_1 &= Z_{\mathrm{R}}^{(\mathrm{opt})} - \mathbf{Z}_{\mathrm{RL}}\mathbf{Z}^{-1}\mathbf{Z}_{\mathrm{RL}}^{T} \\ Z_2 &= Z_{\mathrm{T}} - \mathbf{Z}_{\mathrm{TL}}\mathbf{Z}^{-1}\mathbf{Z}_{\mathrm{TL}}^{T} \\ R_3^2 &= -\left(Z_{\mathrm{TR}} - \mathbf{Z}_{\mathrm{RL}}\mathbf{Z}^{-1}\mathbf{Z}_{\mathrm{TL}}^{T}\right)^{2} \end{aligned}\,. \tag{4.5}$$

This yields the following optimum value of the receiver impedance

$$R_{\mathrm{R}}^{(\mathrm{opt})} + jX_{\mathrm{R}}^{(\mathrm{opt})} = \\ = \mathbf{Z}_{\mathrm{RL}}\mathbf{Z}^{-1}\mathbf{Z}_{\mathrm{RL}}^{T} - \frac{\left(Z_{\mathrm{TR}} - \mathbf{Z}_{\mathrm{RL}}\mathbf{Z}^{-1}\mathbf{Z}_{\mathrm{TL}}^{T}\right)^2}{R_{\mathrm{T}} - jX_{\mathrm{T}} + \mathbf{Z}_{\mathrm{TL}}\mathbf{Z}^{-1}\mathbf{Z}_{\mathrm{TL}}^{T}}, \tag{4.6}$$

where $\mathbf{Z}^{-1}$ is the inverse of the impedance matrix of the lens and the superscript T means the transposed of a vector.

It follows that in the optimum case, the power extracted from the receiver is equal to that absorbed by the resistive load of the transmitter and has the value

$$P_{\mathrm{R}}^{(\mathrm{max})} = P_{\mathrm{T}}^{(\mathrm{max})} = |V_0|^2/(4R_{\mathrm{T}}). \tag{4.7}$$

Once the optimum load impedance pertaining to the $(x_{\mathrm{R}}, y_{\mathrm{R}}, z_{\mathrm{R}})$ point has been found, it follows that moving the receiver out of that point can only lead to lower extracted power. Hence $(x_{\mathrm{R}}, y_{\mathrm{R}}, z_{\mathrm{R}})$ must be the focal point.

Note that this focal point can be put anywhere in three-dimensional space subject to the condition that all dimensions are small relative to the electromagnetic wavelength. It follows then clearly that the focal width must be subwavelength. The potential application of this new phenomenon is the ability to recognize a predetermined position by the fact that the received power is maximum in that point.

4.3.2 Tailoring the subwavelength focus

We shall now demonstrate the possibility of tailoring the focal point by specifying its position in two examples. For simplicity, we drop the third dimension and assume that all the elements are in the (x, y)-plane.

In our first example, the lens consists of two parallel layers of capacitively loaded loops. Each layer is built up by five elements in a planar arrangement, as can be seen in Fig. 4.18 a. The radius of the elements is $r_0 = 5$ mm and the distance between them in a layer is $d = 2.1r_0 = 10.5$ mm. The separation between the layers is $h = 2r_0 = 10$ mm. The transmitter and receiver are two metallic loops identical to the elements of the lens. The transmitter is placed at the $(0, 0)$ point at a distance l from the lens. We choose the operating frequency to be 500 MHz. The self-inductance of the lens' elements and that of the transmitter, 12.2 nH, is compensated by loading them by 8.3 pF capacitors. The transmitter has an internal resistance of 50 Ohm. The mutual inductances between the transmitter, receiver, and lens can be calculated as shown in Appendix A.

We place then the receiver at three different positions and for each position find the corresponding optimum impedance. Initially, the receiver is placed symmetrically to the transmitter at the distance $f = l$ behind the lens (see Fig. 4.18 a). In this configuration, the separation between the lens layers is twice larger than the distance between the transmitter/receiver and the lens, i. e. obeys the relation used in Refs. [2, 81]. Then the receiver is moved along the y-axis to distances $f = 1.5r_0$, $2r_0$ away from the lens. The values of the optimum impedance corresponding to each position of the lens are given in Table 4.1.

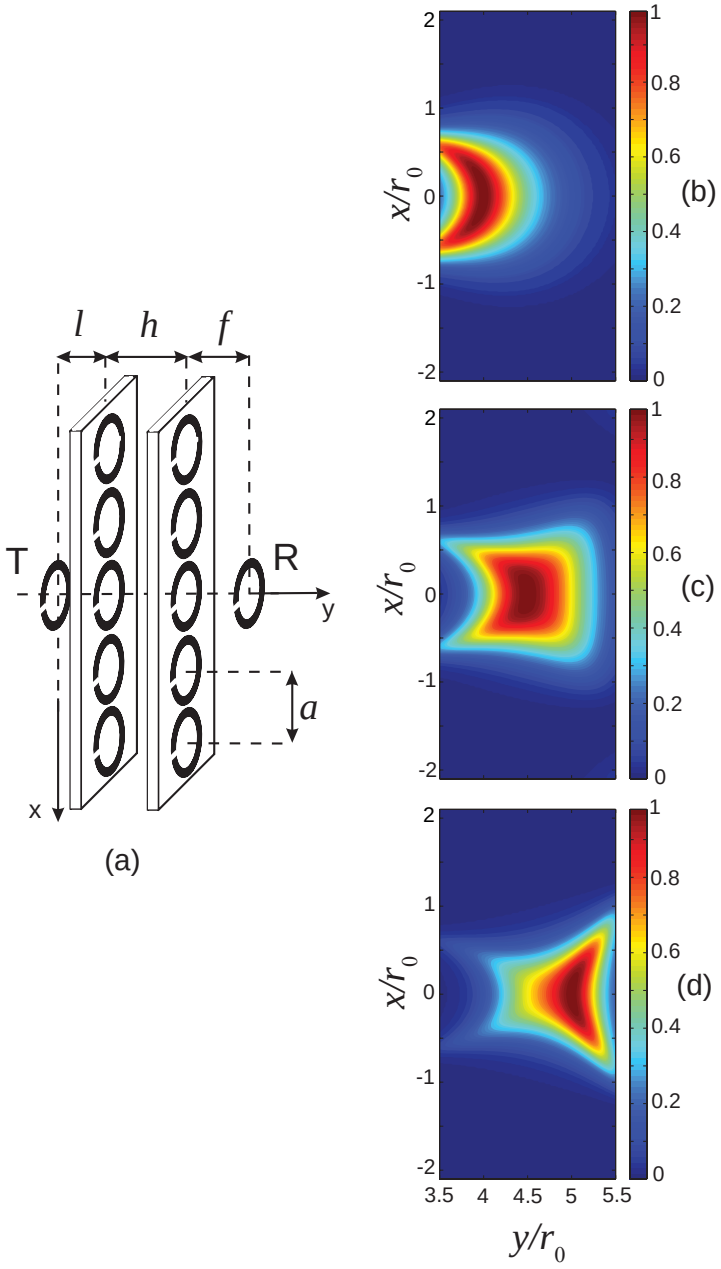

Figure 4.18: (a) *Schematic presentation of the focusing with a two layered lens*, (b)-(d) *contour plots of the normalized extracted power corresponding to three different positions of the receiver,* $f = r_0$, $1.5r_0$, $2r_0$. *Note that only the case* (b) *corresponds to the symmetrical "*$h/2 - h - h/2$*" configuration.*

The results for the extracted power, when the receiver with optimum loading is translated parallel to itself from its initial position, are shown in Figs. 4.18 b-d for all three positions of the receiver. The power is plotted using contour plots relative to the maximum received

distance f/r_0	optimum impedance [Ohm]
1	$0.96 + 0.40j$
1.5	$0.22 - 0.34j$
2	$0.06 - 0.29j$

Table 4.1: Values of the optimum impedance for the configurations of Fig. 4.18 corresponding to three different positions of the receiver, $f = r_0$, $1.5r_0$, $2r_0$.

power of $|V_0|^2/(4R_\mathrm{T})$. It can be clearly seen that focusing of the received power is possible not only for the symmetrical "$h/2 - h - h/2$" configuration but also for the other two. The position of the focus shifts together with the receiver when the latter is moved away from the lens. Moreover, the maximum of the received power is independent of the position of the receiver and has a value of $|V_0|^2/(4R_\mathrm{T})$ for all three cases.

For the second example (Fig. 4.19), we chose quite a different lens configuration. It consists now of two parallel axially arranged arrays with the same element size but of seven elements. The distance between the elements in an array is $a = 0.5r_0 = 2.5$ mm and the separation between the arrays is $h = 2.1r_0$. The arrays are placed symmetrically relative to the y-axis (see Fig. 4.18 a). Similarities to the first example are the choice of resonant frequency at 500 MHz, the purely resistive impedance of the transmitter of 50 Ohm, and the position of the transmitter at the point $(0, 0)$. The distance from the transmitter to the lens is $l = 0.5r_0$. Analogously to the previous example we place the receiver into three different positions on the y-axis, at the distances $f = 0.5r_0$, $1.0r_0$ and $1.5r_0$. The corresponding values of the optimum impedance are given in Table 4.2. The power extracted from the

distance, f/r_0	optimum impedance [Ohm]
0.5	$0.58 - 0.34j$
1.0	$0.21 - 0.05j$
1.5	$0.08 + 0.02j$

Table 4.2: Values of the optimum impedance for the configurations of Fig. 4.18 corresponding to three different positions of the receiver, $f = 0.5r_0$, $1.0r_0$ and $1.5r_0$.

receiving loop as it is moved parallel to itself from its initial optimum position is shown in Figs. 4.19 b-d in the same manner as in Figs. 4.18 b-d in the first example. There are clear maximums for each case corresponding to the different positions of the receiver.

The examples we have given relate to a small number of elements. The aim was merely to show the potential of the method proposed. The numerical techniques, developed for magnetoinductive waves [39, 82], could cope with several thousand elements.

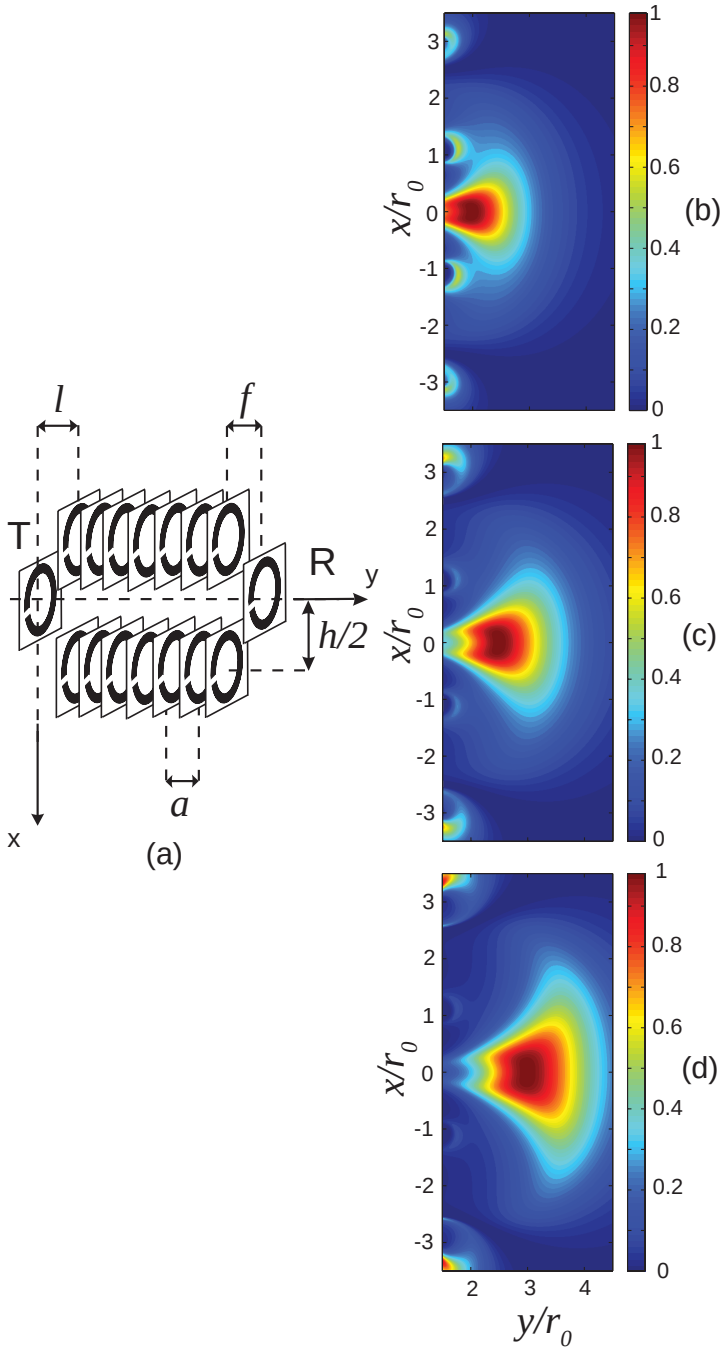

Figure 4.19: (a) *Schematic presentation of the focusing with two parallel axial arrays*, (b)-(d) *contour plots of the normalized extracted power corresponding to three different positions of the receiver,* $f = 0.5r_0$, $1.0r_0$, $1.5r_0$. *Note that only the case* (b) *corresponds to the symmetrical configuration with* $l = f$.

4.3.3 Concluding remarks

In this Section, we have considered the problem of subwavelength focusing by magnetic metamaterials. In contrast to the two previous Sections, where the analytical models were based on the dispersion of diatomic arrays, we relied here completely on the formalism of impedance matrix (2.16) both for analytical and numeric calculations. It gave us a possibility to consider tailoring of the subwavelength focus in the general case when a transmitter, a receiver, and a lens can have arbitrary positions and relative orientations.

We have shown that the power extracted from the receiver may *(i)* reach its maximum and *(ii)* be focused in an arbitrary pre-selected point independently of the actual arrangement of the metamaterial elements provided that the impedance of the receiver is tuned to the optimum value. Applications can be expected in radio-frequency problems where there is need to identify a point in space.

4.4 Rotational Resonance

One of the potential applications of metamaterials is in Magnetic Resonance Imaging, which involves detection of weak signals coming from the human body. It is always desirable to improve the detection mechanisms. In this Section, we shall show how magnetoinductive waves can be profitably used for this purpose.

We suggest a ring resonator consisting of N metamaterial elements arranged into a circular planar array, as shown schematically in Fig. 4.20 [19]. An MI wave propagating along the ring has a (rotational) resonance if the circumference of the ring is equal to an integral multiple of the wavelength. This occurs when $2\pi r = \nu\lambda$, where r is the radius of the ring, ν is an integer, and λ is the wavelength of the MI wave. Hence

$$\beta a = \frac{2\pi\nu}{N}\,, \tag{4.8}$$

and the frequency of the rotational resonance, as found from the dispersion relation (2.12), is

$$\omega_{\rm r} = \frac{\omega_0}{\sqrt{1+\kappa\cos\dfrac{2\pi\nu}{N}}}\,. \tag{4.9}$$

A precessing nuclear magnetic dipole rotating with an angular velocity $\omega_{\rm N}$ is situated in the center of the ring. The dipole induces voltages in each element of the ring, which, in their own turn, excite a traveling MI wave. Under rotational resonance, $\omega_{\rm N}$ is equal to $\omega_{\rm r}$.

4.4.1 Tailoring the power extraction

Let us now discuss the problem of extracting power from a single element. The questions we are asking here are: What is the maximum power that could be extracted in this case, and what are the conditions for the optimum power extraction?

In order to extract power from a single element it should be loaded by a resistive load. If the elements of the ring are uncoupled (and MI waves do not propagate along the ring) then the value of the optimum load resistance is obviously equal to the self-resistance, R, of the element. The maximum power extracted in this case is

$$P = \frac{|V_0|^2}{8R}\,, \tag{4.10}$$

where V_0 is a voltage induced in the element by the dipole's magnetic field. In the case when the elements are coupled to each other and an MI wave travels along the ring, this will no longer be true: the cumulative effect of MI waves can lead to a higher extracted power if the load impedances in the elements of the ring have properly chosen values.

For rotational resonance, we choose to extract power from the first element. It will be loaded by an optimum impedance $Z_{\rm L} = R_{\rm L} + jX_{\rm L}$, the latter to be determined from the conditions that the power extracted is maximum. It is shown analytically in Appendix B

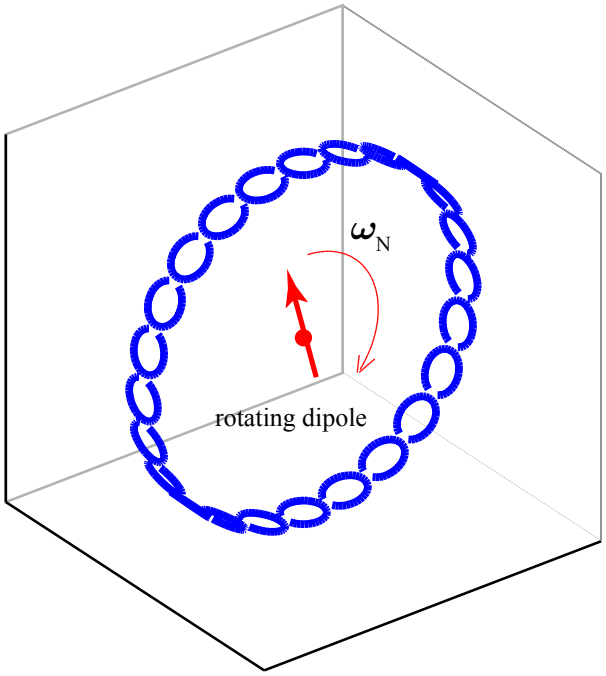

Figure 4.20: *Schematic presentation of a ring resonator. A precessing nuclear magnetic dipole in the center excites a traveling MI wave. Rotational resonance is used to extract power from a single element of the ring.*

for the fundamental resonance, $\nu = 1$, that the optimum load in the low-loss case ($Q \to \infty$) is given by

$$Z_{\mathrm{L}} = \frac{N}{2} R \,. \tag{4.11}$$

The power extracted from the first element is then

$$P = \frac{N|V_0|^2}{16R} \,, \tag{4.12}$$

i. e., $N/2$ larger than in the uncoupled case when there are no MI waves, Eq. (4.10). This analytical result was confirmed by a numerical optimization [19].

Is this the maximum power that could be extracted from the ring resonator? One feels intuitively that violating the symmetry of the current by inserting a load impedance only in the first element is a major perturbation that cannot possibly lead to an absolute maximum. One may argue then that its harmful effect can be mitigated (or even eliminated) by inserting further matching impedances. The right positions here are likely to be the nearest neighbors. It was demonstrated by a numerical optimization in Ref. [19] that inserting additional reactances into elements N and 2 increases the maximum extracted power in the low-loss case to the value

$$P = N \frac{|V_0|^2}{8R} \,, \tag{4.13}$$

which is N times larger than in the uncoupled case, Eq. (4.10), and twice larger than in the case with a load impedance in a single element, Eq. (4.12).

The optimum load impedance in the first element is in this case

$$Z_{\mathrm{L}} = NR\,, \tag{4.14}$$

and, as shown analytically in Appendix B, the tuning impedances in the second and last elements of the ring are

$$Z_{\mathrm{tune\,2,N}} = \pm j \frac{NR}{2\sin\dfrac{4\pi}{N}}\,, \tag{4.15}$$

where the positive value should be taken for the last element and the negative one for the second element.

4.4.2 Concluding remarks

In this Section, we have considered the problem of optimum power extraction from a ring resonator supporting MI waves. For an analytical model, we relied on both the dispersion relation of MI waves and on the impedance-matrix method. We have shown how tailoring the properties of the elements of the ring it is possible to achieve more effective power extraction from a single element in the case when the elements are coupled to each other (with MI waves propagating along the ring) compared to the uncoupled case (without MI waves).

The signal gain described here has a potential in applications for MRI detection systems. We shall return to the problem of rotational resonance in the next Chapter when discussing parametric amplification in ring resonators.

Chapter 5

Nonlinear applications

This Chapter is devoted to nonlinear metamaterials. Out of the diversity of possible effects to consider, we have chosen parametric amplification of MI waves for detailed investigations. Why? As we have said in the Introduction, our aim is to discuss those phenomena that have potential for applications. Amplification in metamaterials is one of them.

One of the factors limiting the behavior of metamaterial devices is losses [83–85]. It is equally true for microwave [20, 21] and optical frequency regions [33, 35, 86], for the effects involving propagation of electromagnetic [82–84] and magnetoinductive [19, 85] waves.

Since we are mostly concerned with the propagation of MI waves, let us briefly discuss the origin of their loss. The attenuation constant, α, for a monatomic metamaterial array, has in the low-loss case [19] the form

$$\alpha = \frac{1}{aQ\kappa \sin \beta a}\,, \tag{5.1}$$

where Q is the quality factor of the elements, κ is the coupling constant between them, a is the period of the array, and β is the propagation constant. It can be seen that in order to decrease attenuation, one has either to increase the quality factor of the individual elements or to increase the coupling between them in the array [85]. In the cases where this is not sufficient (and the loss is still considerable), amplification of the signal could provide a solution for compensating the loss.

Another effect where amplification in metamaterials might be of practical significance is signal detection in MRI. The human body – the source of MRI signals – is at the same time a significant source of noise. Amplification of the signal at an early stage, already in the detection system, could lead to an improvement in the signal-to-noise ratio. We have proposed in Section 4.4 the ring-resonator detection system based on rotational resonance of MI waves and have discussed the improved power extraction achievable with this arrangement. Amplification of MI waves propagating along the ring could bring further benefits in power extraction. Parametric amplification, known for its low-noise properties, is an obvious candidate for investigations.

We shall first present the basics of parametric amplification and discuss how the required nonlinearity can be realized in metamaterials. Then we consider the problem of

phase-matching conditions for MI waves in metamaterial arrays. We shall show that phase matching can be realized by tailoring the dispersion in both monatomic and diatomic configurations. For monatomic arrays, this is achieved by increasing the coupling between the elements (see Chapter 2). For diatomic arrays, we shall rely on the coupled-mode approach developed in Chapter 3.

Having fulfilled phase-matching conditions, we proceed then with theoretical models of parametric amplification of MI waves in monatomic and in diatomic arrays. Finally, we discuss parametric amplification under rotational resonance in arrays arranged into a ring.

5.1 Basics of parametric amplification

Parametric amplification is a nonlinear process involving in the simplest case two waves, a signal and a pump, that are phase matched. Phase-matching conditions in their perfect form imply that both the frequency, ω_p, and the propagation constant, β_p, of the pump wave are twice larger than those of the signal wave, ω_s and β_s, respectively,

$$\omega_\mathrm{p} = 2\omega_\mathrm{s}, \quad \beta_\mathrm{p} = 2\beta_\mathrm{s}\,. \tag{5.2}$$

Interacting in a nonlinear medium, the pump and signal waves can exchange energy; in the case of amplification the energy is transferred from the pump to the signal.

Parametric amplification has been demonstrated for a number of waves of different nature. In optics, amplification of light waves can be observed in crystals with quadratic nonlinearity of the electric permittivity [87, 88]. Parametric amplification of space-charge waves is possible in electron beams, that of acoustic waves in piezoelectrics, and that of magnetostatic waves, in nonlinear ferrites [89–92].

Nowadays, a conventional way of realizing parametric circuits in electronics is to use the nonlinear properties of semiconductor devices, for example, varactor diodes. The capacitance of a varactor diode is voltage dependent, and for small signals it can be written as

$$C^{(\mathrm{nl})} = C_0(1 + \gamma U)\,. \tag{5.3}$$

It is, therefore, reasonable to assume this kind of nonlinearity also for metamaterial elements.

Theoretical studies of parametric amplification in metamaterials have been up to now inspired by the need for loss compensation [14,93,94]. Experimentally, parametric amplification has been demonstrated in backward-wave transmission lines [95], which have similarities to waves propagating in metamaterials [20, 21]. A counterpart of parametric amplification, second-harmonic generation by metamaterials, has been recently reported in Ref. [96].

5.2 Fulfilling phase-matching conditions

The first problem we need to consider is fulfilling phase-matching conditions for parametric amplification of MI waves, Eq. (5.2). This should be done by designing metamaterial arrays that could support both the signal and the pump wave.

5.2.1 Monatomic arrays

Let us first discuss phase matching in the simpler case of monatomic arrays (see Section 2.3). It is worth recalling here the dispersion relation of MI waves in monatomic arrays

$$j\omega L + \frac{1}{j\omega C} + R + 2j\omega M_1 \cos ka = 0\,. \tag{5.4}$$

Here L, C, and R are the inductance, capacitance, and resistance of the elements, and M_1 is the mutual inductance between nearest neighbors.

Let us for further numerical calculations define the parameters of the array. We take $L = 50$ nH and $C = 100$ pF, resulting in the resonant frequency $\omega_0/(2\pi) = 71.17$ MHz. For the mutual inductance, we choose $M_1 = 0.15L$ giving the coupling constant $\kappa_1 = 2M_1/L = 0.3$, a typical value reported, for example, in Refs. [39, 97, 98].

For the value of the signal wave frequency, we take $\omega_\mathrm{s}/(2\pi) = 63.87$ MHz. Neglecting losses, the corresponding propagation constant, as found from the dispersion equation (5.4), is $\beta_\mathrm{s} = 0.20\pi/a$. Phase-matching conditions (5.2) require a pump wave with the twice larger frequency, $\omega_\mathrm{p}/(2\pi) = 127.74$ MHz, and the twice larger propagation constant, $\beta_\mathrm{p} = 0.40\pi/a$. This pair of values, $(\omega_\mathrm{p}, \beta_\mathrm{p})$, does not, however, satisfy the dispersion relation (5.4) as can be seen in Fig. 5.1 a: the corresponding point in the dispersion diagram lies in a stop band of MI waves. The passband is too narrow to support simultaneously both the pump and the signal waves, and therefore the phase-matching conditions cannot be fulfilled.

We need a wider pass band; this can be achieved by increasing the coupling strength between the elements. Let us estimate how strong the coupling strength should be in order to have a sufficiently wide pass band. The width of the pass band is given by Eq. (2.14). Substituting the frequency of the signal for the lower edge of the pass band and a twice larger frequency of the pump for the upper one we obtain for the coupling constant, κ_1,

$$\sqrt{\frac{1+|\kappa_1|}{1-|\kappa_1|}} > 2 \tag{5.5}$$

or $|\kappa_1| > 0.6$. The theoretical limit for the coupling coefficient is 2; obtaining that large values experimentally was, however, a challenge for metamaterial engineering. Only recently, practical realizations with sufficiently large values of κ (up to 1.6) have been reported [54,85]. This was achieved by putting the individual elements maximally close to each other in the axial configuration.

Being certain that it is experimentally feasible to satisfy the requirement for the coupling constant, we can proceed with tailoring the dispersion properties of the array. The only free

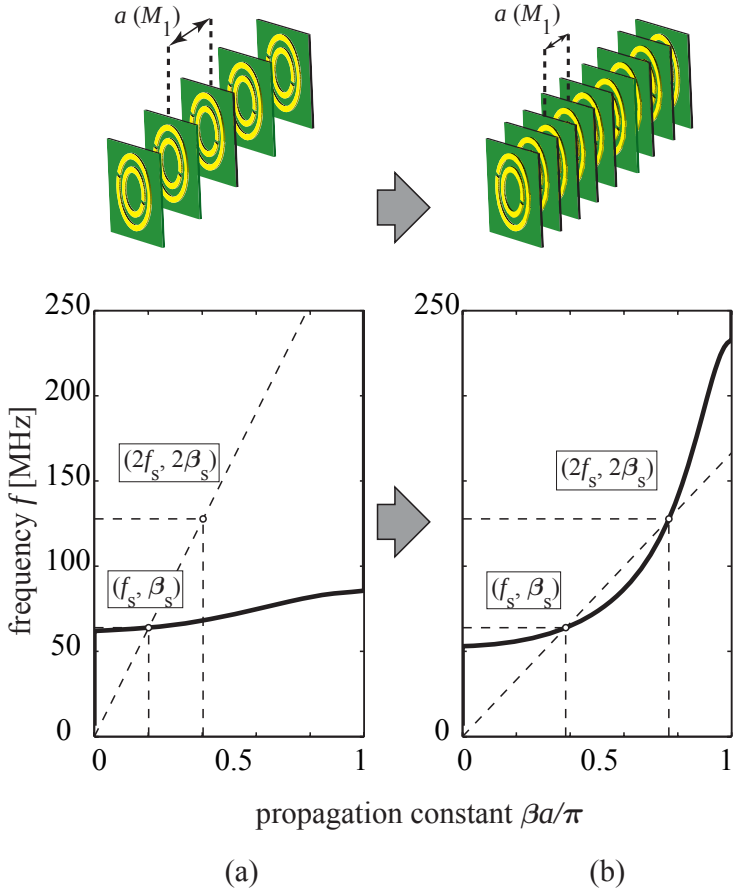

Figure 5.1: *Phase-matching conditions cannot be fulfilled in the case where the coupling between the elements is too weak* (a). *Phase-matching conditions are fulfilled for the case with the large coupling* (b).

parameter left is the resonant frequency of the elements, ω_0. Let us show that for a given coupling constant, by selecting an appropriate resonant frequency, it is possible to design a metamaterial array that would allow propagation of both the signal and the pump MI waves as well as satisfy phase-matching conditions for them. Disregarding losses we can write a system of equations for the signal and the pump assuming that they both satisfy the dispersion relation (5.4)

$$\begin{cases} j\omega_{\mathrm{s}}L + \dfrac{1}{j\omega_{\mathrm{s}}C} + 2jM_1\omega_{\mathrm{s}}\cos\beta_{\mathrm{s}}a = 0 \\ \\ 2j\omega_{\mathrm{s}}L + \dfrac{1}{2j\omega_{\mathrm{s}}C} + 4M_1\omega_{\mathrm{s}}\cos 2\beta_{\mathrm{s}}a = 0 \end{cases} . \tag{5.6}$$

Choosing the mutual inductance to be now $M_1 = 0.45L$ ($\kappa_1 = 0.9$) we can solve Eq. (5.6) for the resonant frequency and propagation constant, giving, respectively, $\omega_0/(2\pi) = 73.44$ MHz

and $\beta_s = 0.38\pi/a$. For the elements with inductance $L = 50$ nH, this value of the resonant frequency can be achieved by loading the elements by capacitances of $C = 94$ pF.

The corresponding dispersion curve is shown in Fig. 5.1 b. It can be seen that, in contrast to the case of the weak coupling of Fig. 5.1 a, both the signal and the pump waves can propagate and are phase-matched, and therefore parametric amplification of the signal is possible, provided, of course, that the metamaterial elements have nonlinear character. In other words, we could (by adjusting the resonant frequency of the elements and the coupling between them) tailor the dispersion properties of the MI waves in the single metamaterial array in order to satisfy the requirement of phase matching.

5.2.2 Diatomic arrays

What are the limitations of the design we have developed above? First, the required high values of the coupling coefficient have been experimentally demonstrated only for axially arranged elements [54, 85]. For planar arrangements, the reported values of the coupling coefficient are much more modest and do not usually exceed the value of -0.1 [40, 56, 97, 98]. This means that planar arrays are excluded from possible phase-matched monatomic realizations – an obvious disadvantage when thinking about planar ring configurations for rotational resonance (Section 4.4). Indeed, as can be seen in Fig. 5.2 a, the dispersion characteristics for a planar monatomic array supports only the signal wave, whereas the pump wave is not supported. The parameters chosen for the example of Fig. 5.2 a are: $L = 50$ nH, $C = 180$ pF, and $\kappa_1 = -0.1$. The chosen frequencies of the signal and pump are, as in the previous example, $\omega_s/(2\pi) = 63.87$ MHz and $\omega_p/(2\pi) = 127.74$ MHz.

The second disadvantage of achieving phase matching by increasing the coupling between the elements is that it leads to the increase of the group velocity of MI waves [59] and, hence, to less efficient parametric interaction between the signal and pump waves. Consequently, the length of the array has to be increased, which can be a disadvantage in the presence of loss.

An alternative solution to the phase-matching problem that we suggest here relies on the concept of diatomic metamaterial arrays (see Chapter 3), which we have already successfully employed for tailoring the properties of MI waves in linear applications (see Chapter 4). In order to fulfill phase-matching conditions we are going here to make use of the two different branches of the dispersion characteristics of diatomic arrays (see Section 3.3). If for linear applications we modified mostly the coupling constants between the elements of diatomic arrays, here we shall also change their resonant frequencies.

The results of Section 3.3 suggest that the strongest interaction between the lines constituting a diatomic array (and, hence, between the signal and pump waves) is observed in the configurations, where the lines are exactly above each other (see Fig. 5.2 b) resulting in the maximum mutual inductance between the elements of different lines, M. The corresponding

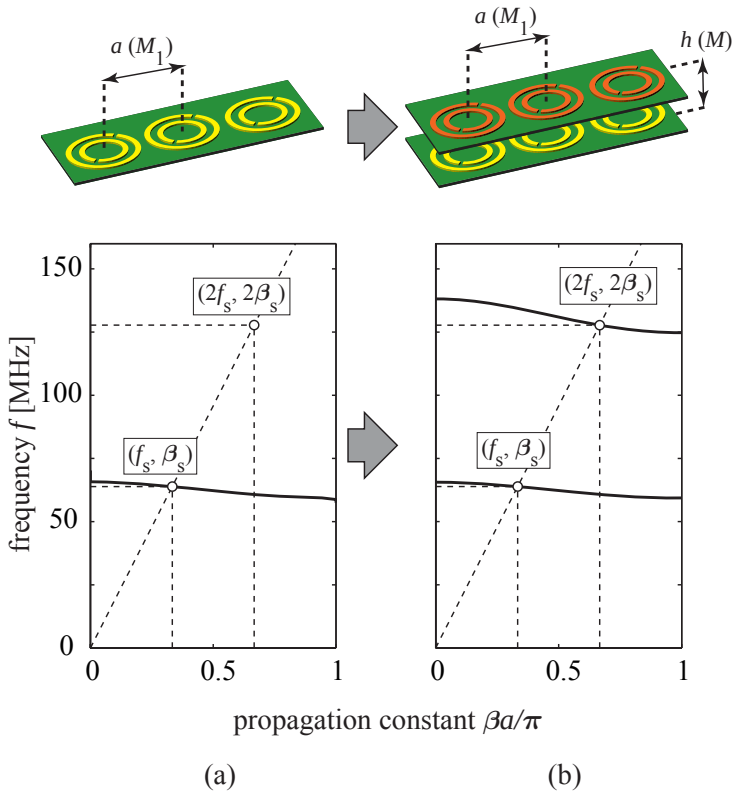

Figure 5.2: *Dispersion characteristic of the monatomic planar metamaterial array* (a) *does not propagate the pump wave. Dispersion characteristic of the diatomic array* (b) *allows propagation of the phase-matched signal and pump waves.*

dispersion relation for MI waves can be written, from Eq. (3.13a), in the form

$$\left(j\omega L + \frac{1}{j\omega C_1} + R_1 + 2j\omega M_1 \cos ka\right) \times \left(j\omega L + \frac{1}{j\omega C_2} + R_2 + 2j\omega M_1 \cos ka\right) = -\omega^2 M^2 \,, \tag{5.7}$$

where we assume for simplicity that the elements of both types have equal self-inductance, L. Different values of the resonant frequencies can be realized by changing the capacitances C_1 and C_2. For further numerical calculations, we take for the mutual inductances the values $M = 0.15L$ and $M_1 = -0.05L$. They are close to the values obtained experimentally in Sections 3.1 and 3.3 for the split-pipe arrays with $h = 10$ mm and $a = 24$ mm. For the self-inductance of the elements and for the signal frequency, we take, analogously to the previous examples, $L = 50$ nH and $\omega_s/(2\pi) = 63.87$ MHz. For the propagation constant, we take the value of $\beta_s = -\pi/(3a)$ well inside the passband, where attenuation is small. The negative value of β_s stands for backward MI waves supported by the planar arrays. Note that here we are in the position to freely choose the value of the propagation constant,

whereas for the monatomic arrays this value is determined by the dispersion relation. It is a consequence of additional freedom in tailoring the dispersion properties provided by diatomic arrays.

Two parameters that are left undefined are the capacitances of the elements, $C_{1,2}$. They are to be determined from the condition that two phase matched waves, the signal, $(\beta_\mathrm{s}, \omega_\mathrm{s})$, and pump, $(\beta_\mathrm{p}, \omega_\mathrm{p})$, satisfy the dispersion relation (5.7). Disregarding losses we can write

$$\begin{cases} \left(j\omega_\mathrm{s}L + \dfrac{1}{j\omega_\mathrm{s}C_1} + 2j\omega_\mathrm{s}M_1\cos\beta_\mathrm{s}a\right)\times \\ \qquad \left(j\omega_\mathrm{s}L + \dfrac{1}{j\omega_\mathrm{s}C_2} + 2j\omega_\mathrm{s}M_1\cos\beta_\mathrm{s}a\right) = -\omega_\mathrm{s}^2M^2 \\ \left(2j\omega_\mathrm{s}L + \dfrac{1}{2j\omega_\mathrm{s}C_1} + 4j\omega_\mathrm{s}M_1\cos 2\beta_\mathrm{s}a\right)\times \\ \qquad \left(2j\omega_\mathrm{s}L + \dfrac{1}{2j\omega_\mathrm{s}C_2} + 4j\omega_\mathrm{s}M_1\cos 2\beta_\mathrm{s}a\right) = -4\omega_\mathrm{s}^2M^2 \end{cases} . \tag{5.8}$$

Solution of Eq. (5.8) gives $C_1 = 130$ pF and $C_2 = 30$ pF. The corresponding resonant frequencies of the elements are $\omega_{01}/(2\pi) = 62.48$ MHz and $\omega_{02}/(2\pi) = 129.15$ MHz. Two branches of the corresponding dispersion relation, Eq. (5.7), are shown in Fig. 5.2 b. It can be seen that the lower branch supports the signal wave and the upper branch, the pump wave, and that both waves are phase-matched.

5.3 Theoretical formulation of parametric amplification

Having developed the mechanisms for the phase-matching between the signal and the pump wave we proceed with a theoretical formulation of parametric amplification in monatomic and diatomic arrays.

5.3.1 Monatomic arrays

An equivalent circuit of a monatomic metamaterial array with nonlinear capacitance in the form (5.3) is shown in Fig. 5.3.

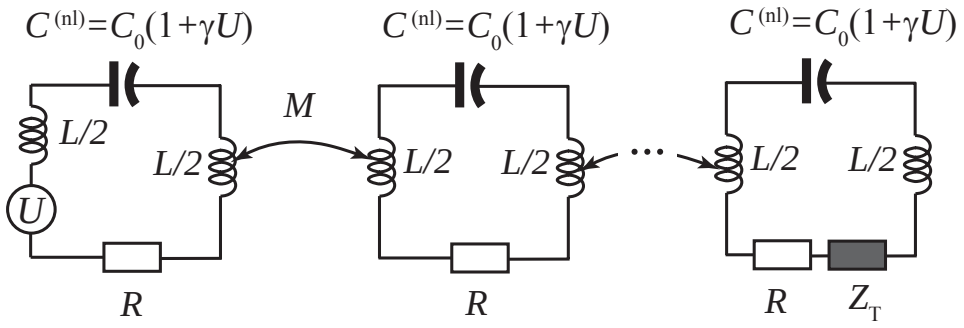

Figure 5.3: *An equivalent circuit of a monatomic metamaterial array. The capacitance is voltage dependent leading to parametric interaction between the signal and the pump.*

Assuming two propagating waves, the signal and the pump, of the form

$$\begin{aligned} U_{\rm s}(n) &= \frac{1}{2}\left[u_{\rm s}(n)e^{j(\omega_{\rm s}t - n\beta_{\rm s}a)} + \text{c.c.}\right] \\ U_{\rm p}(n) &= \frac{1}{2}\left[u_{\rm p}(n)e^{2j(\omega_{\rm s}t - n\beta_{\rm s}a)} + \text{c.c.}\right] \end{aligned} \tag{5.9}$$

(here $U_{\rm s,p}(n)$ are the voltages across the capacitor in the $n^{\rm th}$ element) and neglecting higher harmonics we can write the current, I_n, flowing in the n-th element,

$$I_n = \frac{{\rm d}[C^{(\rm nl)}U]}{{\rm d}t},$$

separately at the signal and pump frequencies. The current at the signal frequency is

$$I_{\rm s}(n) = \frac{j\omega_{\rm s}C_0}{2}\left[u_{\rm s}(n) + \gamma u_{\rm p}(n)u_{\rm s}^*(n)\right]e^{j(\omega_{\rm s}t - n\beta_{\rm s}a)} + \text{c.c.}\,, \tag{5.10}$$

and that at the pump frequency is

$$I_{\rm p}(n) = \frac{j\omega_{\rm s}C_0}{2}\left[2u_{\rm p}(n) + \gamma u_{\rm s}^2(n)\right]e^{2j(\omega_{\rm s}t - n\beta_{\rm s}a)} + \text{c.c.}\,, \tag{5.11}$$

where asterisk denotes complex conjugate.

Kirchhoff's law, Eq. (2.11), for the n^{th} element of the array can be written in the form

$$M\frac{\mathrm{d}}{\mathrm{d}t}\left[I(n+1)+I(n-1)\right]+L\frac{\mathrm{d}I(n)}{\mathrm{d}t}+RI(n)+U(n)=0\,. \tag{5.12}$$

Discrete model

We assume now that the metamaterial array is finite and consists of N elements. The first element is excited by two voltage sources, one at the signal and the other, at the pump frequency. In order to assure traveling wave propagation, the last element should be terminated by the matched loads, whose values at the signal and pump frequencies can be obtained from the simple theory (see Section 2.3) as

$$\begin{aligned} Z_{\mathrm{T}}(\omega_{\mathrm{s}}) &= j\omega_{\mathrm{s}}Me^{-jk_{\mathrm{s}}a} \\ Z_{\mathrm{T}}(2\omega_{\mathrm{s}}) &= 2j\omega_{\mathrm{s}}Me^{-jk_{\mathrm{p}}a} \end{aligned}\,. \tag{5.13}$$

Here $k_{\mathrm{s}}a=\beta_{\mathrm{s}}a-j\alpha_{\mathrm{s}}a$ and $k_{\mathrm{p}}a=2\beta_{\mathrm{s}}a-j\alpha_{\mathrm{p}}a$. Loss is characterized by the attenuation constant of the signal, α_{s}, and the pump, α_{p}, wave.

Substituting expressions for the voltages, Eq. (5.9), and currents, Eqs. (5.10) and (5.11), into Eq. (5.12) we obtain two equations governing the voltages across the nonlinear capacitance in the n^{th} element ($n=2\ldots N-1$). Kirchhoff's equations written separately for the signal, ω_{s}, and pump, $2\omega_{\mathrm{s}}$, frequencies have the form

$$\begin{aligned} &j\omega_{\mathrm{s}}M\Big\{\left[u_{\mathrm{s}}(n+1)+\gamma u_{\mathrm{p}}(n+1)u_{\mathrm{s}}^{*}(n+1)\right]e^{-j\beta_{\mathrm{s}}a}+ \\ &+\left[u_{\mathrm{s}}(n-1)+\gamma u_{\mathrm{p}}(n-1)u_{\mathrm{s}}^{*}(n-1)\right]e^{j\beta_{\mathrm{s}}a}\Big\}+ \\ &+(j\omega_{\mathrm{s}}L+R)\left[u_{\mathrm{s}}(n)+\gamma u_{\mathrm{p}}(n)u_{\mathrm{s}}^{*}(n)\right]-j\frac{1}{\omega_{\mathrm{s}}C_0}u_{\mathrm{s}}(n)=0 \end{aligned} \tag{5.14}$$

and

$$\begin{aligned} &2j\omega_{\mathrm{s}}M\Big\{\left[2u_{\mathrm{p}}(n+1)+\gamma u_{\mathrm{s}}^{2}(n+1)\right]e^{-2j\beta_{\mathrm{s}}a}+ \\ &+\left[2u_{\mathrm{p}}(n-1)+\gamma u_{\mathrm{s}}^{2}(n-1)\right]e^{2j\beta_{\mathrm{s}}a}\Big\}+ \\ &+(2j\omega_{\mathrm{s}}L+R)\left[2u_{\mathrm{p}}(n)+\gamma u_{\mathrm{s}}^{2}(n)\right]-j\frac{1}{\omega_{\mathrm{s}}C_0}u_{\mathrm{p}}(n)=0\,, \end{aligned} \tag{5.15}$$

respectively.

The first, $n=1$, and the last, $n=N$, elements have only a single neighbor. Accordingly, Kirchhoff's equations for them should be modified, additionally taking into account the voltage sources for the first element and the matching impedances for the last element.

The final result can be written in a compact matrix form

$$\begin{cases} \left(\mathbf{Z}^{(\mathrm{s})} - j\frac{1}{\omega_\mathrm{s} C_0}\mathbf{E}\right)\mathbf{u}_\mathrm{s} + \gamma\mathbf{Z}^{(\mathrm{s})}\mathbf{q}_\mathrm{s} = \mathbf{u}_{\mathrm{s}0} \\ \left(\mathbf{Z}^{(\mathrm{p})} - j\frac{1}{2\omega_\mathrm{s} C_0}\mathbf{E}\right)\mathbf{u}_\mathrm{p} + \frac{\gamma}{2}\mathbf{Z}^{(\mathrm{p})}\mathbf{q}_\mathrm{p} = \mathbf{u}_{\mathrm{p}0} \end{cases} . \tag{5.16}$$

Here $\mathbf{E}$ is an $N \times N$ identity matrix,

$$\mathbf{Z}^{(\mathrm{s})} = j\omega_\mathrm{s} \begin{pmatrix} L + \frac{R}{j\omega_\mathrm{s}} & Me^{-j\beta_\mathrm{s} a} & 0 & \dots & 0 \\ Me^{j\beta_\mathrm{s} a} & L + \frac{R}{j\omega_\mathrm{s}} & Me^{-j\beta_\mathrm{s} a} & \dots & \vdots \\ 0 & Me^{j\beta_\mathrm{s} a} & \ddots & \ddots & \vdots \\ \vdots & \ddots & \ddots & \ddots & 0 \\ \vdots & \ddots & \ddots & \ddots & Me^{-j\beta_\mathrm{s} a} \\ 0 & \dots & 0 & Me^{j\beta_\mathrm{s} a} & L + \frac{R + Z_\mathrm{T}(\omega_\mathrm{s})}{j\omega_\mathrm{s}} \end{pmatrix}, \tag{5.17}$$

and

$$\mathbf{Z}^{(\mathrm{p})} = 2j\omega_\mathrm{s} \begin{pmatrix} L + \frac{R}{2j\omega_\mathrm{s}} & Me^{-2j\beta_\mathrm{s} a} & 0 & \dots & 0 \\ Me^{2j\beta_\mathrm{s} a} & L + \frac{R}{2j\omega_\mathrm{s}} & Me^{-2j\beta_\mathrm{s} a} & \dots & \vdots \\ 0 & Me^{2j\beta_\mathrm{s} a} & \ddots & \ddots & \vdots \\ \vdots & \ddots & \ddots & \ddots & 0 \\ \vdots & \ddots & \ddots & \ddots & Me^{-2j\beta_\mathrm{s} a} \\ 0 & \dots & 0 & Me^{2j\beta_\mathrm{s} a} & L + \frac{R + Z_\mathrm{T}(2\omega_\mathrm{s})}{2j\omega_\mathrm{s}} \end{pmatrix}. \tag{5.18}$$

$\mathbf{u}_{\mathrm{s}0} = (u_{\mathrm{s}0}, 0, \dots, 0)^T$ and $\mathbf{u}_{\mathrm{p}0} = (u_{\mathrm{p}0}, 0, \dots, 0)^T$ (the superscript T means transposed of a vector). Here $u_{\mathrm{s}0}$ and $u_{\mathrm{p}0}$ characterize the amplitudes of, respectively, the signal and pump sources in the first element of the array. The vector $\mathbf{q}_\mathrm{s}$ has elements $q_{\mathrm{s}_n} = u_\mathrm{p}(n)u_\mathrm{s}^*(n)$, and the vector $\mathbf{q}_\mathrm{p}$, the elements $q_{\mathrm{p}_n} = u_\mathrm{s}^2(n)$.

Continuous model

Equation (5.16) constitutes a system of difference equations [99] that can be solved numerically for the signal, $u_\mathrm{s}(n)$, and pump, $u_\mathrm{p}(n)$, voltages ($n = 1...N$). For an array of N elements, a system of $2N$ equations should be solved. It is obvious that, although a numerical solution can be found, a general analysis should rely on a more flexible and compact mathematical apparatus. It turns out to be convenient to proceed from the discrete model, based on difference equations (5.16), to a continuous model based on differential equations.

For this purpose, we can expand the amplitudes, $u_{\rm s}$ and $u_{\rm p}$, in the $n^{\rm th}$ element in a Taylor series. Assuming slowly varying amplitudes (a typical approximation based on the assumption of small nonlinearity), we can restrict ourselves to the first two terms of the expansion

$$u_{\rm s,p}(n \pm 1) = u_{\rm s,p}(n) \pm \frac{{\rm d}u_{\rm s,p}}{{\rm d}n}.$$

Here the change of amplitude from element to element is formally written as a derivative. Then

$$u_{\rm s,p}(n+1)e^{-j\beta a} + u_{\rm s,p}(n-1)e^{j\beta a} = 2u_{\rm s,p}(n)\cos\beta a - 2j\frac{{\rm d}u_{\rm s,p}}{{\rm d}n}\sin\beta a\,. \tag{5.19}$$

Note that although we have come from discrete to continuous variables, we did not use the continuous-medium approximation [17], which implies that $\beta a \to 0$. Therefore, it is justified to use Eq. (5.19) everywhere in the Brillouin zone, $-\pi < \beta a < \pi$, including the phase-matching case of Fig. 5.1 b.

Substituting Eq. (5.19) into Eq. (5.16), two differential equations can be obtained. Using the properties of the dispersion relation (5.4) the final result can be written in the form

$$\begin{aligned} \frac{{\rm d}u_{\rm s}(z)}{{\rm d}z} &= -jg_{\rm s}u_{\rm p}(z)u_{\rm s}^*(z) - \alpha_{\rm s}u_{\rm s}(z) \\ \frac{{\rm d}u_{\rm p}(z)}{{\rm d}z} &= -jg_{\rm p}u_{\rm s}^2(z) - \alpha_{\rm p}u_{\rm p}(z) \end{aligned}\,, \tag{5.20}$$

where

$$g_{\rm s} = \frac{\gamma}{2a\omega_{\rm s}^2 C_0 M\sin\beta_{\rm s}a} \qquad \text{and} \qquad g_{\rm p} = \frac{\gamma}{16a\omega_{\rm s}^2 C_0 M\sin 2\beta_{\rm s}a} \tag{5.21}$$

characterize nonlinearity and

$$\alpha_{\rm s} = \frac{R}{2a\omega_{\rm s}M\sin\beta_{\rm s}a} \qquad \text{and} \qquad \alpha_{\rm p} = \frac{R}{4a\omega_{\rm s}M\sin 2\beta_{\rm s}a} \tag{5.22}$$

are in the form of the absorption coefficients of MI waves in the low-loss case [19]. Finally, $z = (n-1)a$ is a continuous coordinate.

As can be expected, in the lossless case, when $\alpha_{\rm s,p} = 0$, Eqs. (5.20) are analogous to the corresponding equations for parametric amplification and second harmonic generation derived in optics [87, 88].

Taking into account that the group velocity of MI waves can be written in the form [59]

$$w_g(\omega) = a\omega^3 C_0 M\sin\beta a\,, \tag{5.23}$$

we can rewrite $g_{\rm s}$ and $g_{\rm p}$ as

$$g_{\rm s} = \frac{\gamma\omega_{\rm s}}{2w_g(\omega_{\rm s})} \qquad \text{and} \qquad g_{\rm p} = \frac{\gamma\omega_{\rm s}}{2w_g(2\omega_{\rm s})}\,. \tag{5.24}$$

Equations (5.20) satisfy conditions for power conservation. It follows directly from Eq. (5.20) that in the lossless case

$$\frac{1}{g_\mathrm{s}}|u_\mathrm{s}|^2 + \frac{1}{g_\mathrm{p}}|u_\mathrm{p}|^2 = \mathrm{const} \tag{5.25}$$

or

$$|u_\mathrm{s}|^2 \sin\beta_\mathrm{s}a + 8|u_\mathrm{p}|^2 \sin 2\beta_\mathrm{s}a = \mathrm{const}\,. \tag{5.26}$$

The power flow, S, at the signal frequency can be written as

$$S(\omega_\mathrm{s}) = \frac{\omega_\mathrm{s}^3 C_0^2}{8a}|u_\mathrm{s}|^2 M \sin\beta_\mathrm{s}a \tag{5.27}$$

and the power flow at the pump frequency, as

$$S(2\omega_\mathrm{s}) = \frac{\omega_\mathrm{s}^3 C_0^2}{a}|u_\mathrm{p}|^2 M \sin 2\beta_\mathrm{s}a\,. \tag{5.28}$$

The total power flow is

$$S(\omega_\mathrm{s}) + S(2\omega_\mathrm{s}) = \frac{\omega^3 C_0^2 M}{8a}\left(|u_\mathrm{s}|^2 \sin\beta_\mathrm{s}a + 8|u_\mathrm{p}|^2 \sin 2\beta_\mathrm{s}a\right)\,. \tag{5.29}$$

This is essentially the same as Eq. (5.26), which was obtained from the differential equations Eq. (5.20); i. e. the continuous model, Eq. (5.20), satisfies the power conservation law.

Effect of loss

In Fig. 5.4 a, the amplitudes of signal and pump voltages across the nonlinear capacitor are shown for a lossless array of 300 elements with the parameters taken from the phase-matching example of Section 5.2 (see Fig. 5.1), and the nonlinearity $\gamma = 0.05\ \mathrm{V}^{-1}$. The first element of the array is excited by two voltage sources, one at the signal frequency with the amplitude 0.05 V and the other one at the pump frequency with the amplitude 0.25 V.

It can be seen from Fig. 5.4 a that the signal and pump waves periodically exchange power; the first maximum of the signal amplitude is achieved at a length of 75 elements. The power is transferred from the pump to the signal during the first half of a period; this is the case of parametric amplification. In the second half of a period the power is transferred from the signal to pump.

As we have already mentioned at the beginning of this Chapter, parametric amplification can be used for the compensation of loss in metamaterials. We shall now look at the effect that loss has on amplification of MI waves. In Fig. 5.4 b, the amplitudes of the signal and the pump waves are shown for the same array with elements having small loss characterized by a quality factor, $Q = \omega_0 L/R$, of 1000. It can be seen that both amplitudes retain their periodic character slowly declining along the array.

If the elements are highly lossy then the amplitude decline is so fast that the pump can no longer effectively transfer its energy to the signal. As can be seen in Fig. 5.4 c for the

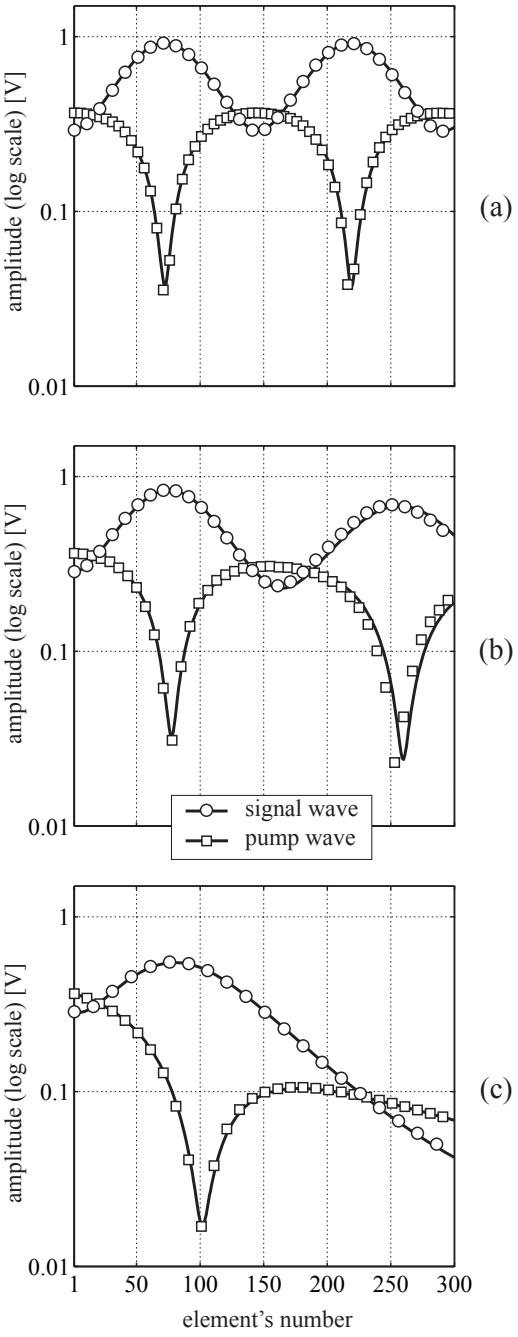

Figure 5.4: *Amplitudes of the signal and pump waves calculated by the discrete (markers) and continuous (solid line) models:* (a) *in the absence of loss,* (b) *for low loss* ($Q = 1000$)*, and* (c) *for high loss* ($Q = 200$)*. Periodic exchange of power in the cases* (a) *and* (b) *disappears for the case of high losses* (c).

elements with $Q = 200$, there is a single pronounced maximum of the signal wave amplitude with no periodic power exchange.

It is gratifying to note that the agreement between solutions of the discrete (markers), Eqs. (5.16), and of the continuous (solid line), Eq. (5.20), models is very good for each case of Figs. 5.4.

Second harmonic generation

The mathematical formulation both in discrete, Eq. (5.16), and continuous, Eq. (5.20), forms is valid not only for the parametric amplification of the signal wave (first harmonic) but also for the generation of the pump wave (second harmonic). In contrast to parametric amplification, which requires nonzero signal in the first element, the initial amplitude of the second harmonic in the case of generation can be zero. An example of second harmonic generation in the absence of loss by the array with the parameters taken from the previous example is shown in Fig. 5.5. The initial amplitude of the second harmonic is zero and that of the first harmonic is $u_{s0} = 0.05$ V. As could be expected from Eq. (5.20), Fig. 5.5 demonstrates the classical behavior of second harmonic generation [87, 88].

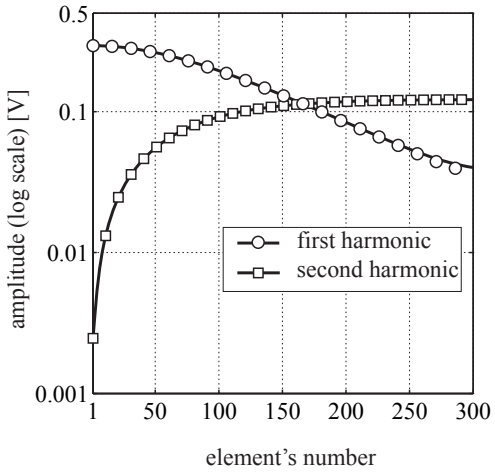

Figure 5.5: *Generation of the second harmonic of an MI wave from a zero initial value.*

5.3.2 Diatomic arrays

The mathematical formulation for parametric amplification in diatomic arrays is obtained following the same steps as in monatomic arrays. Analogously to the monatomic case, we assume here that the required nonlinearity is achieved by the voltage-dependent capacitance given by Eq. (5.3). The corresponding equivalent circuit of a diatomic array consisting of two coupled lines is shown in Fig 5.6. Both lines are made up by N metamaterial elements.

Since we are interested in parametric amplification, it is sufficient to assume a nonlinear capacitance, $C_1^{(\mathrm{nl})} = C_1(1+\gamma U)$, only in the top line, which supports mainly the amplified signal wave. The capacitance of the bottom line, supporting the pump wave, is linear.

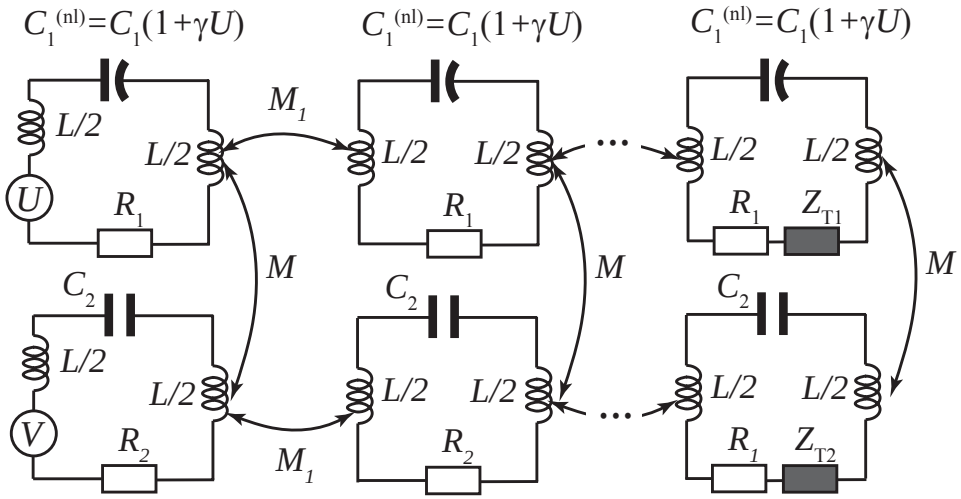

Figure 5.6: *Equivalent circuit of a diatomic metamaterial array. The capacitance of the top line is voltage dependent leading to parametric interaction between the signal and the pump.*

The first element of the top line is excited by the voltage source at the signal frequency, ω_s, and the first element of the bottom line, by the voltage source at the pump frequency, $2\omega_\mathrm{s}$. Each of these sources excites MI waves in the top and bottom lines both at the signal and pump frequencies. Analogously to the monatomic case, it is convenient to write them up in terms of voltages across the capacitances of the n^{th} element ($n = 1 \ldots N$) of both lines

$$\begin{aligned}
U_\mathrm{s}(n) &= \frac{1}{2}\left[u_\mathrm{s}(n)e^{j(\omega_\mathrm{s}t - n\beta_\mathrm{s}a)} + \mathrm{c.c.}\right] \\
U_\mathrm{p}(n) &= \frac{1}{2}\left[u_\mathrm{p}(n)e^{2j(\omega_\mathrm{s}t - n\beta_\mathrm{s}a)} + \mathrm{c.c.}\right] \\
V_\mathrm{s}(n) &= \frac{1}{2}\left[v_\mathrm{s}(n)e^{j(\omega_\mathrm{s}t - n\beta_\mathrm{s}a)} + \mathrm{c.c.}\right] \\
V_\mathrm{p}(n) &= \frac{1}{2}\left[v_\mathrm{p}(n)e^{2j(\omega_\mathrm{s}t - n\beta_\mathrm{s}a)} + \mathrm{c.c.}\right]
\end{aligned} \quad . \tag{5.30}$$

Here $u_\mathrm{s}(n)$ and $u_\mathrm{p}(n)$ are the amplitudes of, respectively, the signal and pump waves in the top line, and $v_\mathrm{s}(n)$ and $v_\mathrm{p}(n)$ are their amplitudes in the bottom line. The corresponding

currents flowing through the elements of the top and bottom lines are, respectively,

$$\begin{aligned} I_n &= \frac{\mathrm{d}[C_1^{(\mathrm{nl})}(U_\mathrm{s}+U_\mathrm{p})]}{\mathrm{d}t} \\ J_n &= C_2\frac{\mathrm{d}[V_\mathrm{s}+V_\mathrm{p}]}{\mathrm{d}t} \end{aligned} \quad . \tag{5.31}$$

Neglecting higher harmonics, the currents can be written separately at the signal and pump frequencies as

$$\begin{aligned} I_\mathrm{s}(n) &= \frac{j\omega_\mathrm{s}C_1}{2}\left[u_\mathrm{s}(n)+\gamma u_\mathrm{p}(n)u_\mathrm{s}^*(n)\right]e^{j(\omega_\mathrm{s}t-n\beta_\mathrm{s}a)}+\mathrm{c.c.} \\ I_\mathrm{p}(n) &= \frac{j\omega_\mathrm{s}C_1}{2}\left[2u_\mathrm{p}(n)+\gamma u_\mathrm{s}^2(n)\right]e^{2j(\omega_\mathrm{s}t-n\beta_\mathrm{s}a)}+\mathrm{c.c.} \\ J_\mathrm{s} &= \frac{j\omega_\mathrm{s}C_2}{2}v_\mathrm{s}(n)e^{j(\omega_\mathrm{s}t-n\beta_\mathrm{s}a)}+\mathrm{c.c.} \\ J_\mathrm{p} &= j\omega_\mathrm{s}C_2v_\mathrm{p}(n)e^{2j(\omega_\mathrm{s}t-n\beta_\mathrm{s}a)}+\mathrm{c.c.} \end{aligned} \quad . \tag{5.32}$$

The last, N^{th}, elements of both lines are terminated by matching impedances (see Fig. 5.6). Since the coupling between the lines is small, the values of the matching impedances can be taken from the simple theory (see Section 2.3). At the signal frequency, both matching impedances are

$$Z_{\mathrm{T}1}(\omega_\mathrm{s}) = Z_{\mathrm{T}2}(\omega_\mathrm{s}) = j\omega_\mathrm{s}M_1e^{-jk_\mathrm{s}a}\,, \tag{5.33}$$

and at the pump frequency they are

$$Z_{\mathrm{T}1}(2\omega_\mathrm{s}) = Z_{\mathrm{T}2}(2\omega_\mathrm{s}) = 2j\omega_\mathrm{s}M_1e^{-jk_\mathrm{p}a}\,. \tag{5.34}$$

For diatomic metamaterial arrays, we shall formulate the theory of parametric amplification following the same steps as has been done for monatomic arrays in Section 5.3.1. First, we shall obtain the system of difference equations governing the amplitudes of the waves across the capacitances and from there we shall derive a set of nonlinear differential equations.

Discrete model

For each element of the top and bottom lines, we can write Kirchhoff's equations governing the voltages across the capacitance at the signal and pump frequencies. For the elements that are not at the ends of the lines ($n = 2 \ldots N-1$), the corresponding equations have the form

- top line, signal frequency

$$
\begin{aligned}
&j\omega_{\rm s}M_1\left\{\left[u_{\rm s}(n+1)+\gamma u_{\rm p}(n+1)u_{\rm s}^*(n+1)\right]e^{-j\beta_{\rm s}a}+\right.\\
&\left.+\left[u_{\rm s}(n-1)+\gamma u_{\rm p}(n-1)u_{\rm s}^*(n-1)\right]e^{j\beta_{\rm s}a}\right\}+\\
&+(j\omega_{\rm s}L+R_1)\left[u_{\rm s}(n)+\gamma u_{\rm p}(n)u_{\rm s}^*(n)\right]+j\omega M\frac{C_2}{C_1}v_{\rm s}(n)-j\frac{1}{\omega_{\rm s}C_1}u_{\rm s}(n)=0\,,
\end{aligned}
\tag{5.35}
$$

- top line, pump frequency

$$
\begin{aligned}
&2j\omega_{\rm s}M_1\left\{\left[2u_{\rm p}(n+1)+\gamma u_{\rm s}^2(n+1)\right]e^{-2j\beta_{\rm s}a}+\right.\\
&\left.+\left[2u_{\rm p}(n-1)+\gamma u_{\rm s}^2(n-1)\right]e^{2j\beta_{\rm s}a}\right\}+\\
&+(2j\omega_{\rm s}L+R_1)\left[2u_{\rm p}(n)+\gamma u_{\rm s}^2(n)\right]+4j\omega M\frac{C_2}{C_1}v_{\rm p}(n)-j\frac{1}{\omega_{\rm s}C_1}u_{\rm p}(n)=0\,,
\end{aligned}
\tag{5.36}
$$

- bottom line, signal frequency

$$
\begin{aligned}
&j\omega_{\rm s}M_1\left\{v_{\rm s}(n+1)e^{-j\beta_{\rm s}a}+v_{\rm s}(n-1)e^{j\beta_{\rm s}a}\right\}+\\
&+(j\omega_{\rm s}L+R_2)v_{\rm s}(n)+j\omega M\frac{C_1}{C_2}\left[u_{\rm s}(n)+\gamma u_{\rm p}(n)u_{\rm s}^*(n)\right]-j\frac{1}{\omega_{\rm s}C_2}v_{\rm s}(n)=0\,,
\end{aligned}
\tag{5.37}
$$

- bottom line, pump frequency

$$
\begin{aligned}
&2j\omega_{\rm s}M_1\left\{u_{\rm p}(n+1)e^{-2j\beta_{\rm s}a}+u_{\rm p}(n-1)e^{2j\beta_{\rm s}a}\right\}+\\
&+(2j\omega_{\rm s}L+R_2)v_{\rm p}(n)+j\omega M\frac{C_1}{C_2}\left[2u_{\rm p}(n)+\gamma u_{\rm s}^2(n)\right]-j\frac{1}{2\omega_{\rm s}C_2}v_{\rm p}(n)=0\,.
\end{aligned}
\tag{5.38}
$$

Equations for the first and the last elements should be modified taking into account the sources and matching impedances in them. The final result can be written in a compact matrix form

$$
\left\{\begin{array}{l}
\left(\mathbf{Z}_1^{(\rm s)}-j\dfrac{1}{\omega_{\rm s}C_1}\mathbf{E}\right)\mathbf{u}_{\rm s}+\gamma\mathbf{Z}_1^{(\rm s)}\mathbf{q}_{\rm s}+j\omega_{\rm s}M\dfrac{C_2}{C_1}\mathbf{v}_{\rm s}=\mathbf{u}_{\rm s0}\\
\left(\mathbf{Z}_1^{(\rm p)}-j\dfrac{1}{2\omega_{\rm s}C_1}\mathbf{E}\right)\mathbf{u}_{\rm p}+\dfrac{\gamma}{2}\mathbf{Z}_1^{(\rm p)}\mathbf{q}_{\rm p}+2j\omega_{\rm s}M\dfrac{C_2}{C_1}\mathbf{v}_{\rm p}=\mathbf{0}\\
\left(\mathbf{Z}_2^{(\rm s)}-j\dfrac{1}{\omega_{\rm s}C_2}\mathbf{E}\right)\mathbf{v}_{\rm s}+j\omega_{\rm s}M\dfrac{C_1}{C_2}(\mathbf{u}_{\rm s}+\gamma\mathbf{q}_{\rm s})=\mathbf{0}\\
\left(\mathbf{Z}_2^{(\rm p)}-j\dfrac{1}{2\omega_{\rm s}C_2}\mathbf{E}\right)\mathbf{v}_{\rm p}+2j\omega_{\rm s}M\dfrac{C_1}{C_2}\left(\mathbf{u}_{\rm p}+\dfrac{\gamma}{2}\mathbf{q}_{\rm p}\right)=\mathbf{v}_{\rm p0}
\end{array}\right.\,.
\tag{5.39}
$$

Here $\mathbf{E}$ is an $N \times N$ identity matrix,

$$\mathbf{Z}_{1,2}^{(\mathrm{s})} = j\omega_\mathrm{s} \begin{pmatrix} L + \dfrac{R_{1,2}}{j\omega_\mathrm{s}} & M_1 e^{-j\beta_\mathrm{s} a} & 0 & \dots & 0 \\ M_1 e^{j\beta_\mathrm{s} a} & L + \dfrac{R_{1,2}}{j\omega_\mathrm{s}} & M_1 e^{-j\beta_\mathrm{s} a} & \dots & \vdots \\ 0 & M_1 e^{j\beta_\mathrm{s} a} & \ddots & \ddots & \vdots \\ \vdots & \ddots & \ddots & \ddots & 0 \\ \vdots & \ddots & \ddots & \ddots & M_1 e^{-j\beta_\mathrm{s} a} \\ 0 & \dots & 0 & M_1 e^{j\beta_\mathrm{s} a} & L + \dfrac{R_{1,2} + Z_{\mathrm{T}1,2}(\omega_\mathrm{s})}{j\omega_\mathrm{s}} \end{pmatrix}, \quad (5.40)$$

and

$$\mathbf{Z}_{1,2}^{(\mathrm{p})} = 2j\omega_\mathrm{s} \times$$

$$\begin{pmatrix} L + \dfrac{R_{1,2}}{2j\omega_\mathrm{s}} & M_1 e^{-2j\beta_\mathrm{s} a} & 0 & \dots & 0 \\ M_1 e^{2j\beta_\mathrm{s} a} & L + \dfrac{R_{1,2}}{2j\omega_\mathrm{s}} & M_1 e^{-2j\beta_\mathrm{s} a} & \dots & \vdots \\ 0 & M_1 e^{2j\beta_\mathrm{s} a} & \ddots & \ddots & \vdots \\ \vdots & \ddots & \ddots & \ddots & 0 \\ \vdots & \ddots & \ddots & \ddots & M_1 e^{-2j\beta_\mathrm{s} a} \\ 0 & \dots & 0 & M_1 e^{2j\beta_\mathrm{s} a} & L + \dfrac{R_{1,2} + Z_{\mathrm{T}1,2}(2\omega_\mathrm{s})}{2j\omega_\mathrm{s}} \end{pmatrix}, \quad (5.41)$$

$\mathbf{u}_{\mathrm{s}0} = (u_{\mathrm{s}0}, 0, \dots, 0)^T$ and $\mathbf{v}_{\mathrm{p}0} = (v_{\mathrm{p}0}, 0, \dots, 0)^T$. $u_{\mathrm{s}0}$ and $u_{\mathrm{p}0}$ characterize the amplitudes of, respectively, the signal and pump sources in the first elements of the top and bottom lines. The vector $\mathbf{q}_\mathrm{s}$ has elements $q_{\mathrm{s}_n} = u_\mathrm{p}(n) u_\mathrm{s}^*(n)$, and the vector $\mathbf{q}_\mathrm{p}$, the elements $q_{\mathrm{p}_n} = u_\mathrm{s}^2(n)$. Numerical calculations show that Eqs. (5.39) conserve power to a high degree of accuracy.

Continuous model

Equations (5.39) constitute a system of $4N$ nonlinear difference equations for $4N$ signal and pump amplitudes in each element of the arrays and can be solved numerically. Direct analysis of Eq. (5.39) would be obviously even more complicated than in the monatomic case. In Section 5.3.1, we have obtained a continuous formulation by using expansion into Taylor series for the amplitudes. Here we can rely on the same approach. Substituting

Eq. (5.19) into Eq. (5.39) the following four differential equations can be obtained

$$\begin{aligned}
\frac{\mathrm{d}u_{\mathrm{s}}(z)}{\mathrm{d}z} &= -jg_u u_{\mathrm{p}}(z)u_{\mathrm{s}}^*(z) + j\mu_{uu}u_{\mathrm{s}}(z) - j\mu_{uv}v_{\mathrm{s}}(z) - \alpha_{\mathrm{s}}u_{\mathrm{s}}(z) \\
\frac{\mathrm{d}v_{\mathrm{s}}(z)}{\mathrm{d}z} &= -jg_v u_{\mathrm{p}}(z)u_{\mathrm{s}}^*(z) + j\mu_{vv}v_{\mathrm{s}}(z) - j\mu_{vu}u_{\mathrm{s}}(z) - \alpha_{\mathrm{s}}v_{\mathrm{s}}(z) \\
\frac{\mathrm{d}u_{\mathrm{p}}(z)}{\mathrm{d}z} &= -jf_u u_{\mathrm{s}}^2(z) - j\eta_{uu}u_{\mathrm{p}}(z) - j\eta_{uv}v_{\mathrm{p}}(z) - \alpha_{\mathrm{p}}u_{\mathrm{p}}(z) \\
\frac{\mathrm{d}v_{\mathrm{p}}(z)}{\mathrm{d}z} &= -jf_v u_{\mathrm{s}}^2(z) - j\eta_{vv}v_{\mathrm{p}}(z) - j\eta_{vu}u_{\mathrm{p}}(z) - \alpha_{\mathrm{p}}v_{\mathrm{p}}(z)
\end{aligned} \quad . \tag{5.42}$$

Equations (5.42) are clearly of the form of coupled-wave equations, where the coefficients

$$\begin{aligned}
g_u &= \frac{\gamma}{2a\omega_{\mathrm{s}}^2 C_1 M_1 \sin\beta_{\mathrm{s}}a} \qquad g_v = \frac{\gamma M}{2C_2 M_1 \sin\beta_{\mathrm{s}}a} \\
f_u &= \frac{\gamma}{16a\omega_{\mathrm{s}}^2 C_2 M_1 \sin 2\beta_{\mathrm{s}}a} \qquad f_v = \frac{\gamma C_1 M}{4aC_2 M_1 \sin 2\beta_{\mathrm{s}}a}
\end{aligned} \tag{5.43}$$

are responsible for the nonlinear coupling between the signal and pump, and

$$\begin{aligned}
\mu_{uu} &= \frac{\omega_{\mathrm{s}}^2 M^2 C_1 C_2}{2a(C_1 - C_2)M_1 \sin\beta_{\mathrm{s}}a} \qquad \mu_{uv} = \frac{C_2 M}{2aC_1 M_1 \sin\beta_{\mathrm{s}}a} \\
\mu_{vv} &= \frac{C_1 - C_2}{2a\omega_{\mathrm{s}}^2 C_1 C_2 M_1 \sin\beta_{\mathrm{s}}a} \qquad \mu_{vu} = \frac{C_1 M}{2aC_2 M_1 \sin\beta_{\mathrm{s}}a} \\
\eta_{uu} &= \frac{C_1 - C_2}{8a\omega_{\mathrm{s}}^2 C_1 C_2 M_1 \sin 2\beta_{\mathrm{s}}a} \qquad \eta_{uv} = \frac{C_2 M}{2aC_1 M_1 \sin 2\beta_{\mathrm{s}}a} \\
\eta_{vv} &= \frac{2\omega_{\mathrm{s}}^2 M^2 C_1 C_2}{a(C_1 - C_2)M_1 \sin 2\beta_{\mathrm{s}}a} \qquad \eta_{vu} = \frac{C_1 M}{2aC_2 M_1 \sin 2\beta_{\mathrm{s}}a}
\end{aligned} \tag{5.44}$$

characterize the linear coupling between the waves of the same frequency that propagate in the top and bottom lines.

Finally, the attenuation coefficients, $\alpha_{\mathrm{s,p}}$, are

$$\begin{aligned}
\alpha_{\mathrm{s}} &= \frac{R_1}{2a\omega_{\mathrm{s}} M_1 \sin\beta_{\mathrm{s}}a}\,, \\
\alpha_{\mathrm{p}} &= \frac{R_2}{4a\omega_{\mathrm{s}} M_1 \sin 2\beta_{\mathrm{s}}a}\,.
\end{aligned} \tag{5.45}$$

Further simplification comes from the properties of the dispersion relation (5.8). Since the resonant frequencies of the elements of the top and bottom lines are different, the

coupling between the lines is small, and the corresponding dispersion equation differs little from the noncoupled case, Eq. (5.4). Therefore, we can assume that

$$j\omega_{\mathrm{s}}L + \frac{1}{j\omega_{\mathrm{s}}C_1} + 2j\omega_{\mathrm{s}}M_1 \cos\beta_{\mathrm{s}}a \approx 0 \tag{5.46}$$

and

$$2j\omega_{\mathrm{s}}L + \frac{1}{2j\omega_{\mathrm{s}}C_1} + 4j\omega_{\mathrm{s}}M_1 \cos 2\beta_{\mathrm{s}}a \approx 0\,. \tag{5.47}$$

Next, we can take into account that due to the resonant behavior of the elements of the bottom line, supporting mainly the pump wave, the amplitude of the signal wave in the bottom line, v_{s}, is small. We can then neglect its nonlinear character and find directly from the signal amplitude, u_{s}, using the linear relationship

$$v_{\mathrm{s}} = -\frac{j\omega L + \dfrac{1}{j\omega C_1} + R_1 + 2j\omega M_1 \cos k_{\mathrm{s}}a}{j\omega M}\frac{C_1}{C_2}u_{\mathrm{s}} \tag{5.48}$$

or, taking Eq. (5.47) into account,

$$v_{\mathrm{s}} = \frac{\omega_{\mathrm{s}}^2 C_1^2 M}{C_1 - C_2}u_{\mathrm{s}}\,. \tag{5.49}$$

This reduces the total number of differential equations to three

$$\begin{aligned}
\frac{\mathrm{d}u_{\mathrm{s}}(z)}{\mathrm{d}z} &= -jg_u u_{\mathrm{p}}(z)u_{\mathrm{s}}^*(z) - \alpha_{\mathrm{s}}u_{\mathrm{s}}(z) \\
\frac{\mathrm{d}u_{\mathrm{p}}(z)}{\mathrm{d}z} &= -jf_u u_{\mathrm{s}}^2(z) - j\eta_{uu}u_{\mathrm{p}}(z) - j\eta_{uv}v_{\mathrm{p}}(z) - \alpha_{\mathrm{p}}u_{\mathrm{p}}(z) \\
\frac{\mathrm{d}v_{\mathrm{p}}(z)}{\mathrm{d}z} &= -jf_v u_{\mathrm{s}}^2(z) - j\eta_{vv}v_{\mathrm{p}}(z) - j\eta_{vu}u_{\mathrm{p}}(z) - \alpha_{\mathrm{p}}v_{\mathrm{p}}(z)
\end{aligned} \quad . \tag{5.50}$$

Let us now give a few numerical examples. For the parameters of the array, we choose the values that we have obtained in Section 5.2.2 for fulfilling phase-matching conditions. The free parameters, still left undefined, are the nonlinearity of the capacitance, γ, the resistances of the elements, $R_{1,2}$, and the initial amplitudes of the signal and pump (defined by the voltage sources in the first elements, U_0 and V_0). We choose the value of γ to be 0.1 V^{-1}. The resistances of the elements shall be characterized by the quality factor, Q, assumed to be equal for both the top and bottom lines.

The amplitudes of the signal and pump waves in both lines corresponding to the parameters of the case (1) of Table 5.1 are shown in Figs. 5.7 a and b. The solutions by the continuous model, Eq. (5.50), are shown by solid line and the solutions by the discrete model, Eq. (5.39), by markers (circles for the signal and squares for the pump). The initial amplitudes of the signal and pump waves in the top line, which contains nonlinear elements,

	quality factor, Q	amplitude of the signal source, U_0	amplitude of the pump source, V_0
(1)	∞	10 mV	125 mV
(2)	∞	0.5 mV	50 mV
(3)	5000	10 mV	125 mV
(4)	1000		
(5)	500		
(6)	400		
(7)	250		
(8)	150		
(9)	100	250 μV	1
(10)	500	1 μV	50 mV

Table 5.1: Quality factors of the elements and values of the signal and pump voltage sources.

have comparable values. As could be expected in this case, the amplitudes behave similarly to the general case of interaction known in optics [87, 88] (compare with Fig. 5.4 a). Propagating along the array they periodically exchange power, and a full period is shown in Fig. 5.7. The signal is amplified in the first half of the period; its maximum is reached at the distance of 25 elements. The signal is strong in the top line and weak in the bottom one; the pump is opposite.

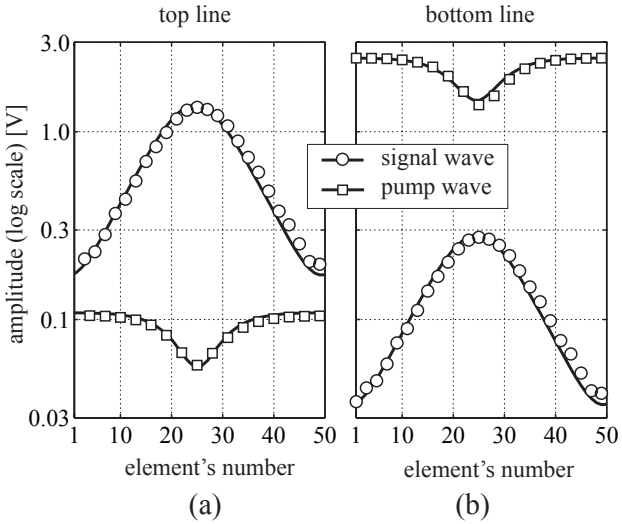

Figure 5.7: *Periodic exchange of power between the signal and pump in the general case, top* (a) *and bottom* (b) *lines. Solutions by the discrete (circles and squares) and continuous (solid line) models for the case* (1) *of Table 5.1.*

The amplitudes of the signal and pump in the case (2) of Table 5.1 are shown in Fig. 5.8.

In this case, the pump is initially much stronger than the signal, and its amplitude remains the same along the array. Equation (5.50) simplifies then to

$$\frac{du_{\rm s}(z)}{dz} = -jg_{\rm s}u_{\rm p}u_{\rm s}^*(z)\,, \tag{5.51}$$

where $u_{\rm p}$ is now constant. This is the well-known case of undepleted pump [87, 88]. The nonlinear parameter, $g_{\rm s}$, is of the form

$$g_{\rm s} = \frac{\gamma}{2a\omega_{\rm s}^2 C_1 M_1 \sin\beta_{\rm s}a} = \frac{\gamma\omega_{\rm s}}{2w_g}\,, \tag{5.52}$$

where $w_g = a\omega_{\rm s}^3 C_1 M_1 \sin\beta_{\rm s}a$ is the group velocity of MI waves at the signal frequency.

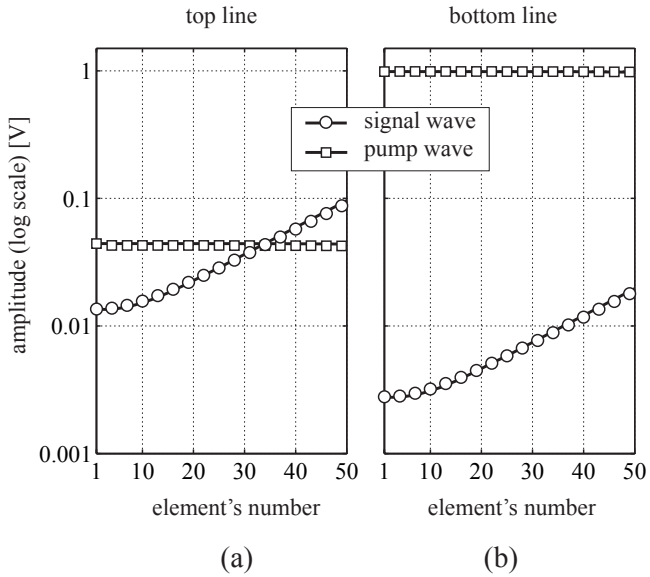

Figure 5.8: *Parametric amplification in the undepleted-pump approximation (case* (2) *of Table 5.1). Amplitudes of the waves in the top* (a) *and bottom* (b) *lines.*

Effect of loss

The two examples shown above are for the lossless case. In cases (3)-(8) of Table 5.1, the amplitudes of the signal and pump sources in the first elements of the lines are the same as in case (1), but the elements are now lossy. The corresponding amplitudes of the signal and pump are shown in Fig. 5.9. In order not to overload the figures, we show the amplitude of the signal only in the top and the amplitude of the pump only in the bottom line. In the cases of Figs. 5.9a and b, the losses are low. The periodic exchange of power between the signal and the pump, which is observed in Fig. 5.7, is superimposed on their decline along the lines due to the loss. It can be seen that the position of the first maximum shifts

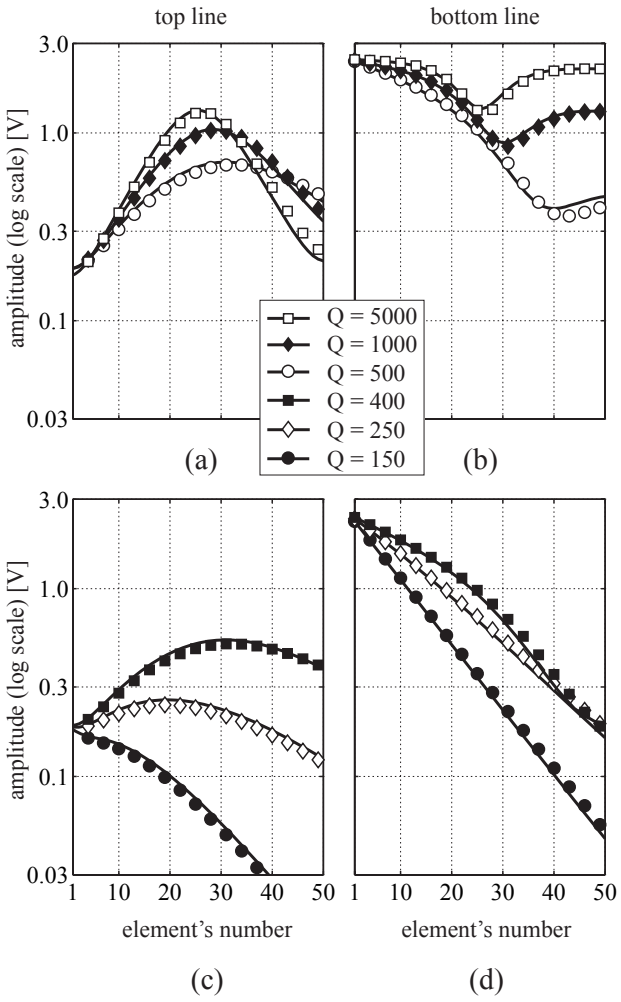

Figure 5.9: *Parametric amplification in the presence of loss. Solutions of the continuous (solid lines) and discrete (markers) models. The loss is low in the cases* (a), (b) *and high in the cases* (c), (d).

towards the end of the array. The maximum achieved value of the signal is naturally smaller than in the lossless case, Fig. 5.7.

As the loss increases, the situation changes qualitatively. The position of the signal's maximum shifts now towards the beginning of the array. It is around 30 elements for $Q = 400$ and 20 elements for $Q = 250$. For the case of $Q = 150$, the loss is high enough to completely suppress the amplification.

In more detail the position of the maximum of the signal as a function of loss is shown in Fig. 5.10 by filled circles. If the loss is negligible (Q is very high), then the maximum is reached at the length of 25 elements (see Fig. 5.7). With increase of the loss, the position shifts towards the end of the array until it reaches its maximal value for Q about 450. As the

loss increases further, the position of the maximum decreases, and it reaches the beginning of the array for Q around 200. At this value, amplification of the signal vanishes.

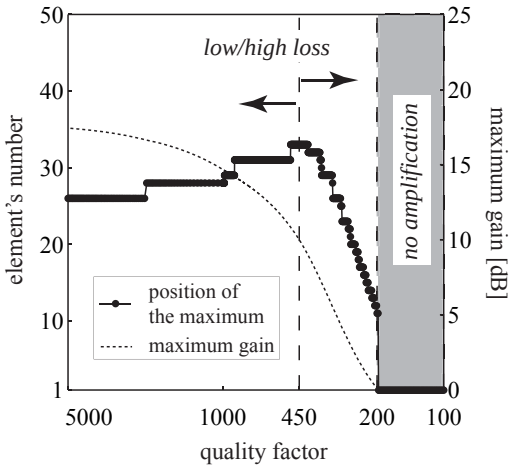

Figure 5.10: *The position of the maximum (filled circles) and the maximal value of the signal (dotted line) depending on the amount of loss. Three different regimes: low loss, high loss, and no amplification.*

This allows us to distinguish between three different regimes depending on the amount of loss: low-loss regime ($Q > 450$), high-loss regime ($200 \leqslant Q \leqslant 450$), and no-amplification regime ($Q < 200$). In each case, the behavior of the signal and pump amplitudes is different (see Fig. 5.9).

It should be mentioned that, as could be expected, the maximum value of the signal amplitude decreases monotonically with the increase of the loss. The maximum amplitude, as compared to the case without amplification, is around 17 dB for negligible loss and becomes zero for $Q = 200$ (see dotted line in Fig. 5.10).

Let us now discuss in more detail the practically significant case of high loss. In Fig. 5.11, the amplitudes of the signal and pump in the top and bottom lines are shown for case (9) of Table 5.1 with $Q = 100$ (note that the amplitudes of the sources are different now from the cases (3)-(8) of Table 5.1).

It can be seen that in this case there is no longer a periodic exchange of power between the signal and the pump. The amplitude of the pump wave decays exponentially along the line and can be written as

$$u_{\mathrm{p}}(z) = u_{\mathrm{p}}(0)e^{-\alpha_{\mathrm{p}}z}\,. \tag{5.53}$$

Equation for the amplitude of the signal wave, u_{s}, is then [from Eq. (5.50)]

$$\frac{\mathrm{d}u_{\mathrm{s}}(z)}{\mathrm{d}z} = -jg_{\mathrm{s}}u_{\mathrm{p}}(0)e^{-\alpha_{\mathrm{p}}z}u_{\mathrm{s}}^{*}(z) - \alpha_{\mathrm{s}}u_{\mathrm{s}}(z)\,. \tag{5.54}$$

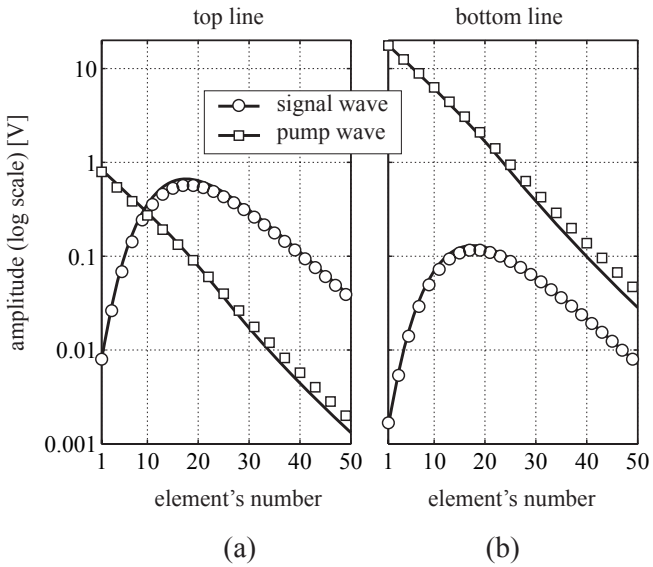

Figure 5.11: *Parametric amplification with undepleted pump in the presence of loss, top* (a) *and bottom* (b) *lines. Solutions by the discrete (circles and squares) and continuous (solid line) models for the case* (9) *of Table 5.1.*

In the case of initially weak signal, the solution is

$$u_{\mathrm{s}}(z) = u_{\mathrm{s}}(0) \exp\left[\frac{-g_u u_{\mathrm{p}}(0)}{\alpha_{\mathrm{p}}} \left(\exp(-\alpha_{\mathrm{p}} z) - 1\right) - \alpha_{\mathrm{s}} z\right], \tag{5.55}$$

from which the position of the maximum is readily obtained as

$$N_{\max} = \frac{1}{a\alpha_{\mathrm{p}}} \ln \frac{g_{\mathrm{s}} u_{\mathrm{p}}(0)}{\alpha_{\mathrm{s}}}. \tag{5.56}$$

For the parameters chosen, this gives the length of 17 elements, in agreement with Fig. 5.11. It can be seen that the amplitude of the signal is larger than its initial value in each element of the array. This means that the detrimental effect of losses is compensated by parametric amplification.

Appropriately choosing the parameters of the array it can be possible to achieve almost constant distribution of the signal amplitude along the array, as shown in Fig. 5.12 for the top line in the case (10) of Table 5.1. The amplitude of the signal with amplification is shown by the solid line and circles and without amplification by the dashed line.

It is gratifying to note that, similarly to the monatomic case, the agreement between the solutions by the discrete and continuous models is very good for each case of Figs. 5.7–5.12.

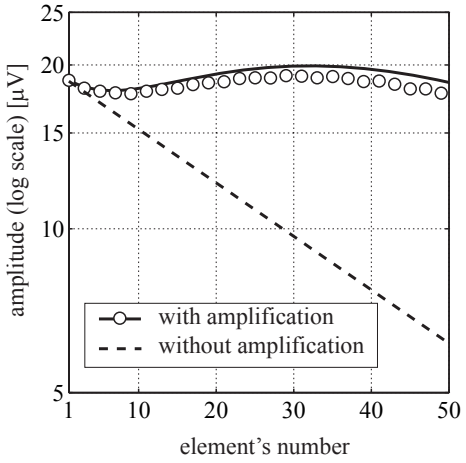

Figure 5.12: *Loss compensation by means of parametric amplification. The amplitude of the signal in the amplified case (solid line and circles) is almost constant along the array, whereas it declines exponentially in the non-amplified case (dashed) line.*

5.4 Amplification under rotational resonance

In the previous Sections of this Chapter, we have developed a theoretical formulation for parametric amplification of MI waves that propagate in linearly arranged metamaterial arrays. In this Section, we shall study parametric amplification in the arrays arranged into rings. As discussed previously in Section 4.4, MI waves in ring structures may exhibit a rotational resonance. This phenomenon can be advantageously used for the detection of a signal produced by a rotating dipole inside the ring under conditions of nuclear magnetic resonance. Parametric amplification of the signal at this early stage can be expected to lead to an improvement in the signal-to-noise ratio.

5.4.1 Rotational resonance and phase matching

An MI wave propagating along such ring has a resonance if βa satisfies the relation (see Section 4.4)

$$\beta a = \frac{2\pi}{N}\nu\,, \tag{5.57}$$

where ν is an integer. The resonant propagation constant is allowed to take a discrete set of values. Fortunately, this requirement does not contradict the phase-matching conditions (5.2): we can see that the propagation constant at the second-order resonance ($\nu = 2$) is twice as large as that at the first-order resonance ($\nu = 1$). It is exactly what is needed for the phase matching. Hence, adjusting the signal and pump waves to the first- and second-order resonance respectively, we can fulfill the phase-matching conditions.

For a planar arrangement, which is characterized by weak coupling between the elements, we have to use a diatomic configuration in order to have a dispersion relation that supports

both the signal and the pump. Schematic presentation of this configuration is shown in Fig. 5.13.

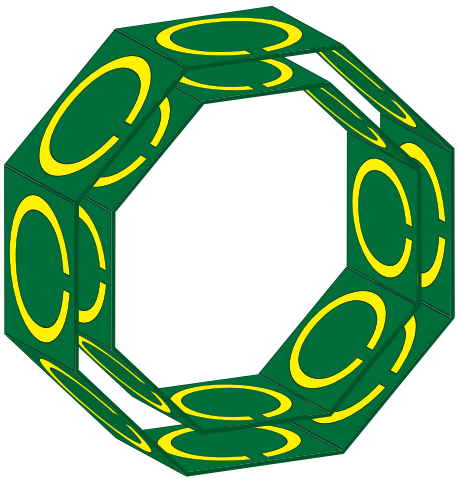

Figure 5.13: *Schematic presentation of two coupled ring resonators. Each ring consists of eight elements. The signal wave is excited by a rotating magnetic dipole in the middle, and the pump wave, by two voltage sources in the neighboring elements of the outer ring. The power is extracted from a resistive load in one of the elements.*

For our numerical calculations, we assume that both rings consist of eight elements. For the self-inductance of the elements and mutual inductance between them, we take the values from the example of Section 5.2.2. They are $L = 50$ nH, $M = 0.15L$, and $M_1 = -0.05L$. For the signal frequency we take, as in all previous examples, $\omega_s/(2\pi) = 63.87$ MHz. The values of the propagation constant, βa, are determined by the rotational resonance conditions: for the eight-element structure of Fig. 5.13, the first resonance occurs at $\beta_s a = \pi/4$, and the second, at $\beta_p a = \pi/2$. Solution of the dispersion equation (5.7) gives for the values of capacitances in the inner and outer rings, respectively, $C_1 = 133$ pF and $C_2 = 32$ pF.

5.4.2 Excitation of the traveling waves

We assume that the signal wave is excited at the first (fundamental) resonance by a rotating magnetic dipole with an angular velocity $\omega_s/(2\pi) = 63.87$ MHz that is placed in the center of the structure. The resonant frequency of the ring's elements, $\omega_{01}/(2\pi) = 61.72$ MHz, is close to the signal frequency. The radial component of the dipole's magnetic field induces signal voltages in the elements of the inner ring

$$U_s(n) = \frac{1}{2}\left[u_{s0}e^{j(\omega_s t - n\beta_s a)} + \text{c.c.}\right] . \tag{5.58}$$

We shall excite the pump wave at the second-order rotational resonance by two external phase-shifted voltage sources at the pump frequency that are placed in the first and second elements of the outer ring, respectively

$$\begin{aligned} U_p(1) &= \frac{1}{2}\left[u_{p0}e^{2j(\omega_s t - \beta_s a)} + \text{c.c.}\right] , \\ U_p(2) &= \frac{1}{2}\left[u_{p0}e^{2j(\omega_s t - 2\beta_s a)} + \text{c.c.}\right] . \end{aligned} \tag{5.59}$$

We shall extract power from a resistive load inserted in the first element of the inner ring. The value of the load resistance is taken to be equal to the self-resistance of the element.

Having determined the excitations we can formulate a system of nonlinear difference equations governing the amplitudes of the signal and pump waves in a way analogous to Eq. (5.39) from the previous Section.

For the case of the arrays arranged into lines, we could assume arbitrary initial phases of the signal and pump waves. If the initial amplitude of the pump wave is much larger than that of the signal wave (which should be true for most practical realizations) then the phase difference between the signal and pump waves does not depend on their initial values [87, 88]. Hence, the amplification is also independent on the initial phases.

For the ring structures, this is no longer true. One expects some similarity between parametric amplification in the ring resonator and that in conventional two-circuit amplifiers [91]. The latter depends significantly on the phase difference between the signal and pump.

We start, therefore, by looking at the initial phases of the signal and pump sources. For the quality factors of the elements and the amplitudes of the sources, we take $Q = 100$, $U_{s0} = 10 \times 10^{-6}$ V, and $V_{p0} = 0.125$ V. The value of the nonlinear parameter, γ, is taken as 0.1 V^{-1}. The pump source in the first element is now phase-shifted against the signal ones at a value of ϕ. We change now ϕ in the range $0 < \phi < 2\pi$. The power extracted from the first element in this case is shown in Fig. 5.14. It is normalized to the value of the power extracted without amplification and is shown in decibels.

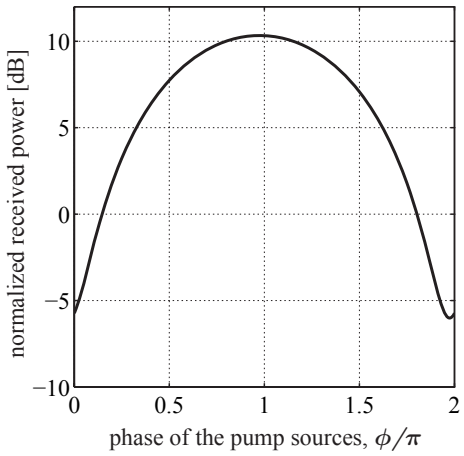

Figure 5.14: *Amplitude of the extracted signal power for different values of the phase difference between the signal and pump sources, ϕ. The maximum amplification is achieved when $\phi = \pi$.*

It can be seen that, as expected, the amount of amplification significantly depends on the phase. For the values of ϕ around 0 and 2π, the received signal is even smaller than in the case without nonlinear interaction. The maximum of the signal amplitude is observed when $\phi = \pi$, i. e. the pump source in the first element is in anti-phase with the signal ones.

5.4.3 Bistability of the parametric gain

Are there any further deviations from the case of linear arrangements? For linear arrangements, we find that the stronger is the pump the larger is the maximum amplitude of the amplified signal. For the ring structure, there is, however, a fine distinction that lies in the conditions of rotational resonance.

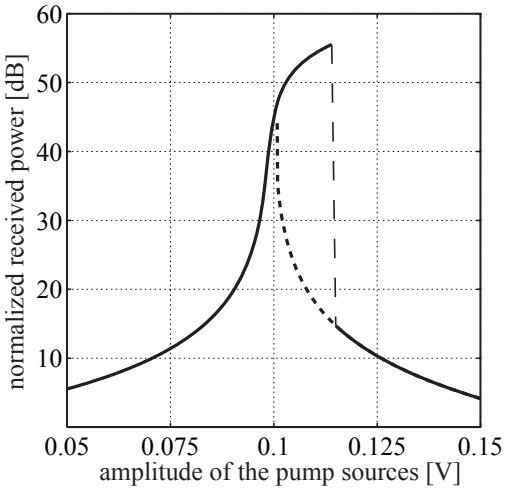

Figure 5.15: *Received signal power for different values of the pump amplitude. Pump power is increased for the solid line and is decreased for the dotted line.*

In our theory, the value of capacitance changes with the voltage applied to it, Eq. (5.3). The larger is the voltage, the larger is the capacitance leading to the change of the resonant frequency of the elements. This effect can be neglected for the linear arrangements but not for the rings. In a ring, a change of the resonant frequency of the elements leads to deviation from the rotational resonance conditions (5.57) and, consequently, to the mismatch between the rotational resonance frequency and the frequency of the signal wave. The amplitude of the signal should, therefore, decline with the increase of the pump amplitude.

A competing process is parametric amplification, which should lead to an increase of the signal's amplitude. One can, therefore, expect a maximum in amplification depending on the value of the pump amplitude.

In order to check this, we take the rings with the parameters defined above but vary now the amplitude of the pump sources in the range of $0.05 - 0.15$ V. The results for the extracted signal power are shown in decibels in Fig. 5.15 normalized to the power extracted from the first element without amplification. They are derived in two different ways: the solid line is obtained for the pump amplitude being increased from 0.05 to 0.15 V, and the dotted line, for the pump amplitude being decreased from 0.15 to 0.05 V.

It can be seen that, as expected, there is a maximum of amplification observed for the

pump amplitudes around 0.11 V. For the low and high values of the pump amplitude the solid and dotted lines coincide. Around the maximum, however, they are different: the extracted signal power has two different levels at the same value of the pump amplitude depending on whether the pump amplitude is decreased or increased. This effect of bistable response is well known in optics and nonlinear physics [100, 101]. In a practical device aiming at a stable operation, bistability of amplification can be avoided by choosing a value of pump amplitude away from the bistable regime. In Fig. 5.15, for example, amplitudes of the pump sources of around 0.07 and 0.125 V still give amplification of 10 dB and, at the same time, lie outside the bistable region.

Chapter 6

Summary and outlook

It is now time to summarize the results obtained and discuss their implications for possible future work. In the Introduction, we have set up the goal to consider effects that could have a potential for applications. In Chapter 2, we have briefly discussed the principles that govern the near-field behavior of the devices comprising magnetically coupled metamaterial elements. Having analyzed the properties of magnetoinductive waves, we have shown that more flexibility is needed for tailoring their dispersion than provided by simple "monatomic" configurations.

For this purpose, in Section 3.1, we have first studied in more detail magnetic coupling between a pair of magnetic metamaterial elements and have proven that it is anisotropic: positive, negative, and zero values of the coupling coefficient are achievable depending on the positions and orientations of the elements relative to each other.

As a next step, in Section 3.2, we have made use of the analogy between magnetoinductive waves in metamaterials and acoustic waves in solids. It is well known that the phonon dispersion in a diatomic solid differs from that in a monatomic one by having two distinct branches, an acoustic and an optical one. We have shown, both theoretically and experimentally, that the dispersion of magnetoinductive waves propagating on metamaterial arrays fabricated using the diatomic principle have similar properties.

Combining the results of Sections 3.1 and 3.2 we have generalized the possibilities for constructing diatomic configurations in Section 3.3. In the general case, a unit cell of a diatomic metamaterial consists of two elements with different resonant frequencies. The elements within a unit cell as well as the elements from the neighboring unit cells are coupled to each other via mutual inductances, whose values can be controlled by placing elements in different positions relative to each other.

The result of Chapter 3 is the tool for tailoring the dispersion of magnetoinductive waves. We have seen that by using diatomic rather than monatomic metamaterial configurations we gain considerably more freedom in designing the dispersion characteristics and, hence, in controlling the near-field behavior of the arrays.

In the Chapters that follow, we have discussed a number of potential applications. Chapter 4 is devoted to linear metamaterials. The effects we have considered are: shift-dependent transmission (Section 4.1), subwavelength imaging (Section 4.2), subwavelength focusing

(Section 4.3), and rotational resonance (Section 4.4).

In Section 4.1, tailoring the dispersion of magnetoinductive waves has been used for controlling the transmission properties of a diatomic metamaterial array. The array consisted of two planar lines that were placed one above the other. By shifting the lines relative to each other we could control the amount of power transmitted.

In Section 4.2, we have studied subwavelength imaging by diatomic metamaterial arrays. When two planar lines constituting a diatomic configuration are strongly coupled to each other, then the propagation of magnetoinductive waves at the resonant frequency of the elements (and hence the undesirable spreading of signal) can be avoided. It is possible then to image directly at the resonant frequency. Our analysis has confirmed the superior behavior of the double lens operating at the resonant frequency in comparison with the double and single lenses operating above and below the resonance.

In Section 4.3, we have studied an effect that is closely related to imaging – subwavelength focusing. We have shown that by tailoring the properties of the receiver in a transmitter-lens-receiver configuration it is possible to place a subwavelength focus in an arbitrary position in space independently of the properties of the transmitter and the lens.

In the final Section of Chapter 4, we have studied the rotational resonance of magnetoinductive waves propagating on ring metamaterial structures. In our analysis, the signal was excited by a rotating magnetic dipole placed in the center of the ring. We have shown that by tailoring the properties of the ring's elements it is possible to achieve beneficial extraction of the signal's power. The ring configuration, therefore, has potential as a detection system in Magnetic Resonance Imaging.

Having in mind improvement of the signal-to-noise ratio in Magnetic Resonance Imaging and compensation of losses in metamaterials, we have proceeded with a study of parametric amplification of magnetoinductive waves in Chapter 5. We have first considered the phase-matching problem and shown that it can be solved for monatomic as well as for diatomic metamaterial arrays by tailoring their properties. The corresponding theoretical formulations of parametric amplification in both cases have been developed in Section 5.3. In Section 5.4, we have considered parametric amplification in ring resonators. We have theoretically demonstrated the loss compensation and increase of the extracted power by parametric amplification in metamaterial arrays.

We have, therefore, succeeded in achieving the goals we set up at the beginning: we have developed mechanisms for tailoring the properties of metamaterials and have applied these mechanisms to a variety of effects involving guiding and detecting of magnetoinductive waves as well as subwavelength imaging and focussing. What could be done further in this direction?

There is always a gap between demonstrations of an effect that might have a potential for applications and developing actual devices based on it. Thinking about metamaterials, further studies should be aimed at closing this gap. In particular, the extraction of power from the ring resonators, first, in linear and then in nonlinear (with amplification) cases could be studied experimentally. It would require more accurate models, which take into account the properties of actual nonlinear components and of the circuits needed for biasing the varactor diodes.

The searching for more efficient ways of fulfilling phase-matching conditions for parametric amplification could result in more complicated nonlinear metamaterial elements. Such elements should be doubly resonant: able to resonate at the frequencies of the signal and pump waves. It would, of course, require developing the corresponding theoretical formulation of parametric amplification in the way analogous to that used in Chapter 5.

There is a number of nonlinear effects having both theoretical and practical significance that could be studied applying the circuit models of metamaterials. They are, first of all, the effects involving propagation of electromagnetic waves in metamaterials and their interaction with magnetoinductive waves. The obvious candidates for investigations are parametric amplification of electromagnetic waves, second-harmonic generation, and phase-conjugation. Discussed briefly in Chapter 5 for magnetoinductive waves, second harmonic generation is of minor importance at megahertz frequency range, which is thoroughly covered by a variety of sources. At terahertz and optical frequencies, however, this might be an issue of major interest. Second harmonic generation with metamaterials, whose elements can be designed having different resonant frequencies, could provide efficient sources of radiation in a wide frequency range.

In this thesis, we have considered magnetic metamaterials that operate in the megahertz frequency region. Combined with the earlier studies, the results obtained here provide a comprehensive analysis of the physical properties of linear and nonlinear low-frequency metamaterials. Mathematical formalisms developed earlier and generalized in this work for nonlinear metamaterials [102] have already allowed to solve a wide range of problems involving signal guiding [23,39,40,56,85], processing [26,48,49,55,57,85,97,98,103], detection [19], subwavelength imaging [18, 104], and focussing [105] with magnetic metamaterials.

A natural step for further studies is to move towards smaller wavelengths. All the dimensions becoming much smaller demands firstly more sophisticated technology, and secondly a more complicated theory. The size of the element being comparable with the wavelength implies nonuniform current distribution and radiation in preferred directions. The distance between the elements being comparable with the wavelength means that the radiation term is no longer negligible and higher order interactions must be taken into account-possibly all interactions between all the elements [53].

There are obviously applications of metamaterials in the visible range similar to those for microwaves, i. e. guiding the waves and processing information. However, coherent optical technology is so well advanced (ever since the emergence of optical fibre communications) that new devices would have great difficulties in penetrating the market place. The most likely application of metamaterials would be in the largely unexplored tens of terahertz range for security. A hand-held device to look at hidden objects would be of great value in our security conscious world. This frequency band is largely unexplored at the moment partly because there are no suitable coherent sources available and partly because the familiar technologies associated with millimeter and optical waves are not readily applicable. Metamaterials have a chance both for providing slow wave structures for possible oscillators and for signal processing.

Appendix A

Mutual inductance for two arbitrary oriented loops

Here we generalize the known results for the mutual inductance, M, between two loops [51] for the case when they can have arbitrary radiuses, positions in space and orientations. The general model in shown in Fig. A.1. The first loop has a radius r_1 and its center is situated at the point $(x_1, y_1, z_1)^T$ (here the superscript T means transposed of a vector). The orientation of the loop is determined by two angles, θ_1 and φ_1, in the cylindrical coordinate system. The second loop has a radius r_2 and its center is situated at the point $(x_2, y_2, z_2)^T$. The orientation of the second loop is given by the angles θ_2 and φ_2.

It order to determine the mutual inductance we use the known expressions for the vector potential of a single loop [50, 51]. It is convenient to consider the problem in cylindrical coordinates. The vector potential of a loop with the radius r_1 situated at the $(0, 0, 0)^T$ point and oriented in the (x, y)-plane (see Fig. A.2) has only A_φ component

$$A_\varphi = \frac{\mu_0 I}{4\pi} \int \frac{\mathbf{e}_\varphi \mathbf{dl}}{r} = \frac{\mu_0 I}{4\pi} \int_0^{2\pi} \frac{\cos\varphi' d\varphi'}{\sqrt{(\rho - r_1 \cos\varphi')^2 + (r_1 \sin\varphi')^2 + z^2}}. \tag{A.1}$$

Here $\mathbf{dl}$ is the current element with cylindrical coordinates $(r_1, \varphi', 0)$; r is the distance between $\mathbf{dl}$ and the point P.

A_φ can be expressed in terms of elliptic integrals

$$A_\varphi = \frac{\mu_0 I}{2\pi} \frac{\sqrt{r_1}}{\sqrt{\rho}} \left[\left(\frac{2}{\chi} - \chi \right) K(\chi) - \frac{2}{\chi} E(\chi) \right], \tag{A.2}$$

where

$$\chi = \frac{2\sqrt{r_1 \rho}}{\sqrt{(\rho + r_1)^2 + z^2}} \tag{A.3}$$

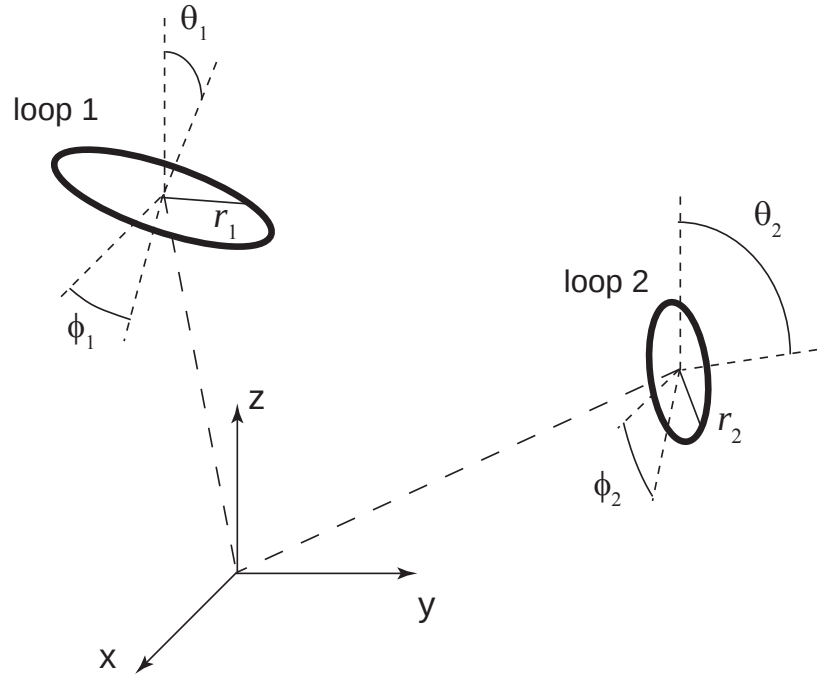

Figure A.1: *Schematic presentation of two loop elements for the calculation of mutual induction. The loops can have different radii, arbitrary positions in space, and arbitrary orientations.*

and $K(\chi)$ and $E(\chi)$ are elliptic integral of the first and the second kind respectively

$$\begin{aligned} K(\chi) &= \int_0^{\pi/2} \frac{1}{\sqrt{1-\chi\sin^2\alpha}}\, d\alpha \\ E(\chi) &= \int_0^{\pi/2} \sqrt{1-\chi\sin^2\alpha}\, d\alpha \end{aligned} \quad . \tag{A.4}$$

The mutual inductance M between two loops is then given by

$$M = \frac{1}{I}\int_{\text{loop2}} \mathbf{A}_{\text{loop1}}\mathbf{dl}_{\text{loop2}}\,. \tag{A.5}$$

To determine M in the case of arbitrary oriented loops we first define two rotation matrices

$$\mathbf{Q}_{1,2} = \begin{pmatrix} \cos\theta_{1,2}\cos\varphi_{1,2} & \cos\theta_{1,2}\sin\varphi_{1,2} & -\sin\theta_{1,2} \\ -\sin\varphi_{1,2} & \cos\varphi_{1,2} & 0 \\ \sin\theta_{1,2}\cos\varphi_{1,2} & \sin\theta_{1,2}\sin\varphi_{1,2} & \cos\theta_{1,2} \end{pmatrix}. \tag{A.6}$$

Then denoting

$$\mathbf{R}(\psi) = \mathbf{Q}_1\left[\begin{pmatrix} x_2-x_1 \\ y_2-y_1 \\ z_2-z_1 \end{pmatrix} + r_2\mathbf{Q}_2^T\begin{pmatrix} -\sin\psi \\ \cos\psi \\ 0 \end{pmatrix}\right] \tag{A.7}$$

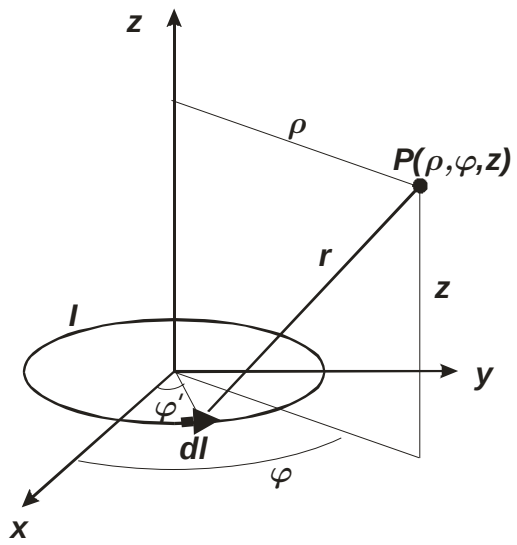

Figure A.2: *Determination of the vector potential of a single loop.*

and

$$\eta = \frac{4r_1\sqrt{R_x(\psi)^2 + R_y(\psi)^2}}{\left(r_1 + \sqrt{R_x(\psi)^2 + R_y(\psi)^2}\right)^2 + R_z(\psi)^2} \tag{A.8}$$

the final expression for the mutual induction can be obtained in the form

$$\begin{aligned} M = {} & \frac{\mu_0\sqrt{r_1}}{2\pi}\int_0^{2\pi} \frac{r_2}{\sqrt{R_x^2(\psi) + R_y^2(\psi)}} \times \\ & \times \left[\left(\frac{2}{\sqrt{\eta}} - \sqrt{\eta}\right)K(\eta) - \frac{2}{\sqrt{\eta}}E(\eta)\right] \begin{pmatrix} -R_y(\psi) \\ R_x(\psi) \\ 0 \end{pmatrix}^T \mathbf{Q}_1\mathbf{Q}_2^T \begin{pmatrix} -\sin\psi \\ \cos\psi \\ 0 \end{pmatrix} d\psi \end{aligned} . \tag{A.9}$$

Appendix B

Rotational resonance: Extracting maximum power

We shall find here analytic expressions for the maximum extracted power and optimum load impedances in a ring resonator under rotational resonance in the two cases:

- only the first element is loaded by a load impedance, $Z_{\rm L}$;
- the first element is loaded by a load impedance, $Z_{\rm L}$; the second and the last elements are loaded by additional tuning impedances, $Z_{\rm tune\,2,N}$.

We assume here that the quality factor of the elements is high, $Q \to \infty$. Let us denote:

$$w_i = \frac{Z_{0_i}}{Z_{\rm m}}\,,$$

where Z_0 is the self-impedance of the elements, Eq. (2.6), $Z_{\rm m} = j\omega M$ is a mutual impedance between the nearest neighbors, and $i = 1 \ldots N$ denotes the element's number.

The impedance matrix, Eq. (2.16), of the ring [19] can then be presented in the block form

$$\mathbf{Z}_{\rm R} = Z_{\rm m}^N \begin{pmatrix} w_1 & \mathbf{b} \\ \mathbf{b}^T & \mathbf{A} \end{pmatrix}\,, \tag{B.1}$$

where $\mathbf{b}$ is an $N-1$ dimensional vector

$$\mathbf{b} = (1, 0, \ldots, 0, 1)\,.$$

Here the superscript T denotes transpose of a vector, and $\mathbf{A}$ is a tridiagonal $(N-1)\times(N-1)$ matrix [106] of the form

$$\mathbf{A} = \begin{pmatrix} w_2 & 1 & 0 & \ldots & 0 \\ 1 & w_3 & 1 & \ddots & \vdots \\ 0 & \ddots & \ddots & \ddots & 0 \\ \vdots & \ddots & 1 & w_{N-1} & 1 \\ 0 & \ldots & 0 & 1 & w_N \end{pmatrix}\,. \tag{B.2}$$

We add a load impedance in the fist element. The current, I_1, flowing in it is

$$I_1 = \sum_{n=1}^{N} \mathbf{Z}^{-1}_{\mathrm{R}_{1,\mathrm{n}}} V_n \,, \tag{B.3}$$

where V_n is the voltage applied to the n^{th} element. In order to find the current I_1 we need to know the first row of the inverted matrix of the ring, $\mathbf{Z}_{\mathrm{R}}^{-1}$. For the block matrix (B.1), the inverted matrix is given by

$$\mathbf{Z}_{\mathrm{R}}{}^{-1} = \begin{pmatrix} K^{-1} & -K^{-1}\mathbf{b}\mathbf{A}^{-1} \\ -\mathbf{A}^{-1}\mathbf{b}^T K^{-1} & \mathbf{A}^{-1} + \mathbf{A}^{-1}\mathbf{b}^T K^{-1}\mathbf{b}\mathbf{A}^{-1} \end{pmatrix} , \tag{B.4}$$

where K is given by

$$K = w_1 - \mathbf{b}\mathbf{A}^{-1}\mathbf{b}^T \,.$$

Let us denote

$$\mathbf{\Phi} = \mathbf{A}^{-1} \,.$$

Then K is a number such that

$$K^{-1} = \frac{1}{w_0 - (\Phi_{1,1} + \Phi_{1,N-1} + \Phi_{N-1,1} + \Phi_{N-1,N-1})} \,, \tag{B.5}$$

and $\mathbf{b}\mathbf{A}^{-1}$ is a row-vector

$$\mathbf{b}\mathbf{A}^{-1} = (\Phi_{1,1} + \Phi_{N-1,1}, \Phi_{1,2} + \Phi_{N-1,2}, \ldots, \Phi_{1,N-1} + \Phi_{N-1,N-1}) \,. \tag{B.6}$$

Under the excitation of rotational resonance by a magnetic dipole the voltages in the elements have the form

$$V_n = \exp\left(j\frac{2\pi n}{N}\right) , \tag{B.7}$$

and we can write then for the current in the first element

$$I_1 = \frac{1 - \sum_{n=1}^{N-1} (\Phi_{1,n} + \Phi_{N-1,n}) \exp\left(j\frac{2\pi n}{N}\right)}{w_1 - (\Phi_{1,1} + \Phi_{1,N-1} + \Phi_{N-1,1} + \Phi_{N-1,N-1})} \,, \tag{B.8}$$

Let us now assume a load impedance, Z_{L}, in the first element of the ring and two additional tuning reactances of the same absolute value but different signs ($Z_{\mathrm{tune\,2}} = Z_{\mathrm{tune}}$ and $Z_{\mathrm{tune\,N}} = -Z_{\mathrm{tune}}$) in the second and the last, N^{th}, elements. We can then write

$$w_1 = 2x + l, \qquad w_2 = 2x + t, \qquad w_{3,\ldots,N-1} = 2x, \qquad w_N = 2x - t \,, \tag{B.9}$$

where

$$x = \frac{Z_0}{2Z_{\mathrm{m}}} \,, \qquad l = \frac{Z_{\mathrm{L}}}{Z_{\mathrm{m}}} \,, \qquad t = \frac{Z_{\mathrm{tune}}}{Z_{\mathrm{m}}} \,.$$

Using the procedure for analytical inversion of tridiagonal matrices [107] we can then rewrite the denominator of the expression for the current in the first element, Eq. (B.8), as

$$\begin{aligned} & w_1 - (\Phi_{1,1} + \Phi_{1,N-1} + \Phi_{N-1,1} + \Phi_{N-1,N-1}) = \\ & = l + 2x - \frac{2U_{N-2}(x) + 2(-1)^N}{U_{N-1}(x) - t^2 U_{N-3}(x)} = \\ & = l + \frac{2xU_{N-1}(x) - U_{N-2}(x) - U_{N-2}(x) - 2(-1)^N - 2t^2 x U_{N-3}(x)}{U_{N-1}(x) - t^2 U_{N-3}(x)} = \\ & = l + \frac{U_N(x) - U_{N-2}(x) - 2(-1)^N - 2t^2 x U_{N-3}(x)}{U_{N-1}(x) - t^2 U_{N-3}(x)}\,, \end{aligned} \tag{B.10}$$

where $U_n(x)$ are Chebyshev polynomials of the second kind [108]. The load impedance is an optimum when

$$Z_{\mathrm{L}} = Z_{\mathrm{m}} \frac{U_N(x) - U_{N-2}(x) - 2(-1)^N - 2t^2 x U_{N-3}(x)}{U_{N-1}(x) - t^2 U_{N-3}(x)}\,. \tag{B.11}$$

Power extracted without tuning reactances

Let us now consider the case $t = 0$, i. e. there is only a load impedance in the first element and no tuning reactances in the neighboring elements. The optimum load impedance is then given by

$$Z_{\mathrm{L}}^0 = Z_{\mathrm{m}} \frac{U_N(x) - U_{N-2}(x) - 2(-1)^N}{U_{N-1}(x)}\,. \tag{B.12}$$

We are working under rotational resonance, Eq. (4.8). For the first, fundamental, resonance we can write from the dispersion relation for MI waves

$$x = \frac{Z_0}{2Z_{\mathrm{m}}} = -\cos ka \qquad ka = \frac{2\pi}{N} - j\alpha a\,, \tag{B.13}$$

where α is the attenuation constant. Using the property of Chebyshev polynomials that

$$U_n(\cos\theta) = \frac{\sin[(n+1)\theta]}{\sin\theta} \tag{B.14}$$

and recalling that αa must be small we can rewrite Eq. (B.12) as

$$Z_{\mathrm{L}}^{(0)} = Z_{\mathrm{m}} \tan\frac{jN\alpha a}{2} \sin\left(\frac{2\pi}{N} + j\alpha a\right) \approx Z_{\mathrm{m}} N \sin\frac{2\pi}{N} \sin(j\alpha a)\,. \tag{B.15}$$

For the small losses, we can write from Eq. (B.13)

$$\sin\frac{2\pi}{N} \sin(j\alpha a) = \frac{Z_0}{2Z_{\mathrm{m}}}\,. \tag{B.16}$$

Hence finally we have for the optimum load

$$Z_{\mathrm{L}}^{(0)} = \frac{NR}{2}\,. \tag{B.17}$$

The ratio of the power extracted in this case to the power extracted in the uncoupled case can be found as

$$\frac{P_{\mathrm{load}}}{P_{\mathrm{uncoupled}}} = \frac{N}{2}\,. \tag{B.18}$$

Power extracted with tuning reactances

Let us now assume now that there are tuning reactances in the second and last elements of the ring as given by Eq. (B.9). We have already assumed that they have the same absolute value but different signs. The question we are asking ourselves here is: How the absolute values of the reactances is connected to the parameters of the ring.

To answer this question we use the results of the numerical calculations [19] that show that the optimum load impedance in this case is

$$Z_{\mathrm{L}}^{(1)} = NR\,. \tag{B.19}$$

Comparing this with Eq. (B.17) we can write from Eq. (B.11)

$$\frac{U_N(x) - U_{N-2}(x) - 2(-1)^N - 2t^2 x U_{N-3}(x)}{U_{N-1}(x) - t^2 U_{N-3}(x)} = 2\frac{U_N(x) - U_{N-2}(x) - 2(-1)^N}{U_{N-1}(x)}\,, \tag{B.20}$$

which gives for t

$$t^2 = \frac{U_{N-1}(U_N - U_{N-2} - 2(-1)^N)}{2U_{N-3}(U_N - U_{N-2} - 2(-1)^N - xU_{N-1})}\,. \tag{B.21}$$

Taking into account the rotational resonance conditions (B.13) and using the definitions for the Chebyshev polynomials, Eq. (B.14), the value of the tuning reactances can be obtained in the form

$$Z_{\mathrm{tune\,2,N}} = \pm j\frac{NR}{2\sin\dfrac{4\pi}{N}}\,. \tag{B.22}$$

The power extracted in this case as compared to the uncoupled case is

$$\frac{P_{\mathrm{tune}}}{P_{\mathrm{uncoupled}}} = N\,. \tag{B.23}$$

Bibliography

[1] A. Sihvola, Metamaterials in electromagnetics, *Metamaterials* **1**, 2–11 (2007).

[2] J. B. Pendry, Negative refraction makes a perfect lens, *Phys. Rev. Lett.* **85**, 3966–3969 (2000).

[3] V. G. Veselago, The electrodynamics of substances with simultaneously negative values of ϵ and μ, *Sov. Phys. Usp.* **10**, 509–514 (1968), (translated from *Usp. Fiz. Nauk* **92**, 517, 1967).

[4] D. R. Smith, W. J. Padilla, D. C. Vier, S. C. Nemat-Nasser, and S. Schultz, Composite medium with simultaneously negative permeability and permittivity, *Phys. Rev. Lett.* **84**, 4184–4187 (2000).

[5] R. A. Shelby, D. R. Smith, and S. Schultz, Experimental verification of a negative index of refraction, *Science* **292**, 77–79 (2001).

[6] E. Shamonina and L. Solymar, Metamaterials: How the subject started, *Metamaterials* **1**, 12–18 (2007).

[7] V. A. Kalinin and V. V. Shtykov, On the possibility of reversing the front of radio waves in an artificial nonlinear medium, *Sov. J. Commun. Techn. & Electron.* **36**, 96–102 (1991).

[8] M. Lapine, M. Gorkunov, and K. H. Ringhofer, Nonlinearity of a metamaterial arising from diode insertions into resonant conductive elements, *Phys. Rev. E* **67**, 065601(R)–1–4 (2003).

[9] A. A. Zharov, I. V. Shadrivov, and Y. S. Kivshar, Nonlinear properties of left-handed metamaterials, *Phys. Rev. Lett.* **91**, 037401–1–4 (2003).

[10] V. M. Agranovich, Y. R. Shen, R. H. Baughman, and A. A. Zakhidov, Linear and nonlinear wave propagation in negative refraction metamaterials, *Phys. Rev. B* **69**, 165112–1–7 (2004).

[11] M. Gorkunov and M. Lapine, Tuning of a nonlinear metamaterial band gap by an external magnetic field, *Phys. Rev. B* **70**, 235109–1–9 (2004).

[12] M. Lapine and M. Gorkunov, Three-wave coupling of microwaves in metamaterial with nonlinear resonant conductive elements, *Phys. Rev. E* **70**, 066601–1–8 (2004).

[13] I. Kourakis and P. K. Shukla, Nonlinear propagation of electromagnetic waves in negative-refraction-index composite materials, *Phys. Rev. E* **72**, 016626–1–5 (2005).

[14] A. K. Popov and V. M. Shalaev, Compensating losses in negative-index metamaterials by optical parametric amplification, *Opt. Lett.* **31**, 2169–2171 (2006).

[15] I. V. Shadrivov, A. A. Zharov, and Y. S. Kivshar, Second-harmonic generation in nonlinear left-handed metamaterials, *J. Opt. Soc. Am. B* **23**, 529–534 (2006).

[16] M. C. K. Wiltshire, J. V. Hajnal, J. B. Pendry, D. J. Edwards, and C. J. Stevens, Metamaterial endoscope for magnetic field transfer: near field imaging with magnetic wires, *Opt. Express* **11**, 709–715 (2003).

[17] O. Zhuromskyy, E. Shamonina, and L. Solymar, 2D metamaterials with hexagonal structure: spatial resonances and near field imaging, *Opt. Express* **13**, 9299–9309 (2005).

[18] M. J. Freire and R. Marques, Near-field imaging in the megahertz range by strongly coupled magnetoinductive surfaces: Experiment and ab initio analysis, *J. App. Phys.* **100**, 063105–1–9 (2006).

[19] L. Solymar, O. Zhuromskyy, O. Sydoruk, E. Shamonina, I. R. Young, and R. R. A. Syms, Rotational resonance of magnetoinductive waves: Basic concept and application to nuclear magnetic resonance, *J. Appl. Phys.* **99**, 123908–1–8 (2006).

[20] G. V. Eleftheriades and K. G. Balmain, *Negative Refraction Metamaterials: Fundamental Principles and Applications*, Wiley-IEEE Press, Hoboken, New Jersey, 2005.

[21] C. Caloz and T. Itoh, *Electromagnetic Metamaterials: Transmission Line Theory and Microwave Applications*, Wiley-IEEE Press, Hoboken, New Jersey, 2005.

[22] N. Engheta and R. W. Ziolkowski, editors, *Metamaterials: Physics and engineering explorations*, John Wiley and Sons Inc., New York, 2006.

[23] E. Shamonina, V. A. Kalinin, K. H. Ringhofer, and L. Solymar, Magneto-inductive waveguide, *Electron. Lett.* **38**, 371–373 (2002).

[24] R. Marques, J. Martel, F. Mesa, and F. Medina, Left-handed-media simulation and transmission of EM waves in subwavelength split-ring-resonator loaded metallic waveguides, *Phys. Rev. Lett.* **89**, 183901–1–4 (2002).

[25] F. Martin, F. Falcone, J. Bonache, R. Marques, and M. Sorolla, Miniature coplanar waveguide stop band filters based on multiple tuned split ring resonators, *IEEE Microw. Wireless Comp. Lett.* **13**, 511–513 (2003).

[26] R. R. A. Syms, E. Shamonina, and L. Solymar, Magneto-inductive waveguide devices, *IEE Proc.- Microw. Antennas Prop.* **153**, 111–121 (2006).

[27] D. Wu, N. Fang, C. Sun, X. Zhang, W. J. Padilla, D. N. Basov, D. R. Smith, and S. Schultz, Terahertz plasmonic high pass filter, *Appl. Phys. Lett.* **83**, 201–203 (2003).

[28] T. J. Yen, W. J. Padilla, N. Fang, D. C. Vier, D. R. Smith, J. B. Pendry, D. N. Basov, and X. Zhang, Terahertz magnetic response from artificial materials, *Science* **5663**, 1494–1496 (2004).

[29] H. O. Moser, B. D. F. Casse, O. Wilhelmi, and B. T. Saw, Terahertz Response of a Microfabricated Rod–Split-Ring-Resonator Electromagnetic Metamaterial, *Phys. Rev. Lett.* **94**, 063901–1–4 (2005).

[30] H.-T. Chen, W. J. Padilla, J. M. O. Zide, A. C. Gossard, A. J. Taylor, and R. D. Averitt, Active terahertz metamaterial devices, *Nature* **444**, 597–600 (2006).

[31] S. Linden, C. Enkrich, M. Wegener, J. Zhou, T. Koschny, and C. M. Soukoulis, Magnetic response of metamaterials at 100 THz, *Science* **306**, 1351–1353 (2004).

[32] G. Dolling, C. Enkrich, M. Wegener, J. F. Zhou, C. M. Soukoulis, and S. Linden, Cut-wire pairs and plate pairs as magnetic atoms for optical metamaterials, *Opt. Lett.* **30**, 3198–3200 (2005).

[33] S. Zhang, W. Fan, N. C. Panoiu, K. J. Malloy, R. M. Osgood, and S. R. J. Brueck, Experimental demonstration of near-infrared negative-index metamaterials, *Phys. Rev. Lett.* **95**, 137404–1–4 (2005).

[34] V. M. Shalaev, W. Cai, U. K. Chettiar, H.-K. Yuan, A. K. Sarychev, V. P. Drachev, and A. V. Kildishev, Negative index of refraction in optical metamaterials, *Opt. Lett.* **30**, 3356–3358 (2005).

[35] G. Dolling, M. Wegener, C. M. Soukoulis, and S. Linden, Negative-index metamaterial at 780 nm wavelength, *Opt. Lett.* **32**, 53–55 (2007).

[36] W. Hardy and L. Whitehead, Split-ring resonator for use in magnetic resonance from 200-2000 MHz, *Rev. Sci. Instrum.* **52**, 213–216 (1981).

[37] W. Froncisz and J. S. Hyde, The loop-gap resonator: A new microwave lumped circuit ESR sample structure, *J. Mag. Res.* **47**, 515–521 (1982).

[38] J. B. Pendry, A. J. Holden, D. J. Robbins, and W. J. Stewart, Magnetism from conductors and enhanced nonlinear phenomena, *IEEE Trans. Microwave Theory Tech.* **47**, 2075–2084 (1999).

[39] E. Shamonina, V. A. Kalinin, K. H. Ringhofer, and L. Solymar, Magnetoinductive waves in one, two, and three dimensions, *J. Appl. Phys.* **92**, 6252–6261 (2002).

[40] M. C. K. Wiltshire, E. Shamonina, I. R. Young, and L. Solymar, Dispersion characteristics of magneto-inductive waves: comparison between theory and experiment, *Electron. Lett.* **39**, 215–217 (2003).

[41] J. D. Baena, R. Marques, F. Medina, and J. Martel, Artificial magnetic metamaterial design by using spiral resonators, *Phys. Rev. B* **69**, 014402–1–5 (2004).

[42] G. Goussetis, A. P. Feresidis, S. Wang, Y. Guo, and J. C. Vardaxoglou, Uniplanar left-handed artificial metamaterials, *J. Opt. A: Pure & Appl. Opt.* **7**, 44–50 (2005).

[43] R. Marques, F. Mesa, J. Martel, and F. Medina, Comparative analysis of edge- and broadside-coupled split ring resonators for metamaterial design. Theory and experiment, *IEEE Trans. Antennas and Prop.* **51**, 2572–2581 (2003).

[44] M. Shamonin, E. Shamonina, V. Kalinin, and L. Solymar, Properties of a metamaterial element: Analytical solutions and numerical simulations for a singly split double ring, *J. Appl. Phys.* **95**, 3778–3784 (2004).

[45] S. O'Brien and J. B. Pendry, Magnetic activity at infrared frequencies in structured metallic photonic crystals, *J. Phys.:Condens. Matter* **14**, 6383–6394 (2002).

[46] P. Gay-Balmaz and O. J. F. Martin, Electromagnetic resonances in individual and coupled split-ring resonators, *J. Appl. Phys.* **92**, 2929–2936 (2002).

[47] C. R. Simovski, P. A. Belov, and S. He, Backward wave region and negative material parameters of a structure formed by lattices of wires and split-ring resonators, *IEEE Trans. Antennas and Prop.* **51**, 2582–2591 (2003).

[48] M. J. Freire, R. Marques, F. Medina, M. A. G. Laso, and F. Martín, Planar magnetoinductive wave transducers: theory and applications, *Appl. Phys. Lett.* **85**, 4439–4441 (2004).

[49] I. S. Nefedov and S. A. Tretyakov, On potential applications of metamaterials for the design of broadband phase shifters, *Microw. Opt. Technol. Lett.* **45**, 98–103 (2005).

[50] L. Solymar, *Lectures on Electromagnetic Theory*, Oxford University Press, Oxford, 1976.

[51] L. D. Landau and E. M. Lifschitz, *Electrodynamics of Continuous Media*, Pergamon Press, Oxford, 1984.

[52] A. Radkovskaya, M. Shamonin, C. J. Stevens, G. Faulkner, D. J. Edwards, E. Shamonina, and L. Solymar, An experimental study of the properties of magnetoinductive waves in the presence of retardation, *J. Magn. Magn. Mat.* **300**, 29–32 (2006).

[53] O. Zhuromskyy, E. Shamonina, and L. Solymar, Effect of radiation on dispersion of magneto-inductive waves in a metamaterial, *Proc. SPIE* **5955**, 595506–1–6 (2005).

[54] R. R. A. Syms, O. Sydoruk, E. Shamonina, and L. Solymar, Higher order interactions in magneto-inductive waveguides, *Metamaterials* **1**, 44–51 (2007).

[55] R. R. A. Syms, E. Shamonina, and L. Solymar, Absorbing terminations for magneto-inductive waveguides, *IEE Proc.-Microw. Antennas Prop.* **152**, 77–82 (2005).

[56] M. C. K. Wiltshire, E. Shamonina, I. R. Young, and L. Solymar, Experimental and theoretical study of magneto-inductive waves supported by one-dimensional arrays of "swiss rolls", *J. Appl. Phys.* **95**, 4488–4493 (2004).

[57] E. Shamonina and L. Solymar, Magneto-inductive waves supported by metamaterial elements: components for a one-dimensional waveguide, *J. Phys. D: Appl. Phys.* **37**, 362–367 (2004).

[58] R. R. A. Syms, E. Shamonina, V. Kalinin, and L. Solymar, A theory of metamaterials based on periodically loaded transmission lines: Interaction between magnetoinductive and electromagnetic waves, *J. Appl. Phys.* **97**, 064909–1–6 (2005).

[59] R. R. A. Syms, E. Shamonina, and L. Solymar, Positive and negative refraction of magnetoinductive waves in two dimensions, *Eur. Phys. J. B* **46**, 301–308 (2005).

[60] G. Atabekov, *Linear Network Theory*, Pergamon Press, Oxford, 1965.

[61] R. A. Silin and V. P. Sazonov, *Slow Wave Structures*, Boston SPA Eng., National Lending Library for Science and Technology, 1971.

[62] G. H. Knittel, A. Hessel, and A. A. Oliner, Element pattern nulls in phased arrays and their relation to guided waves, *Proc. IEEE* **56**, 1822–1836 (1968).

[63] M. Quinten, A. Leitner, J. Krenn, and F. Aussenegg, Electromagnetic energy transport via linear chains of silver nanoparticles, *Opt. Lett.* **23**, 1331–1333 (1998).

[64] M. L. Brongersma, J. W. Hartman, and H. A. Atwater, Electromagnetic energy transfer and switching in nanoparticle chain arrays below the diffraction limit, *Phys. Rev. B* **62**, R16356–R16359 (2000).

[65] W. H. Weber and G. W. Ford, Propagation of optical excitations by dipolar interactions in metal nanoparticle chains, *Phys. Rev. B* **70**, 125429–1–8 (2004).

[66] S. A. Tretyakov and A. J. Viitanen, Line of periodically arranged passive dipole scatterers, *Electr. Eng.* **82**, 353–361 (2000).

[67] N. Stefanou and A. Modinos, Impurity bands in photonic insulators, *Phys. Rev. B* **57**, 12127–1–7 (1997).

[68] A. Yariv, Y. Xu, R. K. Lee, and A. Scherer, Coupled-resonator optical waveguide: a proposal and analysis, *Opt. Lett.* **24**, 711–713 (1999).

[69] L. Brillouin, *Wave Propagation in Periodic Structures*, Dover, New York, 1953.

[70] A. J. Dekker, *Solid State Physics*, Macmillan, London, 1965.

[71] C. Kittel, *Introduction to Solid State Physics*, Wiley, Hoboken, 2005.

[72] M. I. Rabinovich and D. I. Trubetskov, *Oscillations ans Waves in Linear and Nonlinear Systems*, Dodrecht: Kluwer, 1989.

[73] T. Tamir and A. A. Oliner, Guided complex waves Part 1. Fields at an interface, *Proc. IEE* **110**(2), 310–324 (1963).

[74] A. S. Omar and K. F. Schünemann, Formulation of the singular integral equation technique for planar transmission lines, *IEEE Trans. Microwave Theory Techn.* **MTT-33**(12), 1313–1321 (1985).

[75] M. Mrozowski, *Guided Electromagnetic Waves: Properties and Analysis*, Research Studies Press, Hertfordshire, 1997.

[76] M. C. K. Wiltshire, J. B. Pendry, I. R. Young, J. Larkman, D. J. Gilderdale, and J. V. Hajnal, Microstructured magnetic materials for radio frequency operation in magnetic resonance imaging (MRI), *Science* **291**, 849–851 (2001).

[77] S. Maslovski, S. Tretyakov, and P. Alitalo, Near-field enhancement and imaging in double planar polariton-resonant structures, *J. Appl. Phys.* **96**, 1293–1300 (2004).

[78] P. A. Belov, C. R. Simovski, and P. Ikonen, Canalization of subwavelength images by electromagnetic crystals, *Phys. Rev. B* **71**, 193105–1–4 (2005).

[79] S. Maslovski and S. Tretyakov, Phase conjugation and perfect lensing, *J. Appl. Phys.* **94**, 4241–4243 (2003).

[80] M. J. Freire and R. Marques, A planar magnetoinductive lens for three-dimensional subwavelength imaging, *Appl. Phys. Lett.* **86**, 182505–1–3 (2005).

[81] F. Mesa, M. J. Freire, R. Marques, and J. D. Baena, Three-dimensional superresolution in metamaterial slab lenses: Experiment and theory, *Phys. Rev. B* **72**, 235117–1–6 (2005).

[82] E. Shamonina, V. A. Kalinin, K. H. Ringhofer, and L. Solymar, Imaging, compression and Poynting vector streamlines with negative permittivity materials, *Electron. Lett.* **37**, 1243–1244 (2001).

[83] K. J. Webb, M. Yang, D. W. Ward, and K. A. Nelson, Metrics for negative-refractive-index materials, *Phys. Rev. E* **70**, 035602(R)–1–4 (2004).

[84] V. A. Podolskiy and E. E. Narimanov, Near-sighted superlens, *Opt. Lett.* **30**, 75–77 (2005).

[85] R. R. A. Syms, I. R. Young, and L. Solymar, Low-loss magneto-inductive waveguides, *J. Phys. D: Appl. Phys.* **39**, 3945–3951 (2006).

[86] S. Zhang, W. Fan, K. J. Malloy, S. R. J. Brueck, N. C. Panoiu, and R. M. Osgood, Demonstration of metal-dielectric negative-index metamaterials with improved performance at optical frequencies, *J. Opt. Soc. Am. B* **23**, 434–438 (2006).

[87] N. Bloembergen, *Nonlinear Optics*, World Scientific Publishing, Singapore, 2005.

[88] Y. R. Shen, *Principles of Nonlinear Optics*, Wiley, New York, 1984.

[89] W. H. Louisell, *Coupled Mode and Parametric Electronics*, Wiley, New York, 1960.

[90] L. A. Blackwell and K. I. Kotzebue, *Semiconductor-diode Parametric Amplifiers*, Prentice Hall, 1961.

[91] K.-H. Löcherer and C.-D. Brandt, *Parametric Electronics: An Introduction*, Springer, Berlin, 1982.

[92] A. G. Gurevich and G. A. Melkov, *Magnetization Oscillation and Waves*, CRC, New York, 1961.

[93] A. B. Kozyrev, H. Kim, A. Karbassi, and D. W. van der Weide, Wave propagation in nonlinear left-handed transmission line media, *Appl. Phys. Lett.* **87**, 121109–1–3 (2005).

[94] A. K. Popov and V. M. Shalaev, Negative-index metamaterials: second-harmonic generation, Manley-Rowe relations and parametric amplification, *Appl. Phys. B* **84**, 131–137 (2006).

[95] A. B. Kozyrev, H. Kim, and D. W. van der Weide, Parametric amplification in left-handed transmission line media, *Appl. Phys. Lett.* **88**, 264101–1–3 (2006).

[96] M. W. Klein, C. Enkrich, M. Wegener, and S. Linden, Second-harmonic generation from magnetic metamaterials, *Science* **313**, 502–504 (2006).

[97] O. Sydoruk, A. Radkovskaya, O. Zhuromskyy, E. Shamonina, M. Shamonin, C. J. Stevens, G. Faulkner, D. J. Edwards, and L. Solymar, Tailoring the near-field guiding properties of magnetic metamaterials with two resonant elements per unit cell, *Phys. Rev. B.* **73**, 224406–1–12 (2006).

[98] A. Radkovskaya, O. Sydoruk, M. Shamonin, E. Shamonina, C. J. Stevens, G. Faulkner, D. J. Edwards, and L. Solymar, Experimental study of a bi-periodic magnetoinductive waveguide: comparison with theory, *IET Microw. Antennas Propag.* **1**, 80–83 (2007).

[99] R. P. Agarwal, *Difference Equations and Inequalities: Theory, Methods, and Applications*, Dekker, New York, 2000.

[100] H. M. Gibbs, *Optical Bistability: Controlling Light with Light*, Academic Press, Orlando, 1985.

[101] L. Solymar and D. Walsh, *Electrical Properties of Materials*, Oxford University Press, Oxford, 2004.

[102] O. Sydoruk, V. Kalinin, and E. Shamonina, Parametric amplification of magnetoinductive waves supported by metamaterial arrays, *phys. stat. sol. (b)* **244**, 1176–1180 (2007).

[103] O. Sydoruk, O. Zhuromskyy, E. Shamonina, and L. Solymar, Phonon-like dispersion curves for magnetoinductive waves, *Appl. Phys. Lett.* **87**, 072501–1–3 (2005).

[104] O. Sydoruk, M. Shamonin, A. Radkovskaya, O. Zhuromskyy, E. Shamonina, R. Trautner, C. J. Stevens, D. J. Edwards, G. Faulkner, and L. Solymar, Mechanism of subwavelength imaging with bilayered magnetic metamaterials: theory and experiment, *J. Appl. Phys.* **101**, 073903–1–8 (2007).

[105] O. Sydoruk, E. Shamonina, and L. Solymar, Tailoring of the subwavelength focus, *Microw. Opt. Technol. Lett.* (2007), in print.

[106] R. A. Horn and C. R. Johnson, *Matrix Analysis*, Cambridge University Press, Cambridge, 1985.

[107] Y. Huang and W. F. McColl, Analytical inversion of general tridiagonal matrices, *J. Phys. A: Math. Gen* **30**, 7919–7933 (1997).

[108] T. J. Rivlin, *Chebyshev Polynomials: from Approximation Theory to Algebra and Number Theory*, Wiley, New York, 2nd edition, 1990.

Acknowledgements

To work towards a PhD is like embarking on an exciting voyage. I wish to express here my gratitude to the people who traveled with me all or part of the way, and who alerted me whenever I was in danger of disappearing in a pitfall.

I thank my supervisor, Priv.-Doz. Dr. E. Shamonina, for giving me the chance to work on this project in her group. She created a working environment that supports creativity and self-growth. She has always been able to find a wise balance between supervising and giving a freedom for independent work and thinking. Her excitement about the results obtained and the problems yet to be solved has been for me a source of particular motivation in these years.

I thank my senior colleague, Dr. O. Zhuromskyy, for his support and for many discussions on the subject of metamaterials. He made a large contribution to solving the problems discussed in this thesis.

I am greatly indebted to Professor L. Solymar. I was lucky to have met him at the beginning of my scientific career and to have been able to learn from his experience, vision and enthusiasm.

A cooperation with our partners, Dr. A. Radkovskaya, Prof. M. Shamonin, Prof. R. R. A. Syms, Dr. C. J. Stevens, Prof. D. J. Edwards, Dr. V. Kalinin, Mr. G. Faulkner, and Mr. R. Trautner, has made this project rich not only in theoretical results but also in their experimental verification.

I thank my colleagues Mr. F. Hesmer and Mr. E. Tatartschuk for the friendly atmosphere and for their help.

I thank the Department of Physics for being my home in these years. I thank Prof. K. Betzler, the speaker of Graduiertenkolleg 695. I am grateful to Prof. M. Wöhlecke for organizing the seminars of the Graduiertenkolleg, where I had a chance to present my results. I am grateful to Prof. H.-J. Schmidt, Prof. K. Betzler, Prof. M. Wöhlecke, Prof. M. Rohlfing, Dr. E. Shamonina, and Dr. O. Zhuromskyy whose lectures I attended. I thank the ladies from the administration, especially Mrs. B. Guss and Mrs. S. Guthoff, for their help in all organizational issues. I would like to thank the German Research Council for the financial support.

For a number of interesting and fruitful scientific discussions, I wish to thank Prof. R. Marques, Prof. M. Freire, Dr. M. Lapine, Dr. M. Gorkunov, Prof. I. R. Young, Prof. C. Lienau, and Dr. J. Baena.

I am grateful to Oleksandr Zhuromskyy and his wife, Tatyana Alyokhina-Zhuromskyy, for their hospitality and help during my first days in Germany. I thank my family and friends both in Germany and in Ukraine for their love and support.

Eidesstattliche Erklärung

Hiermit erkläre ich an Eides Statt, die vorliegende Abhandlung selbständig und ohne unerlaubte Hilfe verfaßt, die benutzten Hilfsmittel vollständig angegeben und noch keinen Promotionsversuch unternommen zu haben.

Osnabrück, den 9. Mai 2007

(O. Sydoruk)